Title
Non-Equilibrium Electronic Structure of Cuprate Superconductors

Permalink
https://escholarship.org/uc/item/36d50058

Author
Miller, Tristan

Publication Date
2017

Peer reviewed|Thesis/dissertation

Non-Equilibrium Electronic Structure of Cuprate Superconductors

By

Tristan L. Miller

A dissertation submitted in partial satisfaction of the

requirements for the degree of

Doctor of Philosophy

in

Physics

in the

Graduate Division

of the

University of California, Berkeley

Committee in charge:

Professor Alessandra Lanzara, Chair
Professor Dung-Hai Lee
Professor Zi Q. Qiu
Professor Andrew Minor

Fall 2017

Non-Equilibrium Electronic Structure of Cuprate Superconductors

Abstract

Non-Equilibrium Electronic Structure of Cuprate Superconductors

by

Tristan L. Miller

Doctor of Philosophy in Physics

University of California, Berkeley

Professor Alessandra Lanzara, Chair

Ever since high-temperature cuprate superconductors were discovered in 1986, they have been a source of many mysteries and controversies among scientists. The biggest mystery is the mechanism of high-temperature superconductivity. While it is known that electrons bind together in Cooper pairs, it is not known why. A second mystery is the origin of the pseudogap, a state that exists above the superconducting critical temperature. To address these problems, experimentalists have been looking for new techniques to provide new perspectives.

In this dissertation, we study cuprate superconductors using the recently-developed technique of time- and angle-resolved photoemission spectroscopy (TARPES). This technique uses infrared laser pulses to excite materials out of equilibrium, and to probe their electronic structure. TARPES has matured to the point that we understand the technique, but have not fully explored the scientific possibilities. This work seeks to push the boundaries by finding and characterizing unusual phenomena in the TARPES data, and developing frameworks to understand them. In the process, we address the central mysteries of cuprate superconductors.

In Chapter 1, we outline the theory of conventional superconductors, including many technical details of electron-boson coupling. We then discuss cuprate superconductors, establishing the basic properties of their electronic structure and related controversies. In Chapter 2, we briefly discuss our experimental technique and what it measures. We also review the literature of TARPES studies on cuprates. Chapters 3, 4, and 5 describe three different studies on cuprates, each looking at a different phenomenon. Chapter 3 looks at the chemical potential, and finds a connection to the pseudogap state. Chapter 4 looks at the buildup time of non-equilibrium quasiparticles, and finds a connection to the stimulated recombination of Cooper pairs. Chapter 5 looks at the signatures of electron-boson coupling, and proposes a way to determine if it contributes to Cooper pairing. In Chapter 6, we briefly summarize the main findings and offer some concluding remarks.

For Elliot

Contents

List of Figures

Acknowledgments

Several years ago, my older brother, who was at the very end of his Ph.D., quit. His advisor did not have the funding to pay him, and refused to let him graduate. He later completed his Ph.D. after his department allowed him to submit a thesis without his advisor's approval. Knowing that things can go very wrong in academic research, I have always been grateful for the support I have received in my own Ph.D.

First and foremost, I thank my advisor, Alessandra Lanzara. I do not take it for granted that she was able to maintain consistent funding, and run a welcoming research group. Above and beyond that, she has provided much needed guidance on my research, providing a larger perspective when I was bogged down in details. In what I'm sure was a tough balancing act, she simultaneously provided me the space to pursue my own ideas. She also places a high value on communicating our research to other scientists, and provides a valuable role model by being an excellent communicator herself.

I thank my colleagues Christopher Smallwood and Wentao Zhang, who served as mentors at the beginning of my Ph.D. My appreciation for them has only grown over time as I attempt to mentor younger grad students. Both of them are very knowledgeable and careful experimentalists, and I wish them success in their academic careers. Furthermore, it is not exaggeration to say that all my scientific research was built upon theirs. It is because of their ground work that I was able to focus so much on the data, rather than spending time troubleshooting instruments. Along these lines I also thank the people before me who worked on our scientific instruments, including Jeff Graf, Chris Jozwiak, and John Pepper.

I have also had the pleasure to work with many other excellent colleagues. When I first joined the research group, Alessandra was living abroad, but the older generation, including Chris Jozwiak, David Siegel, and Choonkyu Hwang, created a friendly setting and prevented me from ever getting too lost. Kenny Gotlieb, who joined the group at the same time as me, has always been source of optimism and excitement. Among the younger students, I would like to thank Jonathan Ma, who has provided much perspective on grad school and life, even though he might believe that it was me providing perspective to him. He and the other students, including Greg Affeldt, Drew Latzke, Chiu-Yun Lin, and Ryo Mori, as well as the postdocs Irene Lo Vecchio and Cassi Hunt, have perpetuated the positive climate of the group. The newest students, Nick Dale, Sam Ciocys, Conrad Stansbury, and Prosper Dzanwa have in a brief time done very impressive work. Finally, I enjoyed the company of Alex Nguyen, who began as an undergraduate, but has now gone to grad school.

I have also enjoyed many discussions with other scientists, including Jonathan Denlinger, Dung-Hai Lee, Robert Kaindl, Joe Orenstein, Joel Moore, Lex Kemper, and James LeBlanc. They were all patient enough to answer my many questions, and more besides. I also thank Arun Bansil, Matti Lindroos, and their respective research groups for helping on one of my early projects. My work would not be possible without Hiroshi Eisaki, who grew most of the crystal samples that I studied.

I am grateful for my friends and colleagues outside of physics, of which there are too many to name. Zack Subin deserves particular credit for being a good friend, and a source

of many other friends. Mary Ginoza has worked with me on several activist projects, and I have deep respect for her.

My family has been very supportive throughout my Ph.D, and my life. My mother reintroduced me to origami, and has often demanded that I take longer vacations. My brother has been someone I could commiserate with.

I met my partner, Elliot, at the beginning of grad school, and we have been together ever since. He has always been there for me, and I look forward to what happens next.

Curriculum Vitæ
Tristan L. Miller

Education

2010–2017   University of California, Berkeley, CA, USA
        Ph.D., Physics

2006–2010   University of California, Los Angeles, CA, USA
        B.S., Physics

Publications

1. <u>T. L. Miller</u>, W. T. Zhang, H. Eisaki, and A. Lanzara. Interplay of superconductivity and bosonic coupling in the peak-dip-hump structure of $Bi_2Sr_2CaCu_2O_{8+\delta}$. In preparation (2017).

2. <u>T. L. Miller</u>, W. T. Zhang, H. Eisaki, and A. Lanzara. Particle-Hole Asymmetry in the Cuprate Pseudogap Measured with Time-Resolved Spectroscopy. Phys. Rev. Lett. **118**, 097001 (2017).

3. W. T. Zhang, <u>T. L. Miller</u>, C. L. Smallwood, Y. Yoshida, H. Eisaki, R. A. Kaindl, D.-H. Lee, and A. Lanzara. Stimulated emission of Cooper pairs in a high-temperature cuprate superconductor. Sci. Rep. **6**, 29100 (2016).

4. C. L. Smallwood, <u>T. L. Miller</u>, W. T. Zhang, R. A. Kaindl, and A. Lanzara. Nonequilibrium electron dynamics in a solid with a changing nodal excitation gap. Phys. Rev. B **93**, 235107 (2016).

5. <u>T. L. Miller</u>, C. L. Smallwood, W. T. Zhang, H. Eisaki, J. Orenstein, and A. Lanzara. Photoinduced changes of the chemical potential in superconducting $Bi_2Sr_2CaCu_2O_{8+\delta}$. Phys. Rev. B **92**, 144506 (2015).

6. C. L. Smallwood, W. T. Zhang, <u>T. L. Miller</u>, G. Affeldt, K. Kurashima, C. Jozwiak, T. Noji, Y. Koike, H. Eisaki, D.-H. Lee, R. A. Kaindl, and A. Lanzara. Influence of optically quenched superconductivity on quasiparticle relaxation rates in $Bi_2Sr_2CaCu_2O_{8+\delta}$. Phys. Rev. B **92**, 161102(R) (2015).

7. <u>T. L. Miller</u>, M. Ärrälä, C. L. Smallwood, W. T. Zhang, H. Hafiz, B. Barbiellini, K. Kurashima, T. Adachi, Y. Koike, H. Eisaki, M. Lindroos, A. Bansil, D.-H. Lee, and A. Lanzara. Resolving unoccupied electronic states with laser ARPES in bismuth-based cuprate superconductors. Phys. Rev. B **91**, 085109 (2015).

8. W. T. Zhang, C. Hwang, C. L. Smallwood, <u>T. L. Miller</u>, G. Affeldt, K. Kurashima, C. Jozwiak, H. Eisaki, T. Adachi, Y. Koike, D.-H. Lee, and A. Lanzara. Ultrafast quenching of electron-boson interaction and superconducting gap in a cuprate superconductor. Nat. Commun. **5**, 4959 (2014).

9. C. L. Smallwood, W. Zhang, <u>T. L. Miller</u>, C. Jozwiak, H. Eisaki, D.-H. Lee, and A. Lanzara. Time- and momentum-resolved gap dynamics in $Bi_2Sr_2CaCu_2O_{8+\delta}$. Phys. Rev. B **89**, 115126 (2014).

10. W. Zhang, C. L. Smallwood, C. Jozwiak, <u>T. L. Miller</u>, Y. Yoshida, H. Eisaki, D.-H. Lee, and A. Lanzara. Signatures of superconductivity and pseudogap formation in nonequilibrium nodal quasiparticles revealed by ultrafast angle-resolved photoemission. Phys. Rev. B **88**, 245132 (2013)

Invited Talks and Seminars

1. "Ultrafast Quenching of Electron-Boson Interaction and Superconducting Gap in a Cuprate Superconductor." Probing and Understanding Exotic Superconductors and Superfluids, Oct. 2014

Contributed Talks

1. "Measuring Particle-Hole Asymmetry in Bi2212 with Time-Resolved Spectroscopy." APS March Meeting, Mar. 2017

2. "Photoinduced Chemical Potential Shifts in Bi2212." APS March Meeting, Mar. 2016

3. "Shift in Chemical Potential of Superconducting Bi2212 Measured by Ultrafast Photoemission Spectroscopy." APS March Meeting, Mar. 2015

4. "Probing Many-Body Interactions in High-T_c Superconductor Bi2212 using Time- and Angle-Resolved Photoemission." APS March Meeting, Mar. 2013

Chapter 1

Introduction

Superconductivity is defined by two characteristics: zero electrical resistance, and perfect diamagnetism. It was first discovered by Kamerlingh Onnes in 1911, when he cooled mercury below 4 K. In general, superconductivity appears in materials when they are cooled below the critical temperature T_c, which depends on the material. A satisfactory mechanism for superconductivity was not found until 1957, when John Bardeen, Leon Cooper, and John Robert Schrieffer established the BCS theory (named for their initials). In this theory, the zero resistance electrical current is carried by pairs of electrons, called Cooper pairs. Normally, Cooper pairs cannot form because electrons repel each other by the Coulomb interaction. However, in a conventional superconductor, phonons, the quanta of lattice vibrations, create an attractive interaction between electrons, allowing Cooper pairs to form.

In 1986, Johannes Georg Bednorz and Karl Alex Müller discovered the cuprates, a new class of superconductors. Cuprates have been a subject of much interest for the past three decades for two major reasons. The first reason is that cuprates have the highest known critical temperatures among all superconductors, now reaching up to $T_c = 135$ K. This is compared to 33 K, the highest T_c for conventional superconductors. Currently, superconducting technology is used to generate high magnetic fields for magnetic resonance imaging and in research applications, and many applications in power grids are being developed. If superconductors were found with even higher critical temperatures, then superconducting technology would be possible without cryogenics.

The second reason is that the mechanism for cuprate superconductivity has not yet been established. Cuprates are a class of unconventional superconductors, meaning that BCS theory does not suffice to explain them. Superconductivity in cuprates is still the result of Cooper pairing, but the pairing may or may not be the result of interactions with phonons. One significant fact is that the binding energy of the Cooper pairs significantly depends on the electron momentum. Therefore, an important tool to investigate cuprates is angle-resolved photoemission spectroscopy (ARPES), which resolves the momentum-dependent electronic structure.

In this chapter, we will discuss the theoretical and experimental background of superconductors, with an eye towards ARPES experiments on cuprates. In Section 1.1, we discuss the theory of conventional superconductivity, especially as it affects the electronic structure and electron Green's functions.[1,2,3,4] In Section 1.2, we will discuss the basic electronic properties of cuprate superconductors.

1.1 Conventional superconductors

1.1.1 The electron-phonon interaction

Conventional superconductivity requires that electrons attract and form bound pairs. At first, this seems impossible because of the Coulomb repulsion between negative charges. However, each electron charge is screened by a cloud of positive charge around them. There are two contributions to screening. The first part arises from the Coulomb repulsion of other electrons, along with the Pauli exclusion principle. This is known as the exchange correlation hole. The second part arises from the electron-phonon interaction, and can be understood as the displacement of ions in the crystal lattice towards the electron. When the electron is considered in combination with the cloud of excitations surrounding it, it is called a quasiparticle. In certain situations, the positive charge due to screening is greater than the negative charge of the electrons themselves, and thus quasiparticles are attracted to each other, and form Cooper pairs.

The screening can be understood as a modification of the dielectric function, which is a function of both frequency and wavevector. We will not derive the full dielectric function because it is quite complicated (see Ref. 5), and because the mechanism for superconductivity does not depend sensitively on the details. However, we will describe a classical system to intuitively explain how an attractive force is possible at nonzero frequencies. Suppose that there is an oscillating charge in the crystal. This charge creates a periodic driving force on the crystal lattice, which behaves like a harmonic oscillator. When the driving frequency is near the resonant frequency of the crystal lattice, the amplitude of oscillations becomes very large. If the driving frequency is below the resonant frequency, then the crystal lattice will oscillate in phase, and if the driving frequency is above the resonant frequency, then it will oscillate out of phase. Therefore, at some frequency just below the resonant frequency, the crystal lattice will be strongly driven, and this will overcompensate for the original oscillating charge.

The Hamiltonian of the quantum system is of the form

$$\mathscr{H} = \sum_{k,\sigma} \epsilon_k c^\dagger_{k,\sigma} c_{k,\sigma} + \sum_{k,k',q,\sigma,\sigma'} V_{k,k'} c^\dagger_{k',\sigma} c^\dagger_{k+q,\sigma'} c_{k'+q,\sigma'} c_{k,\sigma}. \tag{1.1}$$

Here, $c^\dagger$ and c are the quasiparticle creation and annihilation operators, which obey the usual Fermionic commutation relations. ϵ_k are the energies of the non-interacting quasiparticles,

and $V_{k,k'}$ are the scattering amplitudes. A positive $V_{k,k'}$ indicates a repulsive interaction, while a negative $V_{k,k'}$ indicates attractive interaction. As in the classical system, there is an attractive interaction at frequencies just below the phonon frequency, but unlike the classical system, it may also be attractive at zero frequency. Frequencies are associated with energy differences, so that means $V_{k,k'}$ is negative when the states at k and k' have an energy difference less than the phonon energy. This is a sufficient condition to allow superconductivity at low temperatures, regardless of any other particulars of the shape of $V_{k,k'}$.

1.1.2 The superconducting ground state

To construct the superconducting ground state, we first consider a single pair of quasiparticles, in a spin singlet state and with zero total momentum. The single pair wavefunction is

$$|\Psi_p\rangle = c_{k,\uparrow}^\dagger c_{-k,\downarrow}^\dagger |\Psi_F\rangle, \tag{1.2}$$

where $|\Psi_F\rangle$ is the Fermi sea state (i.e. all quasiparticle states below the Fermi energy are occupied). To construct the ground state, we superimpose many of these quasiparticle pairs, and assume that the probability of each quasiparticle pair is independent of all the other pairs. This results in the ansatz

$$|\Psi_0\rangle = \prod_k (u_k + v_k c_{k,\uparrow}^\dagger c_{-k,\downarrow}^\dagger)|0\rangle, \tag{1.3}$$

where $|0\rangle$ is the state without any quasiparticles. u_k and v_k are probability amplitudes with the normalization condition $|u_k|^2 + |v_k|^2 = 1$ for all k. There is also an alternate parametrization by θ_k and ϕ_k, with

$$\begin{aligned} u_k &= \sin\theta_k \\ v_k &= e^{i\phi_k}\cos\theta_k \end{aligned}. \tag{1.4}$$

Given the ansatz in Eq. (1.3), we can solve for u_k and v_k by minimizing the free energy. To do this, we first reduce the Hamiltonian in Eq. (1.1) by selecting only the terms that scatter between zero momentum spin singlet quasiparticle pairs. Specifically, we take only terms where $q = -k' - k$ and where σ and σ' are in opposite directions. The reduced Hamiltonian, known as the pairing Hamiltonian, is

$$\mathscr{H}_p = \sum_{k,\sigma} \epsilon_k c_{k,\sigma}^\dagger c_{k,\sigma} + \sum_{k,k'} V_{k,k'} c_{k',\uparrow}^\dagger c_{-k',\downarrow}^\dagger c_{-k,\downarrow} c_{k,\uparrow}. \tag{1.5}$$

The free energy is $\mathscr{H}_p - \mu N$. It makes things simpler if we measure all energies relative to the chemical potential μ, replacing ϵ_k with $\varepsilon_k = \epsilon_k - \mu$.

By minimizing the free energy, we find the following solution:

$$
\begin{array}{rcl}
\tan 2\theta_k &=& -\frac{|\Delta_k|}{\varepsilon_k} \\[4pt]
\phi_k &=& \phi \\[4pt]
|u_k|^2 &=& \frac{1}{2}\left(1 + \frac{\varepsilon}{E_k}\right) \\[4pt]
|v_k|^2 &=& \frac{1}{2}\left(1 - \frac{\varepsilon}{E_k}\right)
\end{array}
\tag{1.6}
$$

Here we use the quantities Δ_k and E_k which are defined by

$$
\begin{array}{rcl}
\Delta_k &=& -\sum_{k'} V_{k,k'} u_{k'} v_{k'} \\[4pt]
E_k &=& \sqrt{\varepsilon_k^2 + |\Delta_k|^2}
\end{array}
\tag{1.7}
$$

Equations (1.6) and (1.7) are circular, but can be solved self-consistently. Δ_k is called the gap parameter, and it is approximately independent of k in most conventional superconductors. E_k will turn out to be the energies of the Bogoliubov excitations, discussed in the next section. $|v_k|^2$ is the probability that the pair of quasiparticle states at momentum k are occupied. $|v_k|^2$ looks a little bit like the Fermi-Dirac distribution function, in that it approaches 1 far below the Fermi energy, and approaches 0 far above the Fermi energy. However, the Fermi-Dirac distribution function becomes a step function at zero temperature, while $|v_k|^2$ always changes smoothly from 0 to 1 over an energy range of about Δ.

We note that there are many independent solutions with different values of ϕ, and that any particular solution will have an uncertain number of particles. The true ground state of the system will be a linear combination of states with different ϕ, and the precise linear combination determines the probability amplitudes on the number of particles. For our purposes it suffices to take just a single value of ϕ.

1.1.3 Bogoliubov quasiparticles

In a metal, the elementary excitations above the Fermi energy are electrons, while those below the Fermi energy are holes. The creation operator for such an excitation might look like

$$
\gamma_{k,\sigma}^\dagger = \Theta(\varepsilon_k)c_{k,\sigma}^\dagger + (1 - \Theta(\varepsilon_k))c_{-k,-\sigma},
\tag{1.8}
$$

where Θ is the step function. However, as previously discussed, in the superconducting ground state, the occupation function $|v_k|^2$ varies smoothly even at zero temperature, instead of being a step function. With that in mind, we can define elementary excitations similar to a metal, only replacing the sharp step function Θ with the smoother functions u_k and v_k:

$$
\begin{array}{rcl}
\gamma_{k,\uparrow}^\dagger &=& u_k^* c_{k,\uparrow}^\dagger - v_k^* c_{-k,\downarrow} \\[4pt]
\gamma_{-k,\downarrow}^\dagger &=& u_k^* c_{-k,\downarrow}^\dagger + v_k^* c_{k,\uparrow}
\end{array}
\tag{1.9}
$$

Equation (1.9) defines a canonical transformation from the normal quasiparticles (c and $c^\dagger$ operators) into the Bogoliubov quasiparticles (γ and $\gamma^\dagger$ operators). Similar to the excitations in a metal, Bogoliubov quasiparticles are holelike when far below the Fermi energy,

4

and electronlike when far above the Fermi energy. But near the Fermi energy, the Bogoliubov quasiparticles are mixtures of holelike and electronlike quasiparticles. The Bogoliubov quasiparticle can be interpreted as a single electron escaping from the Cooper pairs. If there is a Bogoliubov quasiparticle at momentum k, then this is equivalent to a state where the normal quasiparticle state at k is completely occupied, while the normal quasiparticle state at $-k$ is completely unoccupied.

We can verify that Bogoliubov quasiparticles are are elementary excitations by showing that the Hamiltonian is diagonal in the γ operators. But first, we must further simplify the Hamiltonian using mean field theory. We take b_k to be the mean value of $c_{-k,\downarrow}c_{k,\uparrow}$. We now make the expansion

$$c_{-k,\downarrow}c_{k,\uparrow} = b_k + (c_{-k,\downarrow}c_{k,\uparrow} - b_k). \tag{1.10}$$

The second term in Eq. (1.10) is a small perturbation, and we can neglect any terms in the Hamiltonian which are second order in that perturbation. We also subtract the energy μN, because it is just a constant offset to the energy. The resultant Hamiltonian, called the model Hamiltonian, is

$$\mathscr{H}_M = \sum_{k,\sigma} \varepsilon_k c_{k,\sigma}^\dagger c_{k,\sigma} + \sum_{k,k'} V_{k,k'}(b_{k'}^* c_{-k,\downarrow}c_{k,\uparrow} + c_{k',\uparrow}^\dagger c_{-k',\downarrow}^\dagger b_k - b_{k'}^* b_k). \tag{1.11}$$

In the ground state, b_k is simply equal to $u_k v_k$. At nonzero temperatures, b_k may deviate from that value. By using the temperature dependence of b_k, we can also extend the definition of Δ_k from Eq. (1.7) to nonzero temperatures:

$$\Delta_k = -\sum_{k'} V_{k,k'} b_{k'}. \tag{1.12}$$

This also leads to an extension of the definition of E_k, and the solutions to u_k and v_k in Eq. (1.6). These extended solutions are correct even at nonzero temperature. Using these solutions, the model Hamiltonian becomes

$$\mathscr{H}_M = \sum_k (\varepsilon_k - E_k + \Delta_k^* b_k) + \sum_{k,\sigma} E_k \gamma_{k,\sigma}^\dagger \gamma_{k,\sigma}. \tag{1.13}$$

The model Hamiltonian is diagonal in the γ operators, and this means that Bogoliubov quasiparticles are elementary excitations. The energy of these excitations is E_k. The lowest energy Bogoliubov quasiparticles have energy $|\Delta_k|$, and appear at the normal state Fermi momentum. The binding energy of a Cooper pair is $2|\Delta_k|$, since that is the minimum energy required to break a single Cooper pair into two Bogoliubov quasiparticles.

Although the $\gamma_{k,\sigma}$ operators are not the same $c_{k,\sigma}$ operators we started with, they behave exactly like Fermionic quasiparticles with energy E_k. Therefore Bogoliubov quasiparticles are elementary excitations of a superconductor. The lowest energy Bogoliubov quasiparticles have energy $|\Delta_k|$, and appear at the normal state Fermi momentum. They consist of mixtures of electronlike and holelike quasiparticles. A Cooper pair may form from the annihilation of two Bogoliubov quasiparticles, so we say that the binding energy of a single Cooper pair is $2|\Delta_k|$.

In ARPES, Bogoliubov quasiparticles have a distinctive appearance. There will appear two branches corresponding to the creation and annihilation of Bogoliubov quasiparticles. If a Bogoliubov quasiparticle is created, then the photoemitted electron has energy equal to $\mu - E_k$. If a Bogoliubov quasiparticle is annihilated, then the photoemitted electron has energy equal to $\mu + E_k$. The spectral weight of the two branches are not equal, because photoemission may only create a holelike quasiparticles, and annihilate electronlike quasiparticles. The weight of the lower branch is $|v_k|^2$, which is the probability that a particular Bogoliubov quasiparticle is holelike, and the weight of the upper branch is $|u_k|^2$, the probability that the Bogoliubov quasiparticle is electronlike.

A further modification to the weight arises from the fact that a Bogoliubov quasiparticle state may already be occupied or unoccupied. At zero temperature, all Bogoliubov quasiparticle states are unoccupied, and thus only the lower branch is visible. At nonzero temperature, the quasiparticle states are occupied, with probability equal to the Fermi-Dirac function $f(E_k, T)$. The weight of the upper branch is multiplied by $f(E_k, T)$, while the lower branch is multiplied by $1 - f(E_k, T)$.

1.1.4 Zero resistivity and the Meissner effect

We take a moment to briefly discuss how BCS theory leads to the two major macroscopic characteristics of superconductivity: zero electrical resistance and the Meissner effect.

First, we note that Cooper pairs may carry electric current. The ground state defined in Eq. (1.3) has zero current, but there exist metastable states with nonzero current. Specifically, we may have Cooper pairs consisting of quasiparticles at $(k + q/2)$ and $(-k + q/2)$, with total momentum q. An equivalent way to think about these states is by having ϕ vary slowly in space, with the current proportional to the gradient of ϕ. In an ordinary metal, current is carried by individual quasiparticles, and resistance is caused by scattering, but in a superconductor, current is carried by the macroscopic state of the system rather than the excitations from that ground state. Scattering may create or destroy Bogoliubov quasiparticles, but current still flows without resistance as long as there is no change in the macroscopic state. In the situations where superconductors have a nonzero resistance, it arises from macroscopic current vortices traversing the superconductor.

If one calculates the current in the presence of an electromagnetic field, one finds that the current density $\mathbf{J}$ is proportional to the negative of the electromagnetic vector potential $\mathbf{A}$, in the Coulomb gauge. Using $\mathbf{B} = \nabla \times \mathbf{A}$ and $\mathbf{J} \propto \nabla \times \mathbf{B}$, we find that any external magnetic field quickly decays at the surface of the superconductor. The physical mechanism is that the external magnetic field is cancelled by currents near the surface. This cancellation of external magnetic fields is called perfect diamagnetism, also known as the Meissner effect.

1.1.5 Green's function formalism

In the true Hamiltonian of a superconductor, Bogoliubov quasiparticles are not eigenstates of energy, and it is necessary to include interaction terms. In this case, a more appropriate approach to the problem is using the Green's function formalism. The Green's function is

$$G(r, r', t, t') = -i\langle\Omega|Tc(r, t)c^\dagger(r', t')|\Omega\rangle, \tag{1.14}$$

where Ω is the system's quantum state and T is the time-ordering symbol. The Green's function is essentially the response of the system to the creation or annihilation of an electron at a single point in time and space. This particular Green's function is called the Feynman propagator, because it restricts the cause to precede the effect, although the cause may either be the creation of an electron at time t', or the annihilation of an electron at time t. Other Green's functions can be defined, such as

$$G^-(r, r', t, t') = i\langle\Omega|c^\dagger(r', t')c(r, t)|\Omega\rangle\Theta(t' - t) \tag{1.15}$$

and

$$G^+(r, r', t, t') = -i\langle\Omega|c(r, t)c^\dagger(r', t')|\Omega\rangle\Theta(t - t'), \tag{1.16}$$

which are the electron removal and electron addition Green's functions, respectively.

The Green's function conveys lots of useful information; for instance, if the created electron appears in an eigenstate with energy $\hbar\omega$, then the response of G would be to oscillate with respect to t with a frequency of ω. In fact, it is more useful to consider the function $G(k, \omega)$, the Fourier transform of $G(r, r', t, t')$ with respect to $r - r'$ and $t - t'$. As will be discussed in Section 2.1, the ARPES intensity as a function of momentum and energy is proportional to the imaginary part of $G^-(k, \omega)$.

To calculate the Green's function, we begin with G_0, the Green's function of the non-interacting Hamiltonian. We then account for the interaction term in the Hamiltonian by summing an infinite series of Feynman diagrams. This results in

$$G(k, \omega) = \frac{1}{G_0^{-1}(k, \omega) - \Sigma(k, \omega)} = \frac{1}{\omega - \epsilon_k - \Sigma(k, \omega)}, \tag{1.17}$$

which is known as the Dyson equation. The function $\Sigma(k, \omega)$ is called the electron self-energy, and consists of an infinite sum of Feynman diagrams. The real part of Σ modifies the energy of quasiparticles, while the imaginary part of Σ modifies the lifetime of quasiparticles

There are three main contributions to the self-energy: electron-impurity interactions, electron-electron interactions, and electron-boson interactions. Electron-impurity interactions add a constant term to the imaginary part of Σ. Electron-electron interactions in a normal metal are described by Fermi Liquid theory, which has an imaginary self-energy proportional to ω^2. Finally, we have the electron-boson interactions, which are discussed in the next section.

1.1.6 Eliashberg theory

Conventional superconductivity is caused by electron-phonon interactions. More generally, superconductivity may be caused by any electron-boson interaction, and the boson need not be a phonon. Regardless of the identity of the boson, it is clear that the electron-boson interaction cannot be treated in a simple perturbative way, since superconductivity is not merely a perturbation of the normal state. If we were to calculate Σ with the electron-boson interaction, we would find that a subset of the Feynman diagrams have a divergent sum. We must remove this sum by taking it out of the self-energy, and putting it into G_0. We introduce the Nambu-Gor'kov formalism as a way of doing just that.

We define a two-component field operator

$$\Psi_k = \begin{pmatrix} c_{k,\uparrow} \\ c^\dagger_{-k,\downarrow} \end{pmatrix} \tag{1.18}$$

and let the Green's function be

$$G(k,t) = -\langle UT\Psi_k(t)\Psi^\dagger_k(0)\rangle. \tag{1.19}$$

where U is the operator that restores the original number of electrons. Now, G is a 2x2 matrix, and the electron self-energy Σ is also a 2x2 matrix. They are related by a modified Dyson equation

$$G^{-1}(k,\omega) = \omega\mathbf{1} - \epsilon_k\tau_3 - \Sigma(k,\omega), \tag{1.20}$$

where τ_i are the Pauli matrices. Σ has the canonical form

$$\Sigma(k,\omega) = (1 - Z(k,\omega))\omega\mathbf{1} + \phi(k,\omega)\tau_1 + \bar{\phi}(k,\omega)\tau_2 + \chi(k,\omega)\tau_3, \tag{1.21}$$

which defines the complex-valued functions Z, ϕ, $\bar{\phi}$ and χ. Z is a renormalization factor that determines the single-electron self-energy. ϕ is the self-energy of the Cooper pairs, with the real part determining the pair binding energy, and the imaginary part determining the pair lifetime. $\bar{\phi}$ can be set to zero by choice of phase convention. χ has an effect on the quasiparticle energies but is usually very small and will be neglected in this discussion.

To understand electron-boson coupling, we first discuss its impact in qualitative terms. First, suppose we have a metal at zero temperature with an optical phonon mode with energy Ω. Holelike quasiparticles can only decay by emitting a phonon if they have energy of at least Ω. As a result, there is a sharp step in the quasiparticle lifetime at energy Ω. In the self-energy, we would see this as a sharp step in the imaginary part of Z. By applying the Kramers–Kronig relation, we can determine that the real part of Z has a peak near Ω, and that quasiparticles with energy below Ω have a smaller velocity. We can think of Z as arising from the virtual scattering and reabsorption of phonons, and from the blocking of similar virtual processes of other quasiparticles.

At nonzero temperatures, nolelike quasiparticles below Ω can emit bosons by recombining with thermally excited quasiparticles. However, this process is slower because of the low occupation density of thermal quasiparticles. Thus, there will still be a sharp step in the quasiparticle lifetime at energy Ω, although it will not be quite as sharp.

In the presence of superconductivity, the picture is slightly different because the minimum energy of a quasiparticle is not zero, but Δ. Only quasiparticles above $\Delta + \Omega$ can decay by boson emission without recombining with thermally excited quasiparticles. This causes the features in Z to appear at energy $\Delta + \Omega$ instead of Ω. At this same energy, there will also appear certain features in the function ϕ.

For a quantitative estimate of the electron-boson self-energy, we can use the Eliashberg equation, which is based on the one-loop approximation of the Nambu-Gor'kov self-energy. A simplified version of these equations is as follows:[2]

$$
\begin{aligned}
\Sigma(k, \omega) = \int_{-\infty}^{\infty} \mathrm{d}\omega' \int_{0}^{\infty} \mathrm{d}\Omega \; \alpha^2 F(\Omega) \; \mathrm{Re}&\left(\frac{\omega' \tilde{Z}(\omega')\mathbf{1} + \tilde{\phi}(\omega')\tau_1}{\sqrt{\omega'^2 \tilde{Z}^2(\omega') - \tilde{\phi}^2(\omega')}} \right) \\
\times &\left(\frac{f(-\omega') + n(\Omega)}{\omega' + \Omega - \omega - i0^+} + \frac{f(\omega') + n(\Omega)}{\omega' - \Omega - \omega - i0^+} \right)
\end{aligned}
\tag{1.22}
$$

The $\tilde{Z}$ and $\tilde{\phi}$ refer to the electron-boson self-energy after being renormalized by the electron-electron self-energy, and $\alpha^2 F(\Omega)$ is known as the Eliashberg coupling function.

This Eliashberg equation essentially encodes the intuition that we had previously discussed. The integrand describes interactions where quasiparticles at energy ω scatter to energy ω' by way of absorption or emission of a boson with energy Ω. If we look at the final term of the integrand, we see that it has a nonzero imaginary part whenever $\omega = \omega' \pm \Omega$, which is equivalent to the condition of conservation of energy. The integrand is also in a form such that it automatically obeys the Kramers–Kronig relation. The rate of boson interaction also depends on the electron-boson coupling strength and bosonic density of states, all of which is encoded in the Eliashberg coupling function $\alpha^2 F(\Omega)$. Finally, the rate of interaction depends on the number of available quasiparticle states at ω', and this is encoded in the middle term of the integrand.

The Eliashberg equation as it is given in Eq. (1.22) is somewhat simplified. First, number of available states at ω' is calculated only from the self-energy, and assumes that the bare electronic structure has a constant density of states. This assumption allows us to neglect χ. Second, $\alpha^2 F(\Omega)$ relies momentum averaging. Momentum averaging may be invalid if the bosons prefer to scatter quasiparticles between certain momenta. Finally, the Eliashberg equation is based on a one-loop approximation. In situations with polarons, other calculations are needed, especially to describe the appearance of satellites.[6]

1.1.7   Simulations of the kink

Although Eliashberg theory is quite complicated, it is important because of its impact on the low-energy electronic structure. The sharp features in Σ generate a "kink" structure in the electronic dispersion, which is directly observable with ARPES. Here we explain what the kink looks like, with the assistance of some basic simulations. These simulations show the spectral density function $A(k, \omega)$, which is proportional to the imaginary part of $G_{11}(k, \omega)$
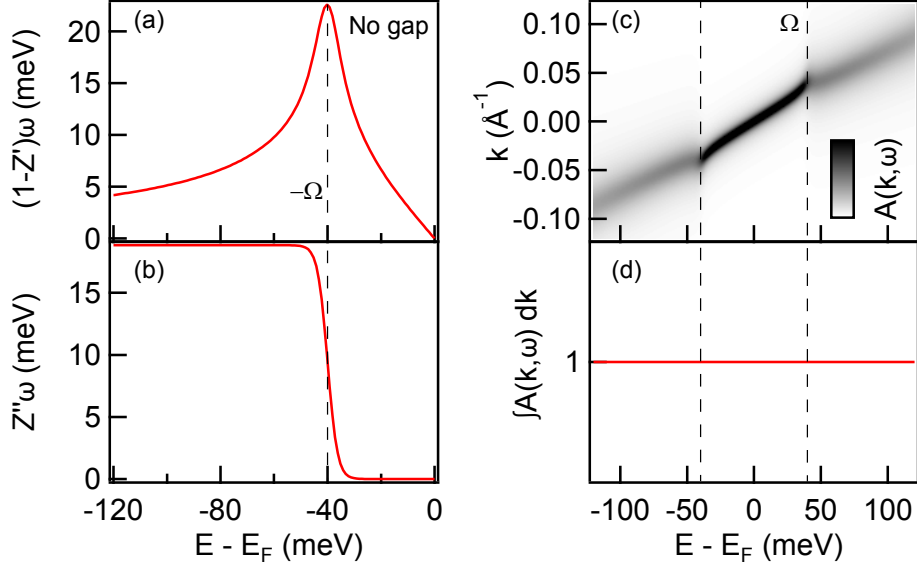
Figure 1.1. A simulation of the electron-boson kink in a metal.

(the upper left entry of the Green's function). As will be discussed in Section 2.1, the ARPES intensity is proportional to the spectral density function, although not identical.

We begin with a simulation in a metal without any superconductivity, shown in Figure 1.1. Here, ϕ is set to zero, and G is a diagonal matrix. We use an Einstein phonon with energy $\Omega = 40$ meV, which implies that $\alpha^2 F(\Omega)$ is sharply peaked at Ω. The algorithm is iterative: we start with an initial guess of the self-energy, and at each step we feed the results back into Eq. (1.22). However, the results converge immediately within one or two iterations. Rather than using the full Equation (1.22), it is easier to calculate only the imaginary part of $Z(\omega)$, and subsequently use the Kramers–Kronig relation to estimate the real part. We use Z' to denote the real part and Z'' to denote the imaginary part. Z'' is an odd function of ω (i.e. $Z''(\omega) = -Z''(-\omega)$) while Z' is an even function.

In Figure 1.1(c) we show $A(k, \omega)$, which is calculated from

$$A(k,\omega) \propto \frac{Z''(\omega)\omega}{(Z'(\omega)\omega - \epsilon(k))^2 + (Z''(\omega)\omega)^2}, \qquad (1.23)$$

which is the imaginary part of the Dyson equation. $\epsilon(k)$ is taken to be a linear function of k. Also, for purposes of calculating $A(k, \omega)$, we include a small contribution from Fermi Liquid theory and electron-impurity scattering into $Z(k, \omega)$ to make the spectra more realistic.

Equation (1.23) predicts that when we hold ω constant, $A(k, \omega)$ is a Lorentzian curve. This curve is called a momentum distribution curve, or MDC. $(1 - Z'(\omega))\omega$ modifies the position of the MDC peak, while $Z''(\omega)\omega$ modifies the width of the MDC peak.[7] The width of the MDC peak is directly related to the inverse lifetime of the quasiparticles. In Figure 1.1(c), the MDC peaks are very broad outside the range $[-\Omega, \Omega]$. This agrees with our intuition that quasiparticles outside this range have a shorter lifetime because they may
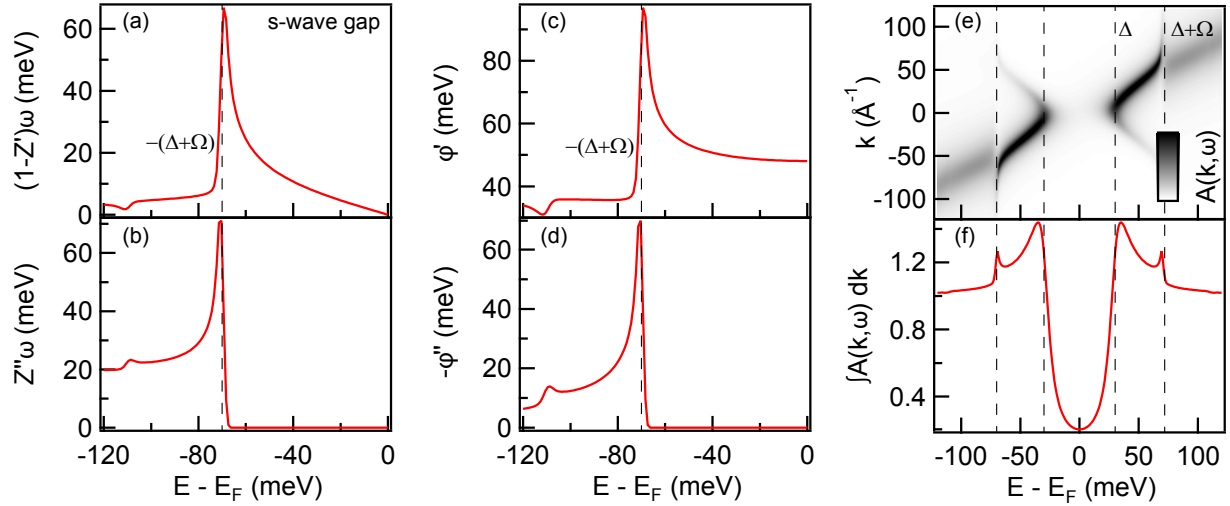
10

Figure 1.2. A simulation of the electron-boson kink in a superconductor with a constant gap.

decay by boson emission. Also note that the positions of the MDC peaks, instead of following a straight line, bends at $\pm\Omega$. This bending arises from virtual interactions with bosons.

The next simulation, shown in Fig. 1.2, introduces the superconducting gap. Here, ϕ is no longer zero, and must be calculated from the off-diagonal component of Eq. (1.22). Similar to the first simulation, we use Eq. (1.22) to calculate ϕ'' (the imaginary part of ϕ), and use the Kramers–Kronig relation to estimate the real part ϕ'. ϕ'' is an odd function of ω, while ϕ' is an even function. The Kramers–Kronig relation is arbitrary up to a constant, so we add a constant to ϕ', chosen such that the gap appears at $\Delta = 30$ meV. The physical meaning of this offset is the part of the superconducting gap that arises from some other source besides the electron-boson coupling under consideration.

In the presence of a superconducting gap, $A(k, \omega)$ has a more complicated form, and near the Fermi energy it is no longer valid to model the MDCs with Lorentzian curves. The major features in Figure 1.2(e) are the lower and upper branches of the Bogoliubov quasiparticles, and the gap between them. As discussed in Section 1.1.3, the weight of the lower branch is $|v_k|^2$, while the weight of the upper branch is $|u_k|^2$. Fig. 1.2(e) also shows a kink structure, just as there was in the absence of a gap, except that now the kinks appear at energies $\pm(\Delta + \Omega)$.

The form of $A(k, \omega)$ is greatly simplified when it is integrated over momentum:

$$\int_{-\infty}^{\infty} A(k, \omega)\mathrm{d}k \propto \mathrm{Re}\frac{Z(\omega)\omega}{\sqrt{(Z(\omega)\omega)^2 - \phi(\omega)^2}}. \tag{1.24}$$

The significance of this integration is that it is proportional to the density of states. As shown in Fig. 1.2(f), there is a depletion of the density of states within the gap, and a pileup of states at the gap edge. We also note a small feature in the density of states near the kink energy at $\pm(\Delta + \Omega)$. This feature only appears when there is a superconducting gap (see

11

the absence of any feature in Fig. 1.1(d)). In Chapter 5 we argue that we have observed this feature experimentally.

So far, our simulations have been assuming a complete lack of momentum dependence. In the case of cuprate superconductors, which will be discussed in Section 1.2, the superconducting gap has a significant momentum dependence. To model this momentum dependence, we can take $\phi(k, \omega) = \phi(\omega)\cos(2\theta)$, where θ is a parametrization of the momentum along the Fermi surface. This affects the density of states, as well as the electron-boson coupling constant.

The electron-boson coupling constant is referred to as λ, and it is equal to

$$\lambda = 2 \int_0^\infty \frac{\alpha^2 F(\omega)}{\omega} \mathrm{d}\omega. \tag{1.25}$$

These simulations use a modest value of $\lambda = 0.3$. However in the case of a momentum dependent superconducting gap, we must also consider the momentum dependence of the electron-boson coupling. Following Ref. Ref. 8, we decompose λ into an isotropic component λ_Z used to calculate Z and an anisotropic component λ_ϕ used to calculate ϕ. This obeys our intuition that only anisotropic electron-boson coupling can contribute to an anisotropic superconducting gap. But for now, we keep $\lambda_Z = \lambda_\phi$, and explore this parameter space more deeply in Chapter 5.

To account for the momentum dependence of the density of states, we replace the density of states in Eq. 1.22 with a weighted sum of the density of states along the whole Fermi surface. The weighting is not necessarily uniform, because bosons may preferentially scatter quasiparticles to certain momenta. In the case of extreme anisotropy, quasiparticles at θ may scatter exclusively towards $\pm\theta + n\pi/2$, which means that they only scatter between momenta with equal values of ϕ. If so, then the simulation reduces to the cases already shown in Figs. 1.2 and 1.1.

On the other hand, we have yet to show the completely isotropic case, where the density of states is weighted uniformly along the Fermi surface. This we show in Figure 1.3. We refer to $\theta = 0$ as the antinode (where the gap is Δ), and $\theta = \pi/4$ as the node (where the gap is zero). As shown in Figs. 1.3(e) and 1.3(f), the kink appears at $\pm(\Delta + \Omega)$ independent of momentum. This is because when the density of states is weighted uniformly around the Fermi surface, it is dominated by the density of states at the antinode. In panel (g) we show the spectral density function integrated over momentum. Along the antinode, there is a clear gap in the density of states, and features appearing at the kink energies. However, along the node, the integrated spectral density function is completely constant.

In summary, simulations show that when electrons in a metal interact with a boson sharply peaked at energy Ω, a kink appears at energies $\pm\Omega$. The kink can be characterized by the MDCs, which follow Lorentzian curves. When there is an electron-boson interaction in a superconductor with a constant gap size, the kink instead appears at energies $\pm(\Delta+\Omega)$. The MDCs no longer have a simple form, although the momentum-integrated spectral weight does. When the superconducting gap depends on momentum, the position of the kink depends on momentum dependence of the density of states and the electron-boson scattering. In the case of an isotropic electron-boson interaction, the kink appears at $\pm(\Delta + \Omega)$.
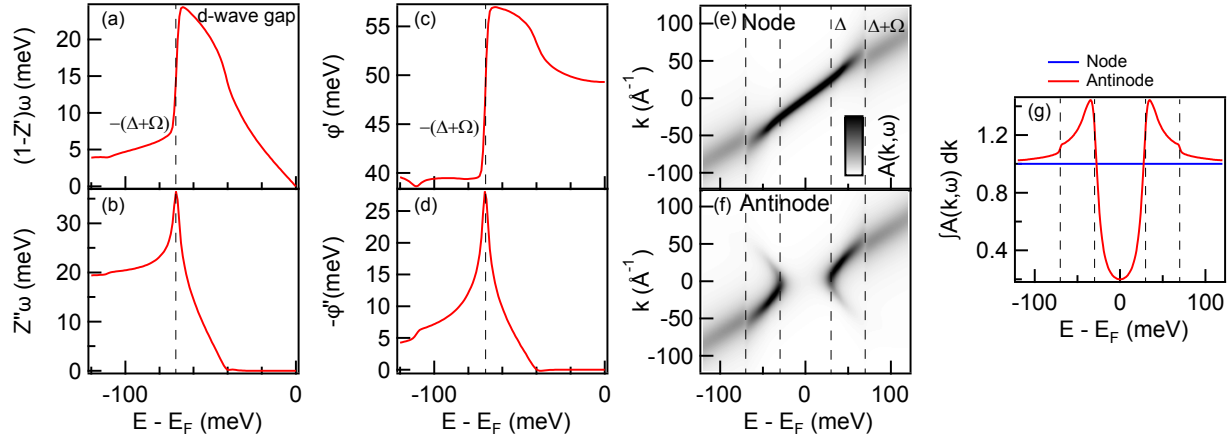
Figure 1.3. A simulation of the electron-boson kink in a superconductor with a momentum dependent gap, inspired by the momentum dependence in Cuprate superconductors.

1.2 Cuprate superconductors

1.2.1 Basic electronic structure

Cuprates are a class of materials that, when undoped, behave as antiferromagnetic insulators. However, when they are doped, they exhibit superconductivity at low temperatures. Some of the most commonly studied examples of cuprates are $YBa_2Cu_3O_{7-\delta}$ (YBCO), $La_{2-x}Ba_xCuO_4$ (LBCO), $Bi_2Sr_2CuO_{6+\delta}$ (Bi2201), and $Bi_2Sr_2CaCu_2O_{8+\delta}$ (Bi2212). Bi2212 is particularly ideal for ARPES experiments, and will be the subject of most of this work.

What all these materials have in common is a layered structure with at least one copper oxide (CuO_2) layer per unit cell. This layer is in a square lattice, with Cu at the corners of the unit cell, and O at the edges. In absence of any doping, the Cu atoms form 2+ ions, while the O atoms form 2− ions. The $4s$ orbitals of Cu^{2+} are unoccupied, and the $3d$ orbitals are fully occupied, except for a single hole. It is energetically favorable for the hole to occupy the $x^2 + y^2$ orbital, since it has lobes pointing towards the O^{2-} ions. These orbitals will also hybridize with the p orbitals of adjacent O ions, and the hole occupies the antibonding orbital. When cuprates are doped with holes, the additional holes occupy the same state with opposite spin.[9]

The most important aspect is that there is a strong repulsion between electrons on the same Cu site. The system is described by the Hubbard model, which has parameters t and U.[10] The large parameter U is the energy cost of two electrons occupying the same Cu site, while the small parameter t is the hopping integral between two adjacent Cu sites. In undoped cuprates, the electron states are half-filled, and the Hubbard U acts a barrier to electrical transport. Furthermore, electrons on adjacent sites prefer to have spins in opposite directions to allow virtual hopping between sites. Thus at low temperatures, undoped cuprates behave as antiferromagnetic insulators, called Mott insulators.
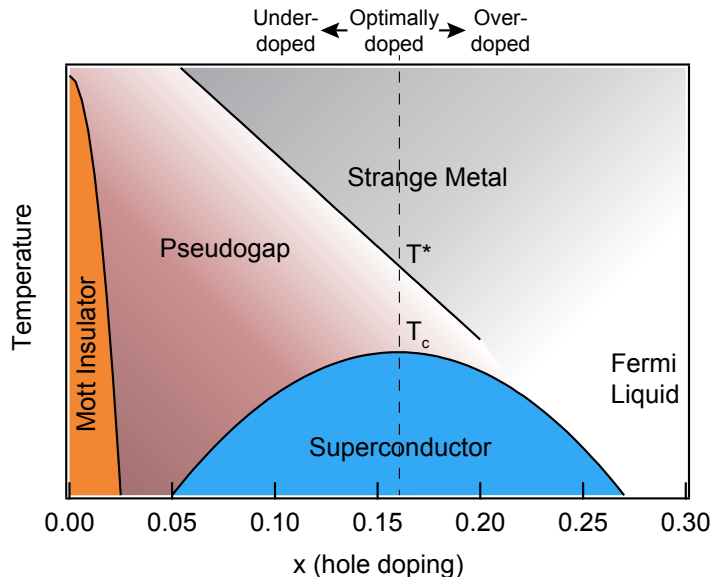
13

Figure 1.4. Schematic phase diagram of a cuprate. There are many other phases that could be shown in the phase diagram depending on the desired level of detail.

When cuprates are doped, the electron states are no longer half-filled, and they no longer behave like Mott insulators. As shown in the phase diagram in Fig. 1.4, there is a superconducting "dome" centered around 0.16 holes per unit cell. Samples at the center of the dome are called optimally doped (OP), while samples on the left side are called underdoped (UD), and samples on the right side are overdoped (OD). Above T_c, especially in underdoped samples, there is a pseudogap state, which will be discussed in Sec. 1.2.2. Above the temperature T^*, the pseudogap state gives way to a strange metal state, which does not follow the Fermi Liquid theory discussed in Section 1.1.5. Instead, a strange metal is described by Marginal Fermi Liquid Theory,[11] where the electron-electron self-energy is proportional to ω.

When electron states are no longer half-filled, the Hubbard model is notoriously difficult to solve. While BCS theory might lead us to believe that cuprate superconductivity is caused by some electron-boson interaction, some have argued that the Hubbard Model is sufficient to understanding cuprate superconductivity.[12] One of the major goals in the study of cuprates is to determine whether the Hubbard model is sufficient, or if an electron-boson interaction is necessary.

1.2.2 The gap and the pseudogap

Compared to conventional superconductors, there is an important difference in the gap parameter of cuprates. Namely, the gap parameter Δ_k is dependent on k, and even changes sign. This has been conclusively demonstrated by experiments with superconducting loops.[13] Normally the magnetic flux through a superconducting loop is quantized, because the phase

ϕ must change by $2\pi n$ around the loop. However, when the loop of cuprate superconductors is constructed in a particular way, there is an additional phase shift of π induced by the sign change of Δ_k.

In ARPES experiments, we cannot observe the phase of Δ_k, but we can directly measure the gap size, which is equal to the magnitude of Δ_k along the Fermi surface. The gap vanishes along the Γ–X direction ($k_x = k_y$), and this point on the Fermi surface is referred to as the node. The gap size is maximized near the M point at Brillouin zone boundary, and this point is called the antinode. In general, the gap is approximately proportional to $|cos(k_x) - cos(k_y)|$ (using units such that k=π at the Brillouin zone boundaries).[14] This is referred to as d-wave symmetry (not to be confused with the d orbitals of the Cu atoms).

The sign change in Δ_k is significant because it implies something about the $V_{k,k'}$ scattering amplitudes. When $V_{k,k'}$ scatters between states with the same sign of Δ_k, it must be relatively attractive, and when it scatters states with opposite sign of Δ_k, it must be relatively repulsive. In principle, superconductivity may be possible even with entirely repulsive interactions, as long as the interactions have the correct momentum dependence.[15] It is often thought that electron-phonon interactions, which are mostly isotropic, would not lead to a d-wave gap; however, electron-phonon interactions may be anisotropic.[16]

A shocking property of the gap in cuprates is that it appears to persist at temperatures where superconductivity is destroyed. The persistent gap, known as the pseudogap, persists up to the temperature T^* shown in Figure 1.4. ARPES experiments have demonstrated that in the pseudogap state, the gap is closed in a region near the node, and open near the antinode.[17,18,19,20,21] In underdoped samples, T^* is larger, the pseudogap is larger, and the pseudogap exists in a larger region of momentum space.[22] Plenty of experimental evidence suggests that the pseudogap appears not just in the pseudogap state, but coexists with the superconducting state in underdoped samples.[23,24,25,26,14,27]

In the pseudogap state, the Fermi surface, rather than forming a complete enclosed pocket, forms disconnected Fermi arcs. These Fermi arcs are unexpected because if the electronic band dispersion is a continuous function of momentum, disconnected arcs would not be possible. There are at least three points of view on how to reconcile the Fermi arcs with continuous bands. One view is that it is not a true gap, and that quasiparticles near the antinode are so decoherent that they appear as a gap.[28] Another view is that the pseudogap is a full d-wave gap, just like the superconducting gap, but the gap appears filled wherever the gap is sufficiently small, because of scattering.[29,30,31] If this is correct, then it suggests that there are fluctuating superconducting pairs above T_c, and that this may be the nature of the pseudogap state.[32]

A third view is that each Fermi arc is just one side of a full Fermi pocket. The other side of the Fermi pocket cannot be observed because the photoemission matrix elements are very small. This viewpoint may be motivated by any of several theories of the pseudogap as an order that is distinct from superconductivity.[33,34,35,36] For example, in the Yang-Rice-Zhang model,[36,37,38] the pseudogap doesn't disappear along the Fermi arc, but rather goes above the Fermi energy, where it cannot be seen by typical ARPES experiments. We refer to this as particle-hole asymmetry, because the pseudogap appears among the electron quasiparticles

and not among the hole quasiparticles. This is in contrast to the particle-hole symmetry of the superconducting gap, which is always centered at the Fermi energy. Some experiments have claimed to find evidence for particle-hole asymmetry in the pseudogap.[39,40,41,42]

In summary, the origin of the pseudogap is theoretically controversial, and the controversy is directly related to conflicting experimental results and interpretations. Most theories of the pseudogap also purport to explain the mechanism for superconductivity. The mystery of the pseudogap isn't the same as the mystery of superconductivity, but it is an extremely important piece of the puzzle.

1.2.3 Electron-boson kink

Because of the important role that electron-phonon coupling plays in conventional superconductors, researchers have devoted much effort to understanding any strong electron-boson coupling that might exist in cuprates. Indeed, there is abundant evidence that the electrons strongly couple to at least one bosonic mode, with an energy strongly peaked around 40–70 meV. The first sign of this bosonic coupling mode was a peak-dip-hump structure in the energy profiles of ARPES intensity.[43,44,45,46,47,48] More detailed investigation[49,50] revealed that the peak-dip-hump structure was just one aspect of the electron-boson dispersion kink. At this point, a major disagreement arose over the identity of the boson. Some have argued that the boson is a phonon,[49,51,52,53,54,55,56,16,57] while others have argued that it is a spin resonance.[46,58,50,59,60,61,62,63,64]

Some of the early arguments over the identity of the boson were based on the kink strength. The spin resonance is strongest in the superconducting state only, while the phonon mode persists above T_c. Along the nodal direction of momentum space, the kink has a similar strength in both the normal and superconducting states in all observed cuprate materials, and this supports the phonon interpretation.[49] On the other hand, further away from the nodal direction, the kink is much stronger in the superconducting state and nearly disappears in the normal state, supporting a spin resonance interpretation.[46,50,59,61,60]

Another line of evidence concerns the energy of the kink. As was discussed at length in Section 1.1.7, the energy of the electron-boson kink depends on the momentum dependence of the electron-boson scattering. In principle, if electrons are scattered towards the node, then the kink will appear at Ω; if electrons are scattered towards the antinode, then the kink will appear at $\Delta_{max} + \Omega$. If electrons are scattered towards all momenta, then the kink will appear at $\Delta_{max} + \Omega$, because the density of states is dominated by the antinode. What experiments find is that along the node, the kink is observed at 60–70 meV across a broad class of cuprates, in both the superconducting and normal states.[49] Away from the node, the kink is observed near 60 meV in OP Bi2212 samples in the superconducting state, but is observed near 40 meV in the normal state. Additionally, it is observed near 40 meV in superconducting OD Bi2212, and near 35 meV in OP Bi2201, both of which have smaller gaps than OP Bi2212.[51,55]

One interpretation is that the kink at momentum k appears at $\Omega + \Delta(k)$. This suggests

that quasiparticles near the node scatter towards other nodal points, while quasiparticles near the antinode scatter towards other antinodal points.[16,65,64] One specific proposal is that the antinodal kink is caused by the out-of-plane, out-of-phase O buckling phonon mode B_{1g}, which scatters between antinodal states, while the nodal kink is caused by in-plane Cu-O breathing phonon mode, which scatters between nodal states.[16] Another specific proposal is that the kink corresponds to spin fluctuations scattering to the opposite side of the Fermi surface.[64]

Another possible interpretation is that the nodal kink does in fact shift by Δ_{max}, but this shift is experimentally obscured by the presence of multiple phonon modes.[57,54] Another interpretation is that the nodal kink disappears above T_c, and is replaced by a similar feature caused by Marginal Fermi Liquid excitations.[58], although this is controverted by a more recent study.[53] We also note a recent observation showing that the kink remains at the same energy both above and below T_c at all momenta.[66,67] If this observation is correct than it poses a challenge to all of the interpretations mentioned so far.

This has been only brief overview of the controversies regarding superconductivity, the pseudogap, and the electron-boson kink in cuprates. We do not yet know the mechanism for high-temperature superconductivity, nor the mechanism for the pseudogap. We do not know whether electron-boson coupling is involved in the mechanism, and we do not know the identity of the boson. All of these are deep questions that cannot be answered by this work alone, but we hope to address them in new ways with new experiments.

Chapter 2

Analysis techniques

Angle-resolved photoemission spectroscopy (ARPES) is a standard method of measuring electronic structure in materials. Time-resolved ARPES (TARPES) is a more recent method that measures electronic structure as a function of time, in response to a laser pulse. Both of these techniques have been discussed extensively.[19,68,69,70] In Section 2.1 we briefly review the theory of ARPES. In Section 2.2, we discuss the TARPES technique. And in Section 2.3, we discuss the highlights of previous TARPES experiments on cuprate superconductors.

2.1   Theory of ARPES

At its most basic, ARPES is an experiment that hits a material with photons, and measures the electrons that are ejected. Ejected electrons escape with a certain angle and velocity. By using conservation of momentum and energy, it is possible to calculate the initial energy and momentum of the electrons. The conservation of energy says that

$$E_i - \mu = E_{\text{kin}} - h\nu - \Phi_A \qquad (2.1)$$

where $E_i - \mu$ is the initial energy of the electron relative to the chemical potential, E_{kin} is the kinetic energy of the electron when it reaches the detector, $h\nu$ is the energy of the photon, and Φ_A is the analyzer workfunction. The workfunction is discussed in more detail in Section 3.1.

The momentum of the incident photon is negligible compared to that of the electron, so we can say that the momentum of the electron parallel to the escape surface ($k_\parallel$) is unchanged by the photoemission process. $k_\parallel$ is related to the angle of photoemission by

$$k_\parallel = \sqrt{2mE_{\text{kin}}} \sin\theta / \hbar. \qquad (2.2)$$

Momentum that is perpendicular to the escape surface $(k_\perp)$ is not conserved because of the fields perpendicular to the surface. The only way to infer the initial $k_\perp$ is by using a more complicated measurement scheme.[71] Fortunately, cuprate superconductors are made up of weakly coupled two-dimensional layers, and so the electrons do not have a strong dependence on $k_\perp$.

It is not entirely accurate to say that we are calculating the initial energy and momentum of the electrons. In a system where electrons interact with one another, the energy and momenta of individual electrons are not well-defined. When an electron is ejected from the sample, conservation of charge requires either the creation of a holelike quasiparticle, or the annihilation of an electronlike quasiparticle, and this may be accompanied by other charge-neutral excitations. A standard method of analysis is to take the full N-particle wavefunction $|\psi^N\rangle$, and separate it into the single particle wavefunction $|\phi\rangle$ containing the ejected electron, and the wavefunction containing the other N-1 electrons, $|\psi^{N-1}\rangle$. Using Fermi's golden rule, the ARPES intensity is proportional to

$$I(k,\omega) = \sum_m |\langle\phi_f|H_{\mathrm{int}}|\phi_i\rangle|^2 |\langle\psi_m^{N-1}|\psi_i^{N-1}\rangle|^2 \delta(\omega + E_f^{N-1} - E_i^N - h\nu), \qquad (2.3)$$

where k and ω are the final momentum and energy of the ejected electron in $|\phi_f\rangle$. The term $|\langle\phi_f|H_{\mathrm{int}}|\phi_i\rangle|^2$ is referred to as the ARPES matrix elements, and it depends on the particulars of the experimental geometry and light polarization. In a typical experiment, the ARPES matrix elements are approximately constant over a single measurement, and thus they can be ignored.

Excluding the matrix elements, the rest of the Eq. (2.3) can be expressed in terms of the electron removal Green's function. The Green's Function from Eq. 1.15 can be expressed as

$$G^-(r,r',t,t') = i\sum_m \langle\psi_i^N|c^\dagger(r',t')|\psi_m^{N-1}\rangle\langle\psi_m^{N-1}|c(r,t)|\psi_i^N\rangle\Theta(t'-t). \qquad (2.4)$$

When we apply the annihilation operator to $|\psi_i^N\rangle$, the result is $|\psi_i^{N-1}\rangle$ by definition. When we apply a Fourier transform, the resulting Green's function is

$$G^-(k,\omega) = i\sum_m \frac{|\langle\psi_m^{N-1}|\psi_i^{N-1}\rangle|^2}{\omega + E_f^{N-1} - E_i^N - h\nu - i0^+}. \qquad (2.5)$$

From here it is trivial to show that the ARPES intensity is equal to $\mathrm{Im}G^-(k,\omega)$, multiplied by the ARPES matrix elements. In the Nambu-Gor'kov formalism discussed in Section 1.1.6, we replace G^- with G_{11}^-.

If, instead of taking the imaginary part of G^-, we take the imaginary part of the full Green's function G, the result is the spectral density function, $A(k,\omega)$, which was simulated in Section 1.1.7. The ARPES intensity is equal to the spectral density function, multiplied by the ARPES matrix elements, multiplied by the distribution function of the electron states. At thermal equilibrium, the distribution function is simply the Fermi-Dirac function. Because the distribution function decreases exponentially above the Fermi energy, it is very difficult for ARPES to measure the spectral density function above the Fermi energy.
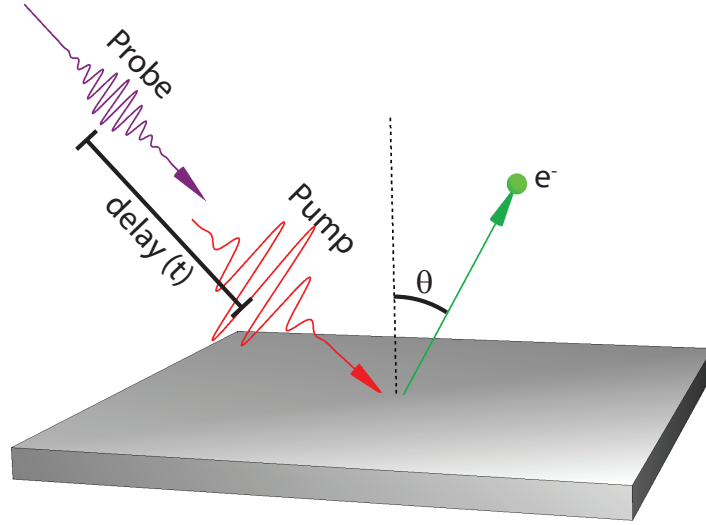
Figure 2.1. A diagram of the time-resolved ARPES measurement scheme.

2.2 Time-resolved ARPES

TARPES is a technique that combines the strengths of ARPES with the strengths of time-resolved spectroscopy. The goal is not just to measure the spectral density function, but also observe how it responds over time to a perturbation. The perturbation arrives in the form of a laser pulse, called the pump pulse. After a small delay, the pump pulse is followed by another laser pulse, called the probe pulse, that photoemits electrons to be measured.

The present work uses a TARPES instrument that has been described in Refs. 68 and 70. The pump pulse is the fundamental mode of a Ti:Sapph laser. It is in the near infrared range, and has an energy of 1.5 eV. The probe pulse is created by fourth harmonic generation, and is the ultraviolet range, near 6 eV. The workfunction of a cuprate is near 4.5 eV, which means that the probe can photoemit electrons and the pump cannot. The pump and probe pulses have a variable repetition rate, usually set near 500 kHz. It is common to characterize the pump and probe pulses by their fluences, which is a measure of the average energy per unit area per pulse. The beam spot size of the probe pulse is around half the diameter of that of the pump pulse, such that the fluence is nearly constant within the region of measurement. The time resolution is about 300 fs, the energy resolution is about 20 meV, and the momentum resolution is about 0.001 Å^{-1}.

Although TARPES is a relatively new technique, it has already found a variety of experimental applications. TARPES can be used to generate coherent oscillations, incoherent excitations, and entirely new states of matter. Additionally, since TARPES pushes the system out of equilibrium, it is not limited by the Fermi-Dirac distribution, and can detect the spectral density function well above the Fermi energy.[69]

2.3 TARPES experiments on cuprates

Here we review some highlights from extant TARPES experiments on cuprate supercon-ductors. In optimally doped Bi2212 at low temperatures, the superconducting gap closes inside the Fermi arc region when the pump fluence is above a critical value of about 15 μJ/cm^2.[72,73,74,75,76,77] Outside the Fermi arc region, the gap doesn't close until the fluence is at least 40 μJ/cm^2.[76] The critical fluence of 15 μJ/cm^2 is consistent with a back-of-the-envelope estimate of the condensation energy of the Cooper pairs.[78] The natural conclusion is that 15 μJ/cm^2 is sufficient to destroy the superconductivity and leave a pseudogap state remaining, and 40 μJ/cm^2 is sufficient to also destroy the pseudogap state. To a first-order approximation, this is similar to what happens to superconducting cuprates as their tem-perature is raised above T_c and T^*, respectively.

However, it is important to remember that the sample is not at thermal equilibrium, and there may be differences between a transient pumped state and an equilibrium heated state. This was demonstrated by an early study on the dynamics of the quasiparticle population upon pumping a superconducting Bi2212 sample with a 100 μJ/cm^2 pulse.[79] At first, elec-trons have a nonthermal distribution, but they settle into a thermal distribution within 50 fs. On a timescale of 110 fs, electrons exchange energy with certain "hot" phonon modes that couple strongly to electrons. After 330 fs, they reach a common temperature. On a timescale of 2 ps, the electrons and hot phonons relax by scattering with cold phonon modes, and they reach a common temperature by 6 ps. After that, heat diffusion occurs on a nanosecond timescale.

Other studies on the quasiparticle population have found that below the critical fluence, the quasiparticle relaxation rate increases with fluence, and increases away from the node.[72] This is suggestive of bimolecular recombination into Cooper pairs, and it also suggests that Cooper pair formation is faster away from the node. Studies looking above the critical fluence found that nodal quasiparticles decayed much faster while superconductivity was suppressed,[74,80,76] which could be explained by the phase space restrictions imposed by the gap.[81] Studies of the energy-dependent decay rate have found that nodal quasiparticles above about 70 meV decay more quickly than those below 70 meV, which reinforces the idea that electrons couple to a 70 meV bosonic mode.[82,83] Note that in all cases, the timescales of the quasiparticles far exceed the timescales that would be predicted from the width of the spectral peaks, and this is not yet understood.[82]

Other studies have looked at the nodal dispersion kink (previously discussed in Section 1.2.3) and its response to pumping.[84,85,75] The major result is that the kink is suppressed in correlation with the suppression of the superconducting gap. Below the critical fluence, both the kink and the superconducting gap are suppressed more and more with increasing fluence. Above the critical fluence, the superconducting gap is fully suppressed, and the suppression of the kink saturates. Additionally, the recovery timescale of both the kink and the gap are similar. This evidence does not prove that the nodal electron-boson coupling is behind superconductivity, but it does suggest that the nodal kink strength is enhanced in the superconducting state, and this enhancement occurs on subpicosecond timescales.

Studies of the kink away from the node have proven difficult, because the presence of the superconducting gap can invalidate standard MDC analysis.

TARPES has proven very useful for studying cuprate superconductors. Sometimes it is simply a convenient way to compare superconducting and non-superconducting states very quickly, keeping in mind that the system is out of equilibrium and that some degrees of freedom are at different temperatures. It can also be used to study the dynamics of the quasiparticle population, or the dynamics of the bosonic kink. The theme of the subsequent chapters is to expand the range of TARPES experiments on cuprates, by studying aspects that had previously been ignored.

Chapter 3

Chemical Potential Dynamics and the Pseudogap

One approach to TARPES is to study the same properties of a material that are traditionally studied at equilibrium with ARPES, using the laser pump power and the delay time as two additional tuning parameters. For example, in cuprate superconductors, the pseudogap has been of particular interest, because different theories of high-temperature superconductivity suggest different origins and shapes of the pseudogap.

However, here we adopt a different approach, examining a property which is traditionally ignored at equilibrium: the chemical potential. Although we did not initially know where this study would lead, it became clear that chemical potential provides important information about the pseudogap structure above the Fermi energy. This is significant because ARPES typically has difficulty making measurements above the Fermi energy, and this has allowed for the development of competing theories of the pseudogap which make distinct predictions.

This chapter is based on two studies,[86,87] although here we describe them in greater detail and follow a more chronological narrative. In Section 3.1, we discuss some background on the chemical potential. In Section 3.2, we describe our initial observations. In Section 3.3, we formulate hypotheses about the mechanism. In Section 3.4, we discuss further results and analysis, contextualizing them within the most likely hypotheses. In particular, we explain the implications on the pseudogap. Finally, in Section 3.5, we discuss the future directions of this line of inquiry.

3.1 Introduction

A grand canonical ensemble is a system that is at equilibrium with a reservoir with which it can freely exchange energy and particles. The chemical potential, denoted μ, is the energy lost by the ensemble when it gives up one particle to the reservoir. Here, the particles in question are electron quasiparticles. Because these quasiparticles are Fermions, at equilibrium they obey the Fermi-Dirac distribution:

$$f(E - \mu, T) = \frac{1}{1 + e^{(E-\mu)/(k_B T)}}. \tag{3.1}$$

T is the temperature of the system, and k_B is the Boltzmann constant. The function $f(E - \mu, T)$ determines the occupation fraction of a single quasiparticle state at energy E.

The chemical potential is commonly confused with the Fermi energy, denoted E_F. In fact, the Fermi energy is defined to be the chemical potential at zero temperature. As we will discuss later, the chemical potential changes upon increasing temperature.

Because the chemical potential is an energy, it is only meaningful to talk about its value relative to some other energy level. It is common to talk about the sample workfunction Φ_S, which is the energy required to transport an electron from the chemical potential to the vacuum immediately outside the sample. Another common concept is the analyzer workfunction Φ_A, which is the energy required to transport an electron from the chemical potential to the vacuum near the detector. However, definitions of the workfunction vary among sources, so to avoid ambiguity, we will instead refer to μ_{vac}, the chemical potential relative to the vacuum level outside the sample. We will also discuss the chemical potential relative to the valence band energy, μ_ε.

One technique to measure the chemical potential is the Kelvin probe. In fact, there have been a few Kelvin probe studies on cuprate superconductors, looking at how the chemical potential changes with temperature.[88,89,90,91] Unfortunately the Kelvin probe technique suffers from two weaknesses. First, the chemical potential may drift over the course of the measurement due to adsorption of gas molecules onto the sample surface. This makes it difficult to determine the exact dependence on temperature. Second, the Kelvin probe technique only measures μ_{vac}, and is not capable of measuring the valence band energy. If the chemical potential and valence band shift together, that could have a vastly different interpretation from a chemical potential that shifts alone.

Despite the weaknesses of the Kelvin probe technique, ARPES is rarely used as an alternative. One problem with ARPES is that it can only measure the chemical potential in certain samples, ones where the electronic structure crosses the chemical potential. While this applies to cuprate superconductors, it cannot be applied to semiconductors or other fully gapped materials. ARPES does allow for measurement of the valence band energy, but does not resolve the problem of drifting chemical potential. In fact, the drift problem is exacerbated in ARPES, because slight variations in laser power lead directly to variations in chemical potential via the space charge effect.

TARPES finally resolves the drift problem. Rather than taking hours to change the temperature of the sample, the sample reacts to laser pulses on a picosecond timescale. During

this time, the adsorption of gases and fluctuation in laser power are negligible. Technically speaking, the relevant timescale isn't the reaction time of the sample, but the time it takes for the instrument to adjust its tuning parameters. But this can still be done sufficiently quickly, on a timescale of minutes or seconds. TARPES does introduce a problem of a different sort: the chemical potential is only a property of equilibrium systems. Nonetheless, in non-equilibrium measurements it is often possible to fit the electron distribution to Eq. (3.1), defining a quasi-thermal chemical potential.

Given these advantages, there has been a recent growth of TARPES studies looking at chemical potential in a variety of materials.[92,93,94,95,96,97,98,99,84] These studies have uncovered a great variety of different physics, including coherent phonons, charge transfer between bulk and surface bands, and the surface photovoltage effect. These various mechanisms will be discussed in greater depth when we search for interpretations of our own data in Section 3.3.

3.2 Initial observations

3.2.1 Measuring chemical potential and valence band energy

We begin by demonstrating the basic technique to measure the chemical potential and valence band energy. The first step is to measure Bi2212 along the Γ–Y direction, also called the nodal direction. An ARPES intensity map of a sample at equilibrium at 35 K is shown in Fig. 3.1(a). In the nodal direction, the superconducting gap vanishes, which is a necessary condition to measuring the chemical potential.

To measure the valence band energy, the quasiparticle dispersion (black curve) is extracted using the standard method of fitting momentum distribution curves (MDCs) to Lorentzian curves.[7] The sample is pumped with a 20 μJ/cm^2 laser pulse, and the transient dispersion (0.7 ps delay after the pump pulse) is compared with the equilibrium dispersion (Fig. 3.1(b)). In the 130–200 meV binding energy range, the dispersion shifts by about 5 meV. We denote this shift $\Delta\varepsilon$.

Throughout this study we measure $\Delta\varepsilon$ from the 130–200 or 150–200 meV energy range, because if we were to use lower binding energies, the measurement would be confounded by changes in the shape of the dispersion, as shown in Fig. 3.2. Near 70 meV, the shape of the dispersion is shaped by the electron-boson kink, which is known to be suppressed by pumping.[84,85,75] Near 0 meV, there is an apparent distortion in the dispersion due to the instrumental energy resolution.[100] This latter distortion is strongest when the instrumental resolution is large compared to the electronic temperature, and is therefore reduced upon pumping. Incidentally, other investigators have measured shifts in the valence band by looking near 0 meV;[84] while this analysis may be valid at the high temperatures used in that study, we caution against its use at lower temperatures.

Figure 3.1(c) shows how we measure the chemical potential, by integrating the ARPES intensity over a small momentum range (double arrow in panel (a)). Following Ref. 73, we
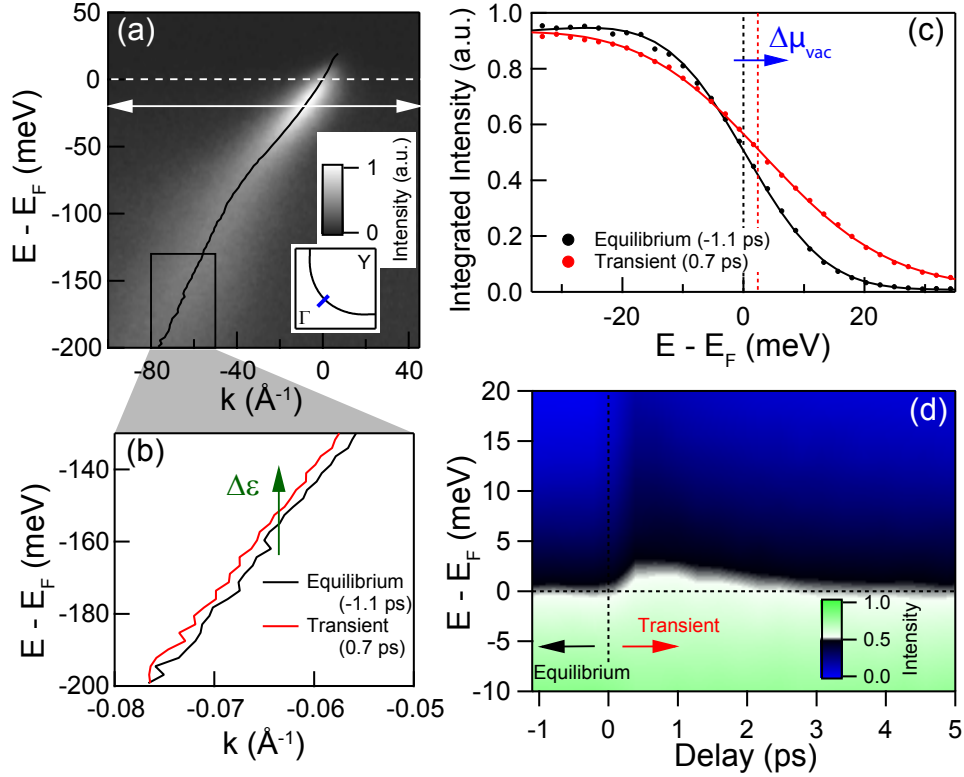
Figure 3.1. Measuring the chemical potential. (a) The ARPES intensity map of optimally doped Bi2212 at 35 K along the cut shown in the inset. (b) The valence dispersion of the sample in (a), between 130 and 200 meV binding energy, both before and after the arrival of a 20 μJ/cm^2 pump pulse. (c) The ARPES intensity integrated along the momentum range indicated by the white double arrow in (a), both before and after the pump pulse. Solid lines show fits to Fermi-Dirac functions, and dashed lines show the chemical potential from the fits. (d) The integrated ARPES intensity as a function of the delay time between the pump and probe.
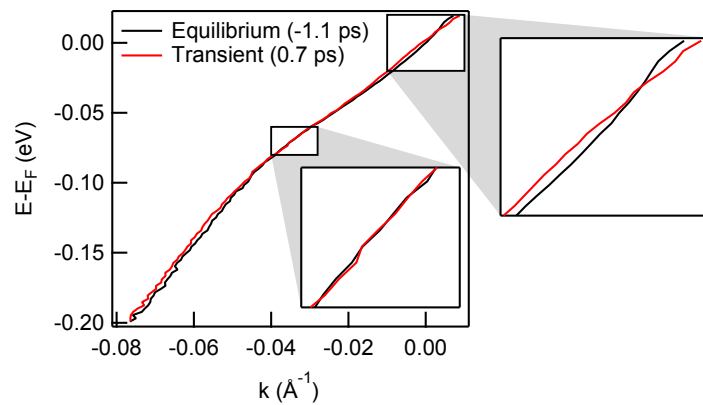

Figure 3.2. Distortions in the dispersion shape. Although there is a clear shift in the dispersion near 150, the shift is obscured at 70 and 0 meV because of changes in the dispersion shape. The data shown here is the same as in Fig. 3.1.
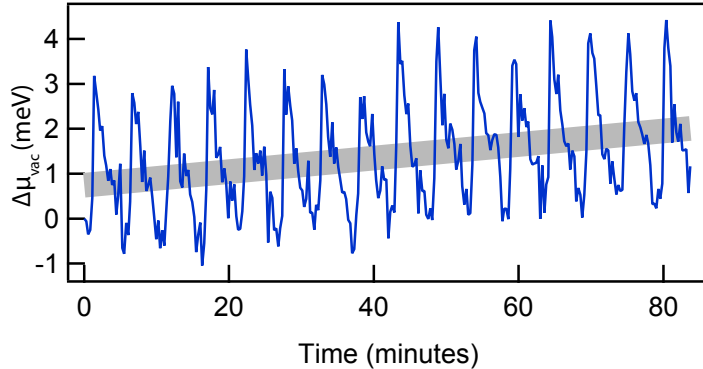
26

Figure 3.3. Drift in chemical potential.

fit the resulting intensity curve $I(E)$ to

$$I(E) = \left[\frac{C_0 + C_1(E - \mu_{\mathrm{vac}})}{\exp(\frac{E-\mu_{\mathrm{vac}}}{k_B T_e}) + 1} + C_2 + C_3 E\right] \otimes R(E). \tag{3.2}$$

Here, R(E) is a Gaussian resolution function with a fixed FWHM of about 23 meV (calibrated separately in each experiment). C_0, C_1, C_2, C_3, T_e, and μ_{vac} are fit parameters. We use our physical understanding of these parameters to determine which should vary freely or be held fixed over the course of a single measurement. C_2 and C_3 are related to the background noise present even when the laser is blocked, and should thus be held constant. C_0 and C_1 are allowed to vary freely because they both depend on the laser power, which can fluctuate throughout the measurement. However, the ratio C_1/C_0 is held constant within each measurement, because it arise from the slope in the density of states and/or the slope in the camera sensitivity.

Since the sample is not in equilibrium, there is no guarantee that it would fit to a Fermi-Dirac distribution. Nonetheless, Eq. (3.1) fits all our data well. This is consistent with previous studies which have shown that it takes 50–100 fs for electrons to reach a quasithermal distribution,[79,101] which is shorter than the 300 fs time resolution of this instrument. Thus, it makes sense to interpret the parameters T_e and μ_{vac} as the temperature and chemical potential of the electrons, respectively. The chemical potential μ_{vac} clearly increases by about 2.5 meV in response to the pump, and the electronic temperature T_e increases from 35 to about 100 K (not shown). In Figure 3.1(d) we show the integrated intensity as a function of delay time, visually illustrating that μ_{vac} increases and then relaxes over a few picoseconds.

Previously, we discussed the possibility that the chemical potential will drift over time because of adsorption of gas and variation in laser power. We directly monitor this drift in each measurement. A typical example is shown in Fig. 3.3. Here the instrument is programmed to go through a cycle about once every five minutes. It is clear that pumping causes a change in the chemical potential, and that this is repeatable in each cycle. Superimposed upon this change is the slow drift traced by the thick gray line. We correct for the drift by fitting it to a straight line.
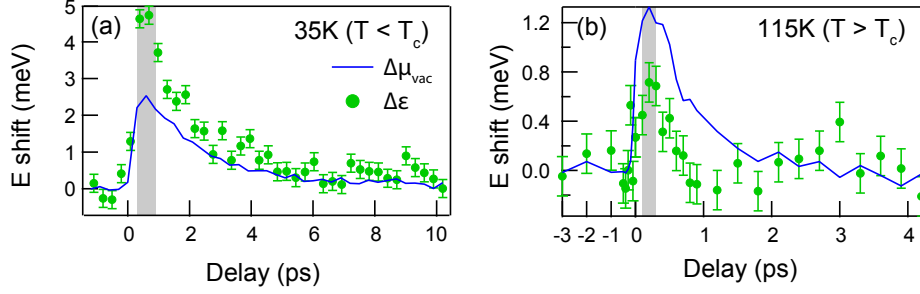
Figure 3.4. The change in chemical potential ($\Delta\mu_{vac}$) and the shift in quasiparticle dispersion ($\Delta\varepsilon$) relative to the vacuum energy in response to a 20 μJ/cm^2 pump pulse at 35 K (a) and 115 K (b).
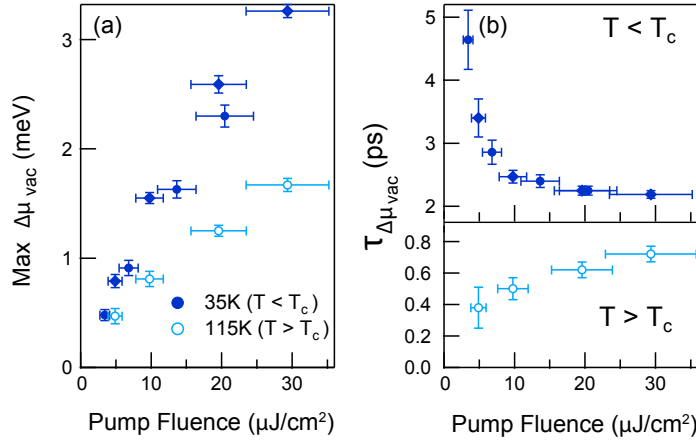

Figure 3.5. Pump fluence dependence of chemical potential. (a) The maximum shift $\Delta\mu_{vac}$, determined by averaging over the gray bars in Figure 3.4. (b) The recovery rates of $\Delta\mu_{vac}$, as determined by simple exponential fitting after 0.6 ps.

To summarize our findings so far, we have measured the shift in the valence band energy, $\Delta\varepsilon$, and the shift in chemical potential, $\Delta\mu_{vac}$. In this first measurement, laser pumping caused a shift of $\Delta\varepsilon \sim 5$ meV and $\Delta\mu_{vac} \sim 2.5$ meV. This presents two mysteries. Why are these quantities nonzero? And why are they different from each other?

3.2.2   Delay and pump fluence dependence

Figure 3.4 shows $\Delta\mu_{vac}$ and $\Delta\varepsilon$ together as a function of delay time in the superconducting (panel (a)) and normal (panel (b)) states of optimally doped Bi2212. Both quantities increase upon pumping and recover exponentially with a timescale of $\sim$2 ps in the superconducting state ($<$1 ps in the normal state). Note that in the superconducting state, $\Delta\mu_{vac} < \Delta\varepsilon$, while in the normal state $\Delta\mu_{vac} > \Delta\varepsilon$. The significance of this difference will be discussed much later in Section 3.4.2.
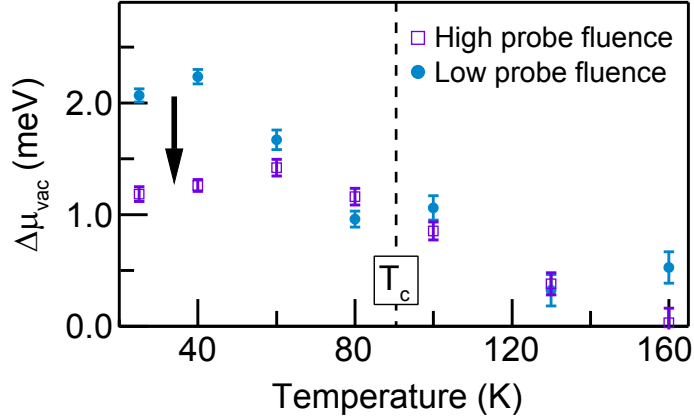
Figure 3.6. The shift in $\Delta\mu_{\mathrm{vac}}$, 0.6 ps after a 15 μJ/cm^2 pulse, as a function of temperature. Results are shown for low probe fluence (10^6 electrons/cm^2/pulse or 3 nJ/cm^2) and high probe fluence (3×10^6 electrons/cm^2/pulse or 9 nJ/cm^2).

Focusing just on $\Delta\mu_{\mathrm{vac}}$, we perform a systematic study of delay time, temperature, and pump fluence in Figure 3.5. Panel (a) shows the maximum $\Delta\mu_{\mathrm{vac}}$ in the superconducting and normal states as a function of pump fluence. $\Delta\mu_{\mathrm{vac}}$ is observed to be larger in the superconducting state, and to increase with pump fluence. Panel (b) shows the recovery time of $\Delta\mu_{\mathrm{vac}}$, as determined by a simple exponential fit from 0.6 ps delay time onwards. In the superconducting state, the recovery time becomes shorter at greater pump fluences, saturating at about 2 ps. In the normal state, the recovery is less than 1 ps, and becomes longer at greater pump fluences.

3.2.3 Probe fluence dependence

One of the most surprising observations about $\Delta\mu_{\mathrm{vac}}$ is that it depends not just on the pump fluence, but on the probe fluence as well. Figure 3.6 shows the temperature dependence of $\Delta\mu_{\mathrm{vac}}$, taken at 0.6 ps after the incidence of a 15 μJ/cm^2 pump pulse, using both high (9 nJ/cm^2) and low (3 nJ/cm^2) probe fluence. In the superconducting state, $\Delta\mu_{\mathrm{vac}}$ is observed to decrease with probe fluence.

The probe fluence is directly proportional to the number of electrons ejected per laser pulse, with a constant of proportionality that has been measured empirically.[68] So if $\Delta\mu_{\mathrm{vac}}$ changes with probe fluence, that implies a dependence on the number of electrons ejected. This must be the result of the interactions between electrons after they have been ejected. In equilibrium ARPES, such interactions are understood to create the space and mirror charge effects, which together have a large effect on the measured chemical potential.[102,103] However, our TARPES observations cannot be the result of a simple space or mirror charge effect. Recall that $\Delta\mu_{\mathrm{vac}}$ is defined as the difference between two measurements, one taken before pumping and one taken after pumping. In both measurements, the probe fluence is
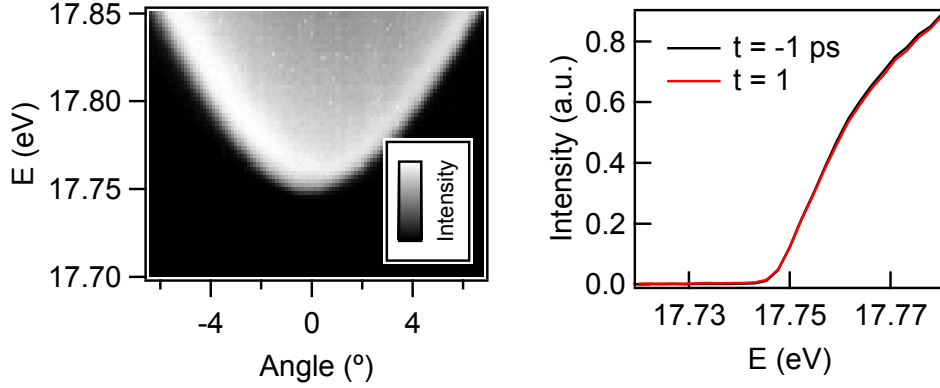
Figure 3.7. Low energy cutoff. (a) A sample of Bi2212 at 30 K which has been biased by about 18 V compared to the detector. The measurement is taken at Γ. (b) The intensity in (a) integrated over angle, shown before and 1 ps after a 24 μJ/cm^2 pump pulse.

the same. Therefore, when we see a change in $\Delta\mu_{\text{vac}}$, it cannot just be the result of a probe fluence. Instead it must depend on the product of the probe fluence and pump fluence.

Regardless of the mechanism, it is clear that the probe fluence dependence is related to some interaction between electrons after ejection. So this change in $\Delta\mu_{\text{vac}}$ cannot be intrinsic to the sample (although the fact that it appears only in the superconducting state suggests that it may be influenced by the sample's intrinsic properties). Therefore, in the rest of this study, we minimize the effect of probe fluence by discarding all data with high probe fluence, using only data with low fluence (3 nJ/cm^2 or less).

3.2.4 Low energy cutoff

We add one final observation which could be used as a clue to the physics. In Figure 3.7(a), we show a Bi2212 sample measured at 30 K at the Γ point. However, this sample has been biased by almost 18 V relative to the detector. The lowest energy electrons visible in the image correspond to those electrons that had just enough energy to escape the sample with zero kinetic energy left over. After having escaped, they are accelerated towards the detector, ultimately gaining 18 eV in kinetic energy. The minimum visible energy is called the low energy cutoff.

Once we have measured the low energy cutoff, the natural question is whether it changes upon pumping. We take the intensity in Fig. 3.7(a), and integrate over momentum. We repeat this procedure for measurements taken before and 1 ps after a 24 μJ/cm^2 pulse. As shown in Figure 3.7(b), there is little or no difference before and after pumping. Fitting suggests that the shift is –0.2 meV, which is within error of zero. For comparison, $\Delta\mu_{\text{vac}}$ was observed to be +3 meV in the same sample under the same conditions.

3.3   Hypotheses

In Section 3.2 we established the basic observations of $\Delta\mu_{\text{vac}}$ and other energy shifts. These observations present a number of mysteries: (a) $\Delta\mu_{\text{vac}}$ is nonzero, (b) the valence band shift $\Delta\varepsilon$ is nonzero, (c) $\Delta\mu_{\text{vac}}$ is not the same magnitude as $\Delta\varepsilon$, (d) $\Delta\mu_{\text{vac}} - \Delta\varepsilon$ changes sign across T_c, (e) in the superconducting state, $\Delta\mu_{\text{vac}}$ depends on probe fluence, and (e) the low energy cutoff has little or no shift.

In this section we will consider many different hypotheses to explain these observations. No single hypothesis will suffice to explain all of them, but we will eventually find satisfactory explanations for each one. Although a few of the discussed hypotheses will be completely discarded, this overview could serve as a starting point for the interpretation of future TARPES studies.

3.3.1   Sequestration of charge

We first consider a mechanism inspired by studies of the chemical potential in the topological insulator Bi_2Se_3.[94,95,96,97] In these samples, there is a distinction between the bulk states and surface states. Upon laser excitation, hole-like quasiparticles are created in the surface states, and electron-like quasiparticles are created in the bulk states. It takes some time for bulk quasiparticles to trickle back into the surface states. In the mean time, the chemical potential of the bulk and that of the surface states become decoupled, and shift by as much as 120 meV.

The general mechanism here is that electrons are sequestered, either in a different location, a different momentum, or a different energy. While the electrons are sequestered, charge is not conserved, and thus it is unsurprising that the chemical potential has changed. This mechanism is difficult to rule out, but studies suggest that Bi2212 is unlike Bi_2Se_3 in that the quasiparticles decay and thermalize very quickly.[79,72] The surface states are not distinguished from the bulk states, so there aren't any obvious metastable quasiparticle states. So we tentatively rule out this hypothesis.

3.3.2   Lattice distortion

Next we consider a mechanism inspired by studies of the chemical potential in iron-based superconductors $BaFe_2Se_2$ and $EuFe_2Se_2$.[92,93] In these studies, the chemical potential is observed to oscillate with a frequency equal to that of coherent $A_{1g}(\text{As})$ phonons. This suggests that distortions in the lattice transform the electronic structure enough that it changes the chemical potential.

In the case of our studies on Bi2212, there is no evidence for oscillations in chemical potential, so there is no basis to attribute the behavior to coherent phonons. It is also worth
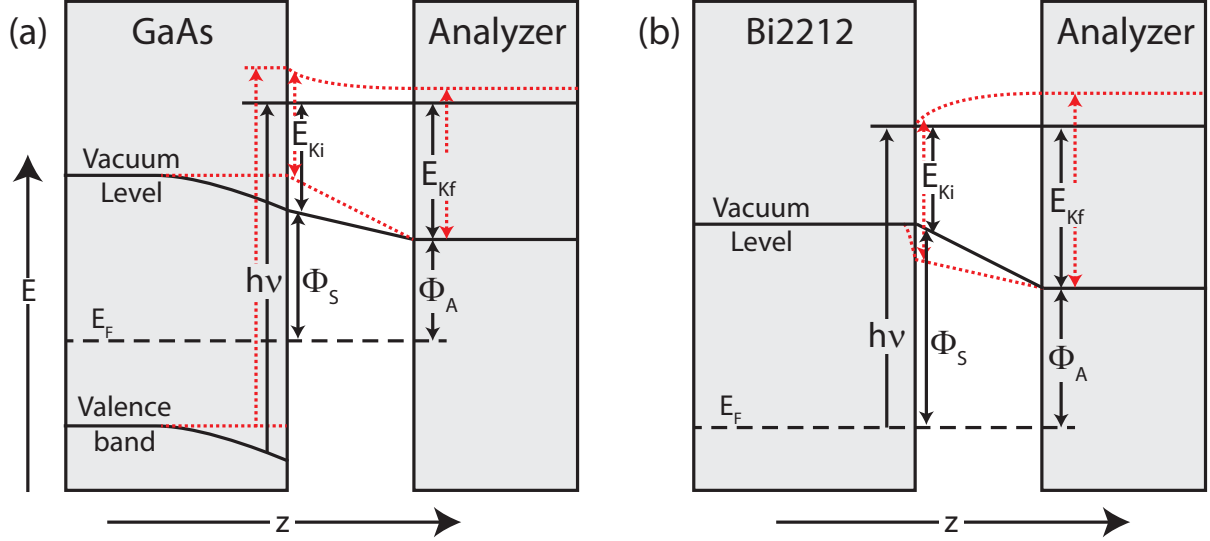
Figure 3.8. A schematic drawing of the surface photovoltage effect in GaAs (a) (adapted from Ref. 98) and the surface potential barrier in Bi2212 (b). Upon absorption of a photon, electrons in the valence band (or at the Fermi energy) are excited by energy $h\nu$, and escape the sample with initial kinetic energy E_{ki}. The final kinetic energy upon reaching the detector is E_{kf}. The z axis represents the distance from the sample. The dotted red lines indicate changes that occur when the sample is pumped with light before photoemission.

noting that the studies on iron-based superconductors use much higher pump fluences, up to 2 mJ/cm², in contrast to our fluences up to 30 μJ/cm².

However, there may be an overall lattice expansion simply due to quasi-thermal heating. If the crystal lattice should expand, this would cause the entire Brillouin zone to shrink, causing a shift in the dispersion. To rule out the mechanism of lattice expansion, we make a rough estimate of the magnitude of the effect. We first make the generous assumption that the lattice is at equilibrium with the electronic temperature, even though experiments indicate that it is lower.[79] In a typical measurement, the electronic temperature increases from 20 K to 115 K, which corresponds to a lattice expansion of 0.026%,[104,105] which corresponds to a $\Delta\varepsilon$ of only 0.18 meV. This is insufficient to account for our observations.

3.3.3   Surface potential barrier

During the photoemission process, all electrons cross a potential barrier as they escape the sample. If the magnitude of this potential barrier were to change, for example by changing the dipole moment near the surface, then it would affect the energy of all ejected electrons. Specifically, it would cause an equal shift in both $\Delta\mu_{\text{vac}}$ and $\Delta\varepsilon$. It is difficult to predict exactly how large this shift would be, but it is likely to be a small fraction of the total potential barrier, which is about 4.5 eV.

The surface potential barrier is more complex than it may first seem, because it may induce time-dependent electric fields which affect electrons while they are travelling between the sample and the detector. It is useful to compare the case of Bi2212 to TARPES studies on GaAs.[98,99] In GaAs, rather than measuring the chemical potential, studies have looked at the shift in the valence band energy. As illustrated in Fig. 3.8(a), the valence band energy bends downwards near the surface of the sample. This bending is mitigated by pumping, and this is known as the surface photovoltage effect. In the case of Bi2212 (see Fig. 3.8(b)), there is no bending of the valence band energy near the surface. However, there is a dipole moment at the surface, which implies a change in the vacuum energy level immediately outside the sample.

When the electrons are ejected from the sample, they have some initial kinetic energy E_{ki}, which is determined by the difference between the electron energy and the vacuum energy. When GaAs is pumped, E_{ki} does not change, because both the valence band and vacuum energy change by the same amount; when Bi2212 is pumped, E_{ki} increases because of a change in the dipole moment at the surface.

When the electrons reach the detector, they have final kinetic energy E_{kf}. The final kinetic energy differs from the initial kinetic energy for two reasons. First, the detector has a different potential energy than the vacuum near the sample. Second, electrons may gain or lose energy in the time-dependent potential. The final kinetic energy is given by

$$E_{kf} = E_{ki} - e \int_{t_i}^{t_f} \frac{\delta \Phi(z(t), t)}{\delta z} \frac{\mathrm{d}z(t)}{\mathrm{d}t} \mathrm{d}t, \qquad (3.3)$$

where Φ is the electric potential as a function of time (t) and distance from sample (z). The recovery timescale of Φ is observed to be picoseconds, and the length scale is determined by the spot size of the pump pulse ($\sim$100 μm). Based on the electron's kinetic energy ($\sim$1.5 eV in these studies), the velocity $\mathrm{d}z(t)/\mathrm{d}t$ is about 1 μm/ps. Therefore, the second term in Eq. (3.3) is about 1/100th of the change in Φ. So in Bi2212, the pump-induced change in E_{kf} is dominated by the pump-induced change in E_{ki}, while the second term is 100 times smaller. In GaAs, there is no pump-induced change in E_{ki}, so the measurement is instead dominated by the second term.

This has the interesting effect that in GaAs, the electron energies are shifted even when the pump arrives after the probe. The electrons take hundreds of picoseconds to travel away from the pumped spot, and during this time they are affected by the electric fields induced by the surface photovoltage effect. In theory this could happen in Bi2212 as well, but it would have a magnitude 100 times smaller than the main effect, far too small to observe with our experimental precision.

We can use this framework to explain why there is no pump-induced change in low energy cutoff. This cutoff arises from electrons which have zero kinetic energy immediately after escaping the sample. So the first term in Eq. (3.3) is zero by definition, and the second term is too small to observe.

3.3.4 Asymmetry of density of states

In the previous section, we discussed how $\Delta\mu_{\mathrm{vac}}$ and $\Delta\varepsilon$ could change together, but not how they could change relative to each other. Here we discuss a mechanism that produces a pump-induced change in $\Delta\mu_{\mathrm{vac}}$ but not $\Delta\varepsilon$. For purposes of this discussion, we define $\Delta\mu_\varepsilon$ to be $\Delta\mu_{\mathrm{vac}} - \Delta\varepsilon$.

The basic idea is that the density of states $(D(E))$ in the valence band is asymmetric, which is to say that it is different below the chemical potential compared to above. In an asymmetrical density of states, the chemical potential must change with temperature in order to conserve charge. The chemical potential obeys the equation

$$N = \int_{-\infty}^{\infty} D(E)f(E - \mu_\varepsilon, T_e)\mathrm{d}E, \tag{3.4}$$

where $f(E, T_e)$ is the Fermi-Dirac distribution function at electronic temperature T_e and N is the density of electrons. Equation (3.4) implicitly defines a function $\Delta\mu_\varepsilon(T_e)$, which can be calculated numerically. This has been done before in studies of Bi_2Se_3.[94]

A rough approximation may be derived, which may be helpful to informing our intuition. The chemical potential follows

$$\Delta\mu_\varepsilon \propto -w^2 \frac{D'(E)}{D(E)}\bigg|_{E\sim E_F}, \tag{3.5}$$

where w is the width of the electronic distribution function (typically proportional to temperature), and $D'(E)$ is its first derivative of the density of states evaluated near the Fermi energy E_F.[106] The order of magnitude of $\Delta\mu_\varepsilon$ can also be estimated from Eq. (3.5), substituting $k_B T_c$ for w. For optimally doped Bi2212, this is about 0.5 meV.

Note that Eq (3.5) assumes that the density of states does not change upon pumping. In fact, the density of states does change in the presence of superconductivity. In Section 3.4.2 we will discuss how to modify the picture to account for superconductivity. This will ultimately lead to the observed change in sign of $\Delta\mu_\varepsilon$ across T_c.

3.3.5 Pump-induced mirror charge effect

In Section 3.2.2, we showed that there is an effect on the chemical potential which depends on the product of pump fluence and probe fluence. We can only offer one possible mechanism to explain this effect, which is illustrated in Figure 3.9.

In equilibrium ARPES, when many electrons are ejected together, they gain energy from their repulsion to each other, and this is known as the space charge effect. They also lose energy because of their attraction to each other's mirror charges, and this is known as the mirror charge effect. Both effects depend on the probe fluence, and are usually considered together.[102,103] Pumping the sample cannot change the space charge effect, but it can change the dielectric properties of the material, which may change the mirror charge. As illustrated
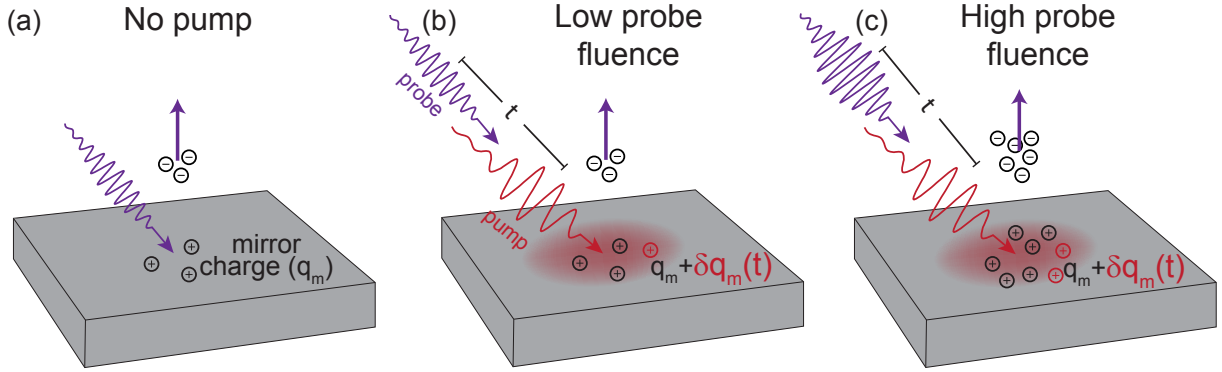
Figure 3.9. The pump-induced mirror charge effect. (a) Without any pumping, electrons are affected by interactions with each other (space charge effect) and interactions with their mirror charges (mirror charge effect). (b) Pumping changes the dielectric properties of the material, causing the mirror charge to change by δq_m. (c) At high probe fluence, δq_m is larger, because it is proportional to the original mirror charge, which is proportional to probe fluence.

in Figure 3.9(b), there is additional mirror charge $\delta q_m(t)$, which is proportional to the original mirror charge q_m. When the probe fluence is higher (see panel (c)), q_m is larger, and therefore $\delta q_m(t)$ is larger too. Thus there is a shift in electron energy which depends on the product of the pump and probe fluences.

In Figure 3.6, we noted that this effect only occurred in the superconducting state. This makes sense because laser pumping suppresses superconductivity, which is likely to have a large effect on the dielectric properties of the material. Unfortunately, the magnitude of the pump-induced mirror charge will depend in a complicated way on the dielectric properties. In this study we do not investigate the details further.

3.3.6 A thermodynamic constraint

Our next consideration is not a mechanism for the change in chemical potential, but a constraint that requires it to change. In the context of studies measuring $\Delta\mu_{\text{vac}}$ in cuprates with the Kelvin probe technique[88,89,90], an expression was derived for the change in chemical potential across the superconducting transition.[91] That expression was

$$\frac{\frac{\mathrm{d}}{\mathrm{d}T}(\mu_n - \mu_\psi)}{c_n - c_\psi}\bigg|_{T=T_c} = \frac{\mathrm{d}lnT_c}{\mathrm{d}n}, \tag{3.6}$$

where T is temperature, c is the specific heat, and n is the particle density. The subscripts ψ and n indicate properties of the superconducting and normal states, respectively.

Although Eq. (3.6) does not fully describe $\Delta\mu_{\text{vac}}$ or provide an exact mechanism, it predicts that $\Delta\mu_{\text{vac}}(T)$ changes in slope across the superconducting transition temperature.

In an overdoped sample, T_c decreases with n, and therefore the slope in $\Delta\mu_{\text{vac}}(T)$ will decrease across T_c. In an underdoped sample, T_c increases with n, and therefore the slope in $\Delta\mu_{\text{vac}}(T)$ will increase across T_c. In an optimally doped sample, T_c doesn't change with n, and therefore the slope in $\Delta\mu_{\text{vac}}(T)$ won't change significantly across T_c.

3.3.7   Quasiparticle vs pair chemical potential

So far, in our discussion of the chemical potential, we've implicitly been speaking of the quasiparticle chemical potential. In superconductors, there is also a second chemical potential, that of the Cooper pairs. When the sample is out of equilibrium, the two chemical potentials are not necessarily equal. This was demonstrated in a study on Sn.[107,108] A current was passed through Sn, with a quasiparticle junction on one side and a Josephson junction on the other. Because the current required a steady flow of charge between the quasiparticles and the Cooper pairs, it induced a difference in their chemical potentials. The chemical potential difference implies a relaxation timescale, which was found to be about 200 ps in the case of Sn.

This is relevant because the superconducting gap is centered at the pair chemical potential. So in our experiments, as we shift the quasiparticle chemical potential, there's a question of whether the superconducting gap shifts along with it in the timescale of the measurement. We will test both possibilities in Section 3.4.2. For now, we make a rough estimate. According to Ref. 108, the relaxation timescale of the difference between the chemical potentials is proportional to $(T_\theta/T_c)^3$, where T_θ is the Debye temperature. Assuming that this dependence still applies, and using[109] $T_\theta = 300$ K and $T_c = 90$ K, we find that the relaxation time is about 2000 times faster in Bi2212 than it is in Sn. So our initial expectation is that the pair chemical potential in Bi2212 immediately equilibrates with the quasiparticle chemical potential, at least within our experimental time resolution of 300 fs.

3.4   Interpretation of results

So far, we have discussed several mechanisms which work in tandem to produce our observed change in chemical potential. The dependence of chemical potential on the probe fluence has been explained as a result of a pump-induced mirror charge effect. The changes in $\Delta\mu_{\text{vac}}$ and $\Delta\varepsilon$ appear to be the result of the combination of two mechanisms. The first mechanism is the change in the surface potential barrier, which causes an equal shift in both $\Delta\mu_{\text{vac}}$ and $\Delta\varepsilon$ (but which does not cause any shift in the low energy cutoff). The second mechanism is the asymmetric density of states, which causes a shift in $\Delta\mu_{\text{vac}}$ only. To separate out the effect of the asymmetric density of states, we calculate $\Delta\mu_\varepsilon = \Delta\mu_{\text{vac}} - \Delta\varepsilon$.

We do not make specific predictions about the magnitude of the change in surface potential barrier, but Eq. (3.6) describes a constraint on $\Delta\mu_{\text{vac}}$ as a function of temperature. We test this constraint in Section 3.4.1. In Section 3.4.2, we discuss the density of states in a
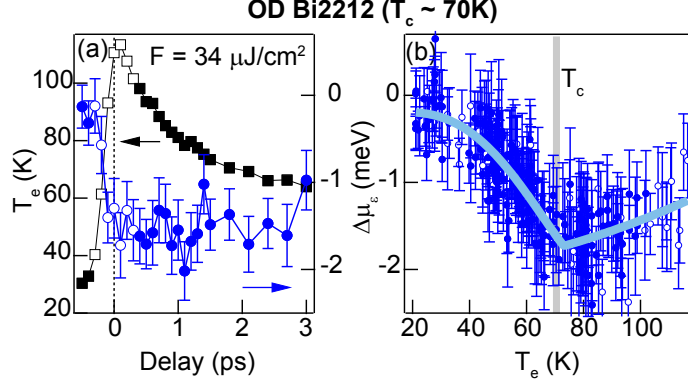
Figure 3.10. Producing chemical potential-temperature curves. (a) $\Delta\mu_\varepsilon$ and T_e as a function of delay time t after pumping an overdoped Bi2212 sample with a 34 μJ/cm^2 pulse. (b) $\Delta\mu_\varepsilon$ is shown as a function of T_e, eliminating t as a variable. Data points are collected from delay times up to 10 ps, pump fluences between 3 and 34 μJ/cm^2, and initial temperatures between 25 and 80 K. Empty circles denote the data collected between a –0.3 and 0.3 ps delay. Error bars are calculated from the variance between measurement cycles.

superconductor. In Section 3.4.3, we discuss the pseudogap state, and draw new conclusions about the structure of the pseudogap.

3.4.1 Chemical potential-temperature curves

The surface barrier potential and the asymmetric density of states mechanisms both predict that the chemical potential varies as a function of temperature. In our studies, the sample is out of equilibrium and does not have a true temperature. However, we do measure an electronic temperature T_e, so we seek to find the chemical potential as a function of T_e.

Figure 3.10(a) shows $\Delta\mu_\varepsilon$ and T_e as functions of delay time t after pumping a sample at 30 K with a 34 μJ/cm^2 pulse. In panel (b) we plot $\Delta\mu_\varepsilon$ directly as a function of T_e. Data were collected for t up to 10 ps, combining five different experiments with pump fluences ranging from 3 to 34 μJ/cm^2 and initial temperatures ranging from 25 to 80 K. Each experiment was shifted by a constant energy to account for the initial chemical potential at different initial temperatures. These data demonstrate the nontrivial fact that the function $\Delta\mu_\varepsilon(T_e)$ exists independently of changes in experimental conditions. In particular, we show that the data taken between -0.3 and 0.3 ps (open circles) fall along the same curve, reinforcing the notion $\Delta\mu_\varepsilon(T_e)$ is an equilibrium property of the system, even though we have measured it on ultrafast timescales.

We can repeat the same procedure for $\Delta\mu_{\text{vac}}$ and $\Delta\epsilon$ separately. Figure 3.11 shows both $\Delta\mu_{\text{vac}}$ and $\Delta\epsilon$ as functions of electronic temperature (T_e) for four differently doped samples of Bi2212. Again, the data are collected over multiple measurements with fluences ranging from 3 to 34 μJ/cm^2, different delay times up to 10 ps, and various initial temperatures.
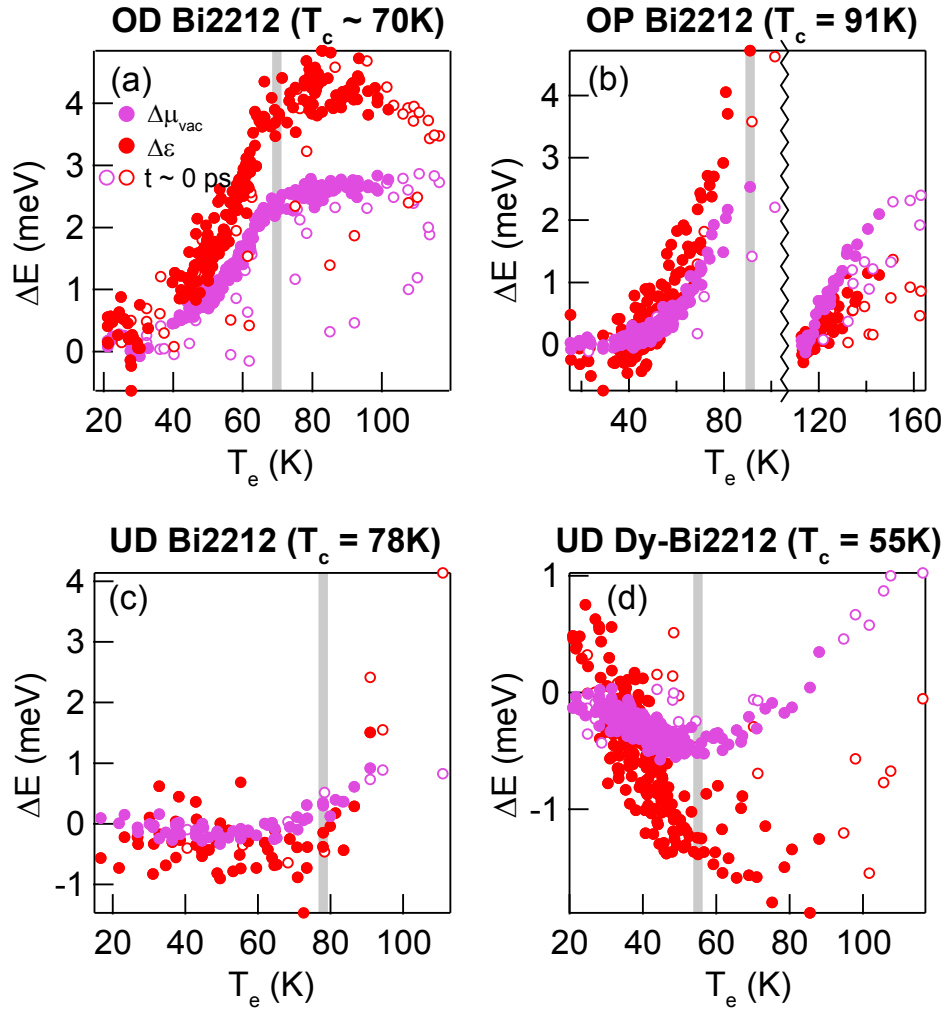
Figure 3.11. $\Delta\mu_{vac}$ and $\Delta\epsilon$ as a function of electronic temperature, combined over many experiments on OD Bi2212 (a), OP Bi2212 (b), slightly UD Bi2212 (c), and very UD Dy-Bi2212 (d). Open circles show measurements taken at delay times between -0.3 and 0.3 ps. Gray bars indicate the superconducting transition temperature T_c. The dividing line in (c) indicates that low and high temperature data could not be compared.

Although the data are collected over a large variety of conditions, nearly all data fall along a single function of electronic temperature, with some notable exceptions: measurements taken between -0.3 and 0.3 ps after pumping (open circles) are often outliers. These outliers indicate that $\Delta\mu_{\mathrm{vac}}$ and $\Delta\epsilon$ lag behind the electronic temperature on a timescale of about 0.3 ps. This is in contrast to $\Delta\mu_\varepsilon$, which did not have any apparent lag behind the electronic temperature within our experimental resolution (see Fig. 3.10).

The differences in lag time are unsurprising given our understanding of the distinct origins of $\Delta\mu_\varepsilon$ and $\Delta\mu_{\mathrm{vac}}$. $\Delta\mu_\varepsilon$ is understood as the effect of a broadening electronic distribution function in an asymmetrical density of states. $\Delta\mu_{\mathrm{vac}}$ is understood as a change in the surface potential barrier. There is little relation between these two mechanisms, so it is not surprising that one is independent of delay time, while the other lags on a 0.3 ps timescale.

Examining Fig. 3.11, we can verify consistency with the thermodynamic constraint in Eq. (3.6). Verifying the equation, we observe that in the overdoped sample (Fig. 3.11(a)), the slope in $\Delta\mu_{\mathrm{vac}}(T_e)$ decreases across T_c. In the underdoped samples (Figs. 3.11(c)–3.11(d)), the slope in $\Delta\mu_{\mathrm{vac}}(T_e)$ increases across T_c. In the optimally doped sample (Fig. 3.11(b)), the slope in $\Delta\mu_{\mathrm{vac}}(T_e)$ doesn't change significantly across T_c.

3.4.2   Density of states in a superconductor

In Figure 3.4 we saw that $\Delta\mu_\varepsilon$ is negative below T_c and positive above T_c. This was shown again in a different way in Fig. 3.10, where the slope of $\Delta\mu_\varepsilon(T_e)$ changes from negative to positive across T_c. The change of sign can be fully explained as a consequence of the density of states in a superconductor. The basic explanation is that the quasiparticle distribution function $f(E, T_e)$ is broadened by the superconducting gap. This broadening causes the width w in Eq. (3.5) to actually be larger when the gap is open below T_c than when the gap is closed at T_c. The result is that the slope in $\Delta\mu_\varepsilon(T_e)$ changes sign across T_c.

Now we explain the argument in greater detail. We begin with the normal density of states in optimally doped Bi2212, which can be approximated with a simple phenomenological tight-binding model (see Fig. 3.12(a)).[110] Because of the saddle point in the valence band, there is a Van Hove singularity in the density of states just below the chemical potential, which causes an asymmetric density of states. The negative slope in $D(E)$ causes a positive slope of $\Delta\mu_\varepsilon(T_e)$ in the normal state.

In the superconducting state, the pairing interaction causes the electron and hole quasiparticles to mix. We distinguish between ε, the quasiparticle energy before the pairing interaction is turned on, and E, the energy afterwards, each measured relative to μ_{pair}, the pair chemical potential. Figure 3.12(b) shows the Bogoliubov quasiparticle dispersion described in Section 1.1.3, which has two branches with energies $E_\pm(\varepsilon) = \pm\sqrt{\varepsilon^2 + \Delta^2}$ and
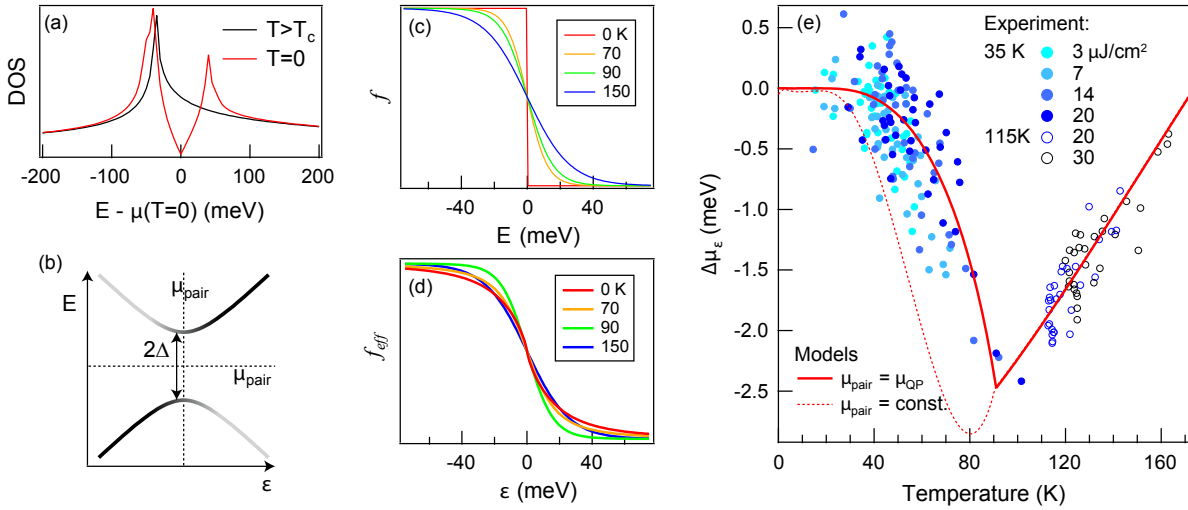
Figure 3.12. The effect of superconductivity on the chemical potential. (a) The density of states of optimally doped Bi2212 calculated with a tight-binding model, in both the normal state, and superconducting state at T=0. (b) An illustration of the relationship between ε, the quasiparticle energies before the pairing interaction is turned on, and E, the energies afterwards. (c) The distribution function as a function of E. (d) The effective distribution function as a function of ε. (e) A comparison of the experimental $\Delta\mu_\varepsilon$ to its calculated value, considering the case where the pair chemical potential is equal to the quasiparticle chemical potential and the case where it is held constant.

spectral weights $w_\pm(\varepsilon) = \frac{1}{2}(1 + \frac{\varepsilon}{E_\pm})$. The resulting density of states is

$$D(E, \Delta) = \begin{cases} \frac{E}{\varepsilon}\Big(w_+(-\varepsilon)D(-\varepsilon) + w_+(\varepsilon)D(\varepsilon)\Big) & \text{for } E > \Delta \\ \frac{E}{\varepsilon}\Big(w_-(-\varepsilon)D(-\varepsilon) + w_-(\varepsilon)D(\varepsilon)\Big) & \text{for } E < -\Delta \\ 0 & \text{for } |E| < \Delta \end{cases} \qquad (3.7)$$

where $\varepsilon = \sqrt{E^2 - \Delta^2}$.

In the case of Bi2212, Δ varies with momentum because of the d-wave gap symmetry. However, a first approximation can be made by taking the total density of states, applying a constant Δ, and summing the results over a range of values of Δ. This approximation is shown in Figure 3.12(a). A more accurate calculation could be made by taking the momentum-dependent density of states, and applying the appropriate value of Δ at each momentum.

We now consider the special case where the pair chemical potential and quasiparticle chemical potentials are equal. Using Equation (3.7), it is possible to change variables in the integral of Eq. (3.4) from E to ε. The new equation is

$$N = \int_{-\infty}^{\infty} D(\varepsilon) f_{eff}(\varepsilon - \mu_\varepsilon, T_e, \Delta) d\varepsilon, \qquad (3.8)$$

where f_{eff} is the effective distribution function with respect to ε. In an s-wave superconductor, f_{eff} is given exactly by

$$f_{eff}(\varepsilon, T_e, \Delta) = \frac{1}{2}\Big(1 - \frac{\varepsilon}{E}\Big) + \frac{\varepsilon}{E}f\Big(E, T_e\Big). \qquad (3.9)$$

This is equivalent to an equation that had previously been derived as an attempt to explain Kelvin probe measurements.[111] The first term of Eq. (3.9) is the contribution from the energy gap, while the second term is the contribution from temperature. In a d-wave superconductor, we can approximate f_{eff} by integrating Eq. (3.9) over a range of gap sizes. A more accurate calculation could be made by applying Eq. (3.9) separately at each momentum, applying the value of Δ at that momentum; however, here an approximation suffices.

The functions $f(E, T)$ and $f_{eff}(\varepsilon, T, \Delta)$ are shown in Figs. 3.12(c) and 3.12(d), using a d-wave gap that follows a BCS temperature dependence and has a maximum size of 39 meV.[14] To understand what is happening, we refer to the width of $f(E, T)$ as w, and the width of $f_{eff}(\varepsilon, T, \Delta)$ as w_{eff}. At zero temperature, w is zero, but w_{eff} has a nonzero value proportional to the size of the superconducting gap. The enhancement of w_{eff} does not represent thermal excitations but rather the Bogoliubov mixing of electronlike and holelike excitations. Pumping is known to suppress the superconducting gap;[73,81] thus, as we approach $T_e = T_c$ the value of w_{eff} may actually decrease with the temperature, if $\Delta_{\text{SC}} \gg k_B T_c$. This is seen in Fig. 3.12(d), where w_{eff} actually gets smaller as T increases to $T_c = 91K$. Above T_c, w_{eff} increases with temperature.

Equation 3.5 predicts that $\Delta\mu_\varepsilon(T_e)$ follows the same trend as the width of w_{eff}. Figure 3.12(e) shows predictions of $\Delta\mu_\varepsilon(T_e)$ alongside the observations. The model has no free parameters, but matches the data quite well.
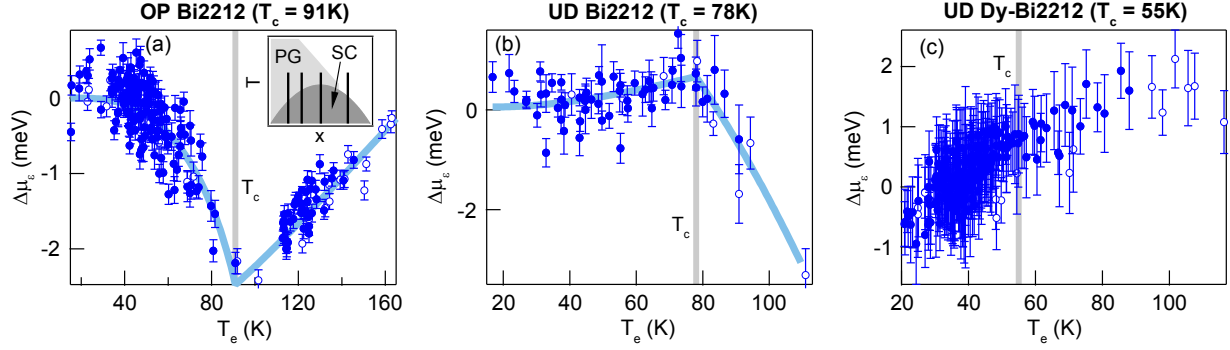
41

Figure 3.13. The function $\Delta\mu_\varepsilon(T_e)$ is plotted for OP Bi2212 with $T_c = 91$ K (a), a slightly UD Bi2212 with $T_c = 78$ K (b), and a very UD Dy-Bi2212 with $T_c = 55$ K (c). Data are collected over many delay times, pump fluences, and initial temperatures. The inset of (a) shows the cuprate phase diagram, including the superconducting (SC) and pseudogap (PG) phases, with black lines indicating the three samples, as well as the sample in Fig. 3.10. Empty circles denote the data taken between a –0.3 and 0.3 ps delay, and gray bars indicate T_c. (a) uses the same data from Fig. 3.10.

We also consider an alternate model, based on the idea that the pair chemical potential and quasiparticle chemical potential take a very long time to equilibrate. Rather than letting the superconducting gap shift with the chemical potential, we hold the center of the gap at a constant energy. The result of a numerical calculation is shown in Fig. 3.12(e) with the dashed red line. The alternate model fails to match our observations, and this corroborates our initial expectation in Section 3.3.7 that the quasiparticle and pair chemical potentials equilibriate faster than the timescale of our measurement.

3.4.3 Density of states in the pseudogap

The superconducting gap had an interesting effect on the chemical potential, but the structure of the superconducting gap is already largely understood. By contrast, the structure of the pseudogap is not understood. In particular, the superconducting gap is understood to have particle-hole symmetry in the sense of being centered at the chemical potential. It is not known whether the pseudogap has particle-hole symmetry or not.

As discussed in Section 1.2.2, whether the pseudogap has particle-hole symmetry is at the heart of a dispute about its nature. Some studies support a particle-hole symmetric pseudogap,[112,113,114,115,116,29,30] representing fluctuating superconducting order.[32] Other studies claim to demonstrate the particle-hole asymmetry of the pseudogap,[39,40,41,42] which could be consistent with various theories, including d-density wave order theory,[33] the Yang-Rice-Zhang (YRZ) model of a doped resonant valence bond state,[36,37,38] algebraic charge liquid theory,[34] Amperean pairing theory,[35] or an alternate model of fluctuating superconducting order.[117] Several of the aforementioned theories also purport to explain the nature of superconductivity.

Since we have demonstrated that the $\Delta\mu_\varepsilon(T_e)$ curve in Bi2212 is determined by the asymmetry in the density of states, it would be fruitful to measure the curve in differently doped samples, since the pseudogap is known to get larger with underdoping.[118,14] Figure 3.13 shows the results on OP Bi2212 ($T_c = 91$ K) slightly UD Bi2212 ($T_c = 78$ K), and very UD Dy-Bi2212 ($Bi_2Sr_2Ca_{0.6}Dy_{0.4}Cu_2O_{8+\delta}$, $T_c = 55$ K). The trends in $\Delta\mu_\varepsilon(T_e)$ are qualitatively distinct in each case. This suggests that the relevant property of the material is not just the size of the pseudogap, but its relative size compared to another energy scale. In this picture, the three distinct regimes arise when the pseudogap is comparatively large, small, or just the right size.

In Fig. 3.12, we had already explained how the $\Delta\mu_\varepsilon(T_e)$ curve in OP Bi2212 is the result of the density of states in the superconducting state, and a negative $D'(E)$. The $\Delta\mu_\varepsilon(T_e)$ curve in OD Bi2212 (see Fig. 3.10) can also be explained in the same manner. Both of these samples are in the small pseudogap regime.

The slightly UD Bi2212 sample (Fig. 3.13(b)) is in the midsized pseudogap regime. Here, $\Delta\mu_\varepsilon(T_e)$ follows an inverted trend, increasing with temperature up to T_c, and decreasing with temperature beyond that. Looking at Eq. (3.5), this suggests that $D'(E)$ is positive, in contrast to the OP and OD samples.

Finally, we consider the heavily UD Dy-Bi2212 (Fig. 3.13(c)), which is in the large pseudogap regime. Here, $\Delta\mu_\varepsilon(T_e)$ increases with temperature both below and above T_c. The lack of change across T_c suggests that the effect of the superconducting gap is washed out by a sufficiently large pseudogap. The positive slope in $\Delta\mu_\varepsilon(T_e)$ suggests that $D'(E)$ is negative again in this sample.

To summarize, we have deduced that $D'(E)$ is negative near the chemical potential in samples that either have a very small or very large pseudogap. And when the pseudogap is large, it washes out the effect of the superconducting gap. When the pseudogap is somewhere in the midsized range, $D'(E)$ changes sign to be positive. If the pseudogap is particle-hole symmetric, then it has the same effect on the density of states both above and below the chemical potential, and therefore cannot change the sign of $D'(E)$. Thus, we conclude that the pseudogap cannot be particle-hole symmetric.

Although the sign change in $D'(E)$ points to a particle-hole asymmetric gap, not every particle-hole asymmetric model would necessarily produce the behavior observed here. In Fig. 3.14, we compare our experimental findings to a relatively simple particle-hole asymmetric pseudogap model, the YRZ model, which is based on a doped resonant valence bond state.[36,37,38] Figures 3.14(a) and 3.14(b) show the pseudogap in two underdoped samples as a function of the Fermi surface angle (φ). Near the node ($\varphi \sim 45°$), the pseudogap is entirely above the Fermi energy, resulting in the well-known Fermi arc.[17,18] Near the antinodes ($\varphi = 0$ and 90°), the pseudogap is centered below the Fermi energy. For the slightly underdoped sample (panel (a)), the antinodal upper pseudogap edge lies just above the Fermi energy. But for the very underdoped sample (panel (b)), the pseudogap is larger, such that the antinodal upper pseudogap edge is further from the Fermi energy.

Figures 3.14(c) and 3.14(d) show density of states calculations for each pseudogap size. There are clear anomalies in the density of states at the upper and lower antinodal gap
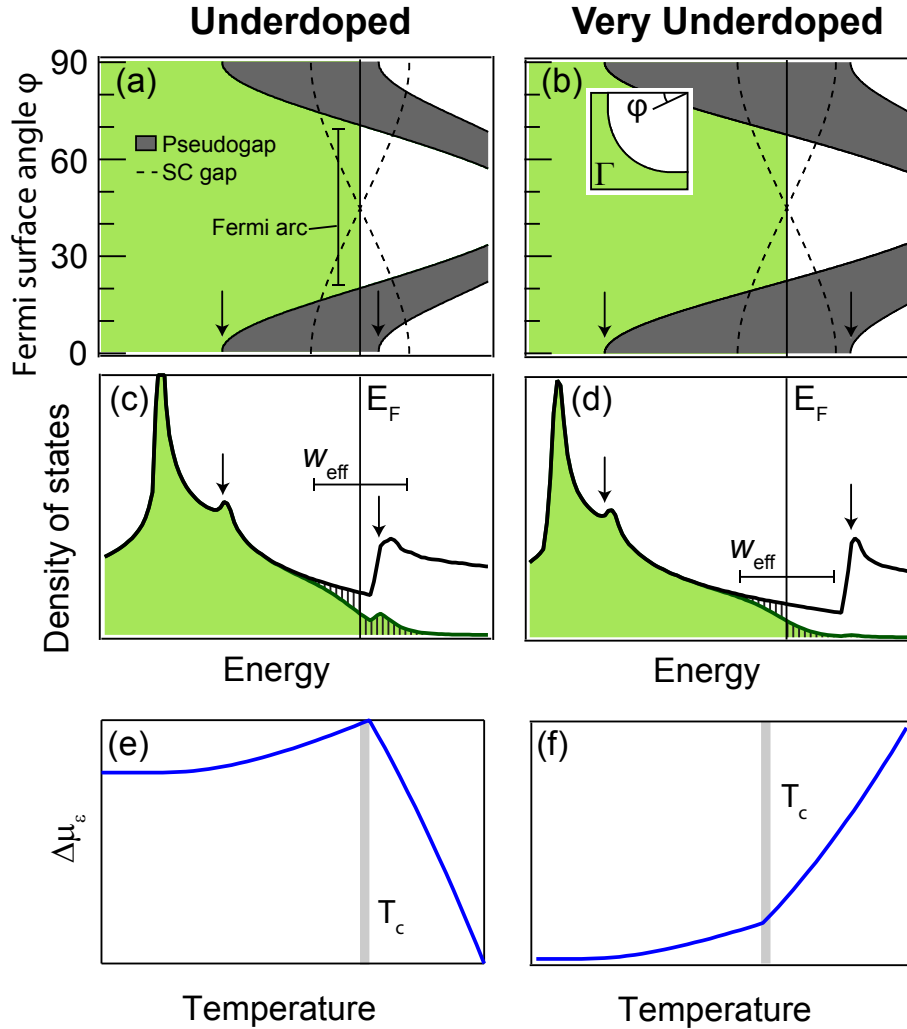
Figure 3.14. The density of states in a pseudogap, using the YRZ model. Shown are the underdoped (a,c,e) and very underdoped (b,d,f) cases of Bi2212. (a,b) Diagrams of the pseudogap, parametrized by the Fermi surface angle φ shown in the quarter Brillouin zone in the inset of (b). (c,d) The calculated density of states, with the green shaded region indicating occupied states. The striped area below the Fermi energy must be equal to the striped area above the Fermi energy in order to conserve charge. Arrows indicate the edges of the antinodal pseudogap. (e,f) Qualitative predictions of the function $\Delta\mu_\varepsilon(T_e)$. Gray bars indicate T_c.

edges (black arrows). Such anomalies had also been shown in previous calculations.[38] For the slightly underdoped sample (Fig. 3.14(c)), the anomaly just above E_F causes $D'(E)$ to have a positive sign near E_F, which leads to an inversion of $\Delta\mu_\varepsilon(T_e)$ (Fig. 3.14(e)). This is similar to the inversion seen in UD Bi2212 (Fig. 3.13(b)).

However, for the very underdoped sample (Fig. 3.14(d)), the anomaly is too far away from E_F to impact $D'(E)$ near E_F. Furthermore, the large antinodal pseudogap restricts the impact of the superconducting gap to the Fermi arc, and at these momenta the superconducting gap is smaller (see Fig. 3.14(b)). This reduces the effect of superconductivity on the width, resulting in a relatively weak feature at T_c in $\Delta\mu_\varepsilon(T_e)$ (Fig. 3.14(f)). This is similar to our results on underdoped Dy-Bi2212 (Fig. 3.13(c)).

3.5   Conclusions

In these studies, we have catalogued a variety of mechanisms that would lead to a pump-induced change in chemical potential. We have argued that the main effects are a pump-induced mirror charge effect, a change in the surface potential barrier, and the asymmetric density of states. This last mechanism has been most interesting, because it can be used as a window to study the density of states in the presence of superconductivity and the pseudogap.

The main result is that the slope in density of states near the Fermi energy changes sign in Bi2212 in the presence of a pseudogap. This implies that the pseudogap has particle-hole asymmetry, unlike the symmetry of the superconducting gap. The sign change occurs both above and below T_c, supporting previous work showing that the pseudogap coexists with superconductivity.[23,24,25,26,14,27] Using calculations of the YRZ model,[36,37,38] we have shown that the results on a UD Bi2212 sample are well described by an anomaly in the density of states just above the Fermi energy, created by the antinodal upper pseudogap edge. Our results on very underdoped Dy-Bi2212 are described by an anomaly that appears further away from the Fermi energy. However, this is not a demonstration that the YRZ model is correct. The results may also be consistent with other particle-hole asymmetric pseudogap models, such as the Amperean pairing model.[35] This must be verified by calculations of the density of states within each theory.

We note that our conclusion of particle-hole asymmetry relies on several assumptions. First, we used Eq. (3.5) rather than the more general Eq. (3.4). There is a remote possibility that the pseudogapped density of states changes with temperature in precisely the right way to give only the appearance of an asymmetric pseudogap. Second, the results we see in UD Bi2212 could also be caused by the charge density wave state[119] or the d-symmetry form factor density wave state,[120] and it is unknown whether these states are related to the pseudogap. Third, while we have shown qualitative consistency with the YRZ model, further work is needed to show quantitative consistency with this or other pseudogap models.

An exciting implication of our results is that the upper edge of the antinodal pseudogap can be directly accessed by ARPES because it falls within the effective quasiparticle

distribution width w. Note that w is dominated by Bogoliubov mixing rather than thermal excitations, and so, we predict that excitations above the Fermi energy will be reflected below the Fermi energy, seen as a small peak or shoulder in the ARPES spectra.[121] This may have already been observed.[41] Study of this feature may provide more detailed momentum-dependent information on the pseudogap.

Chapter 4

Stimulated emission of Cooper pairs

The concept of stimulated emission of bosons has played an important role in modern science and technology, and constitutes the working principle for lasers. In a stimulated emission process, an incoming photon enhances the probability that an excited atomic state will transition to a lower energy state, and generate a second photon of the same energy. It is thought that a stimulated emission process also operates in superconductors, stimulating the recombination of quasiparticles into Cooper pairs.

This chapter describes a study[122] where we claim to have observed the effects of stimulated recombination in the cuprate superconductor Bi2212. As with the previous chapter, the key was to investigate an aspect of TARPES experimental results that is usually overlooked. While many studies have generated non-equilibrium quasiparticles (NEQPs) in both conventional and high-temperature superconductors, so far most have focused on the decay of the NEQP population. Here we instead look at the buildup of the NEQP population in Bi2212. We find that the buildup is slower in the superconducting state inside the Fermi arc region at low fluences. We propose a mechanism where stimulated recombination of NEQPs counteracts the initial buildup of NEQPs, slowing it down. If this proposal is correct, it signals an important momentum space dichotomy in the formation of Cooper pairs inside and outside the Fermi arc region.

4.1   Introduction

Numerous studies have used ultrafast infrared pulses to break Cooper pairs and generate NEQPs in conventional and high-temperature superconductors.[123,124,125,72,78] So far, most pump-probe spectroscopic studies on superconductors have focused on the decay of the NEQPs through recombination into Cooper pairs, which occurs on picosecond timescales.[126,79,101,127,72] Such phenomena are usually understood within the phenomeno-

logical Rothwarf-Taylor (RT) model, whose basic ingredient is simple bimolecular recombination.[128,123,72]

One way to go beyond the RT model would be to include the effects of stimulated emission into the superconducting condensate. Because Cooper pairs obey boson-like statistics, they can be considered analogous to photons in a laser medium. The presence of a photon enhances the probability that an excited atomic state within the medium will transition to lower energy state, and emit a photon in the exact same state as the first photon. Likewise, the presence of a superconducting condensate enhances the probability that excited Cooper pairs will return to the Condensate instead of entering any other state. This process can be thought of as the origin of the zero resistance current in a superconductor. While stimulated emission likely has a negligible effect during the relatively slow decay of the NEQP population on picosecond timescales, it may play a greater role in the faster buildup dynamics of the NEQP population, which occurs on femtosecond timescales.

Here we report a systematic TARPES study of the temperature, momentum, doping, and density dependence of the initial buildup of NEQPs in high temperature superconductor Bi2212. In the superconducting state, and at low pump fluence, it takes ~ 0.9 ps for the NEQP population to reach the maximum. In contrast, in the normal state, or when the pump fluence is sufficiently strong to deplete the entire superconducting condensate, the maximum in the NEQP population is reached immediately (within our time resolution of 300 fs) after the arrival of the pump pulse. The NEQP population residing outside the Fermi arc also builds up almost instantly. Along the Fermi arc, the NEQP buildup time shortens as the energy gap increases. We propose that these findings provide evidence of stimulated recombination of quasiparticles into the superconducting condensate.

4.2 Buildup of non-equilibrium states

Figure 4.1 shows the buildup of the nodal NEQP population for an underdoped Bi2212 superconductor ($T_c = 78$ K) above and below the superconducting transition temperature. Figure 4.1(a) shows the equilibrium photoemission intensity map (before the arrival of the pump pulse) in the superconducting state and the pump-induced change of the same map for different delay times (with t=0 representing the arrival time of the pump pulse). Here the pump fluence (2.4 μJ/cm^2) is far below the critical fluence (15 μJ/cm^2) needed to fully deplete the superconducting condensate (as discussed in section 2.3).[78] We observe a clear decrease in the photoemission intensity below the Fermi level, and an increase above the Fermi level, signifying the excitation of NEQPs. However, the change in intensity is greater at $t = 0.9$ ps than at $t = 0$, indicating that the NEQP population requires a finite time to build up. This can also be seen in the integrated intensity as a function of energy, shown in the left panel of Fig. 4.1(b).

Figure 4.1(c) shows the integrated change in the intensity above the Fermi level, defined
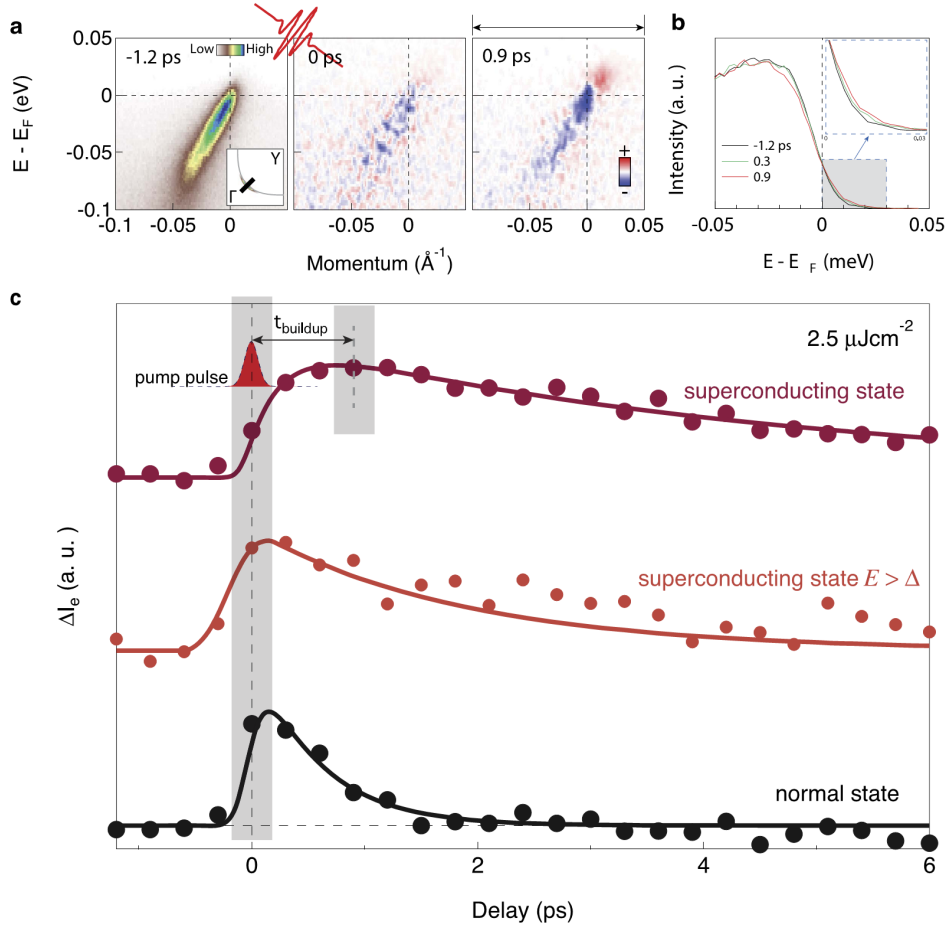
Figure 4.1. Buildup time of nodal non-equilibrium quasiparticles. Measurements were taken along a nodal cut in an underdoped Bi2212 ($T_c = 78$K) sample, using a pump pulse with fluence 2.4 μJ/cm^2. (a) Equilibrium photoemission intensity at delay time $t = -1.2$ ps as a function of energy and momentum, and pump-induced change of photoemission spectra as a function of energy and momentum at delay time 0 and 0.9 ps. (b) The photoemission intensity obtained by integrating over the momentum window indicated by the arrows in (a), for three different delay times. (c) The spectral gain ΔI_e as a function of delay time. The three curves are obtained by integrating the change of photoemission intensity above the Fermi level at 20 K, above the energy of the maximum superconducting gap at 20 K, and above the Fermi level in the normal state at 90 K, respectively. The width of the pump pulse in the cartoon is determined by frequency-resolved optical gating (FROG).
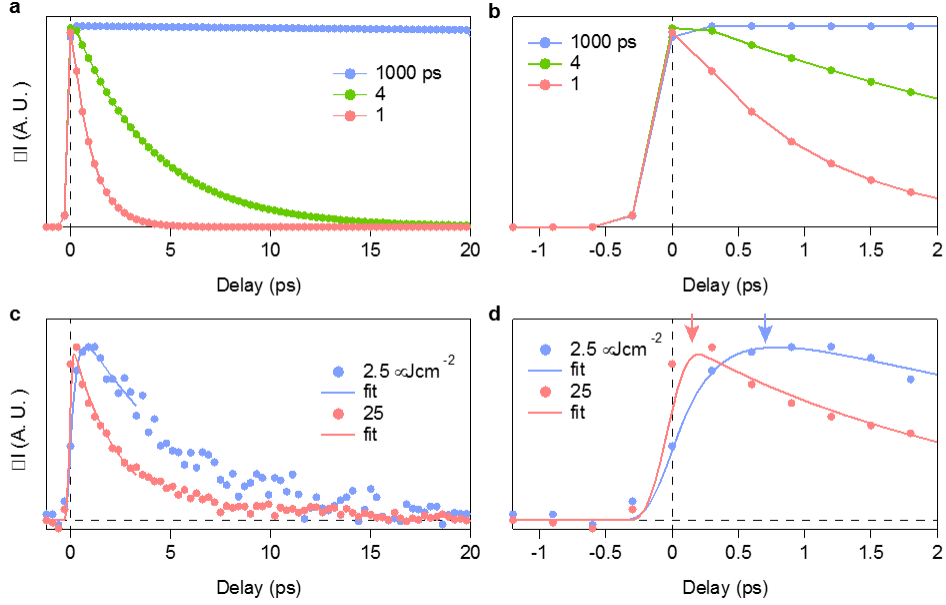
Figure 4.2. Effect of time-resolution on buildup time. (a) Simulated decay curves with zero buildup time, and decay times of 1, 4, and 1000 ps, convolved with a Gaussian resolution function (FWHM = 300 fs). (c) The decay curves at pump fluence 2.5 μJ/cm^2 (below F_c) and 25 μJ/cm^2 (above F_c) for the underdoped (T_c = 78 K) sample. (b,d) The decay curves in (a) and (c), respectively, shown at delay times between -1.2 and 2 ps.

as[72,79,101,127]

$$\Delta I_{\mathrm{e}}(t) = \int_0^E \mathrm{d}\omega \int_{0.1}^{0.1} \mathrm{d}k [I(\omega, k, t) - I(\omega, k, -1.2 \text{ ps})] \tag{4.1}$$

as a function of time for $T = 20$ K $< T_c$ and $T = 90$ K $> T_c$. Consistent with Fig. 4.1(a), the maximum change in intensity occurs at a much later time than $t = 0$. We will define the time at which ΔI_e is near maximum as t_{buildup}, the "buildup" time. Later, we will describe a procedure to extract t_{buildup}. For $t > t_{\mathrm{buildup}}$, the decay rate of the NEQP population above T_c is much faster than that below T_c, consistent with other reports in the literature.[123,126,72] From now on, we focus our attention on $\Delta I_e(t)$ for the usually overlooked $t \leq t_{\mathrm{buildup}}$. Strikingly, in the superconducting state, the maximum intensity change (t_{buildup}) is reached at ~ 1 ps, while in the non-superconducting state, the maximum intensity change is reached instantly. If ΔI_e is integrated only above the maximum superconducting gap (Δ_{max}), no delay in t_{buildup} is observed.

One initial consideration is that the finite t_{buildup} could arise from limitations in our time resolution. But this is immediately ruled out in Fig. 4.2. We create a basic simulation by taking decay curves with decay times of 1, 4, and 1000 ps, and convolve them with a Gaussian time-resolution function with full width half maximum (FWHM) of 300 fs. These curves are compared to two experimental measurements on Bi2212, one with a longer buildup time than the other. While the time resolution broadens the initial buildup of NEQPs, it is clear that the broadening is too small to explain our data.
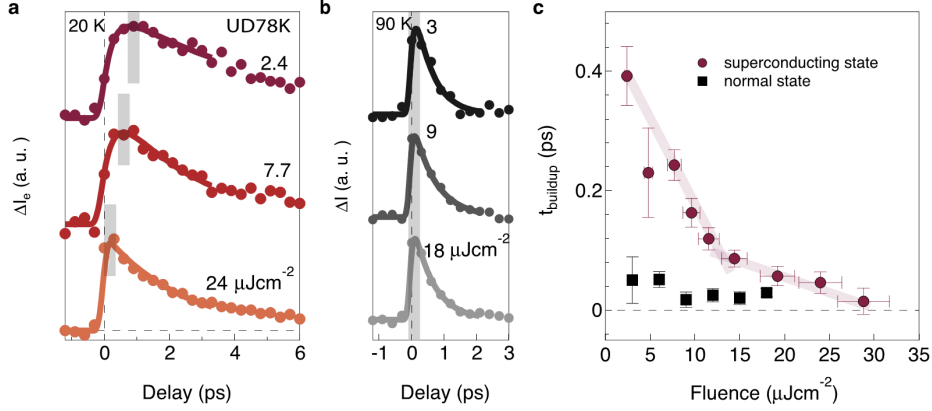
Figure 4.3. The fluence dependence of the buildup time. (a,b) ΔI_{e} as a function of delay time and pump fluences at 20 K and 90 K, respectively, for an underdoped sample ($T_{\mathrm{c}} = 78$ K). The shaded line is a guide to the eyes. (c) The extracted buildup time t_{buildup} as a function of pump fluence in the normal and superconducting states

4.3 Pump fluence dependence

Figure 4.3(a) shows the low temperature ($T < T_c$) $\Delta I_{\mathrm{e}}(t)$ for different pump fluences. Very different buildup behaviors are observed for fluences below and above the critical fluence ($15\ \mu\mathrm{J/cm}^2$). Specifically, at pump fluence equal to $24\ \mu\mathrm{J/cm}^2$, $\Delta I_{\mathrm{e}}(t)$ reaches its maximum instantly within our time resolution. This fast buildup is similar to the normal state data in Fig. 4.3(b). On the other hand, at lower pump fluence, t_{buildup} appears as large as 0.9 ps. In marked contrast with the low temperature data, for $T > T_c$, the buildup of NEQPs does not show a significant delay for any pump fluence studied (see Fig. 4.3(b)).

To precisely define the buildup time t_{buildup}, we fit $\Delta I_{\mathrm{e}}(t)$ with a resolution-convolved function given by

$$\Delta I_{\mathrm{e}}(t) = A(1 - e^{-t/t_{\mathrm{buildup}}})e^{-\gamma t} \otimes Gauss(t, \mathrm{FWHM}) \tag{4.2}$$

where γ is the long-time NEQP population decay rate. The Gaussian accounts for the experimental time resolution, and its FWHM is 300 fs. Equation (4.2) captures the dynamics of the initial buildup of NEQPs quite well (see solid lines in Fig. 4.3(a)). Figure 4.3(c) shows the extracted t_{buildup} as a function of pump fluence. At low temperature, t_{buildup} is ~ 400 fs at the lowest fluence, and decreases as the fluence increases until it saturates at the normal state value of < 100 fs. The saturation occurs at the critical fluence required to deplete the superconducting condensate,[78] but note that the superconducting gap does not close until about 0.6 ps later.[73] The absence of a buildup time above T_c or above the critical fluence suggests a connection between the slow buildup and the presence of the superconducting condensate.

4.4 Momentum dependence

In momentum space, similar delayed buildup is observed in $\Delta I_e(t)$ throughout the Fermi arc region. Figure 4.4(a) shows the momentum-dependent buildup time in an optimally doped sample in response to a weak (2.4 μJ/cm^2) pump. As previously reported,[72] the long-time decay rate (γ) of the NEQP population increases from node to off-node. Inside the Fermi arc region, there is a delay in buildup, which decreases away from the node. In contrast, for a momentum cut outside the Fermi arc region, there is no delay, and t_{buildup} drops to the normal state value of about 100 fs.

We have also compared the buildup time for the NEQP population in samples with different doping level (see overdoped sample in Fig. 4.4(b)), and the same momentum dependence of t_{buildup} is observed: the buildup time is nonzero only on the Fermi arc. For the overdoped sample, all measurements were taken within the Fermi arc region, and hence they all show an apparent delay in the buildup of the NEQP population. However, compared with the optimally- and underdoped samples, the delay is less pronounced (see Fig. 4.4(c)). The momentum dependence of the buildup rate for the NEQP population is shown in Fig. 4.4(d). For each momentum we extract the corresponding gap value. The NEQP is then plotted as a function of gap size. Gap values are extracted using a standard procedure of fitting the symmetrized energy distribution curves at the Fermi momentum to the phenomenological single particle spectral functions.[129] It is clear that there is a distinct mechanism for the buildup time for the states beyond the Fermi arc region.

Note that the difference cannot be attributed to the lack of a gap inside the Fermi arc region, since the Fermi arc itself does not develop until about 0.6 ps after pumping.[73] Interestingly, the buildup time of the NEQP population is identical to that of the photoinduced shift of the superconducting gap at the same momentum (see Fig. 4.4(e)) The similar timescale further suggests that the superconducting condensate is a key ingredient in establishing the buildup time.

4.5 Stimulated emission mechanism

Now we propose an explanation of these observations that takes into account the quantum coherence of the Cooper pair condensate. When the pump pulse photoexcites the material, the input energy is partially stored in the electronic degrees of freedom, and partially in the lattice degrees of freedom. Where there is a superconducting condensate, those NEQPs whose time reversal partner is also excited can quickly recombine into Cooper pairs due to a process of coherent recombination stimulated by the existing condensate. This process serves to reduce the proportion of input energy initially stored in electronic degrees of freedom, hence causing the observed delay in the buildup of the NEQP population. Such a stimulated recombination process is absent when the superconducting condensate is depleted by either the temperature, or by a high fluence pump.

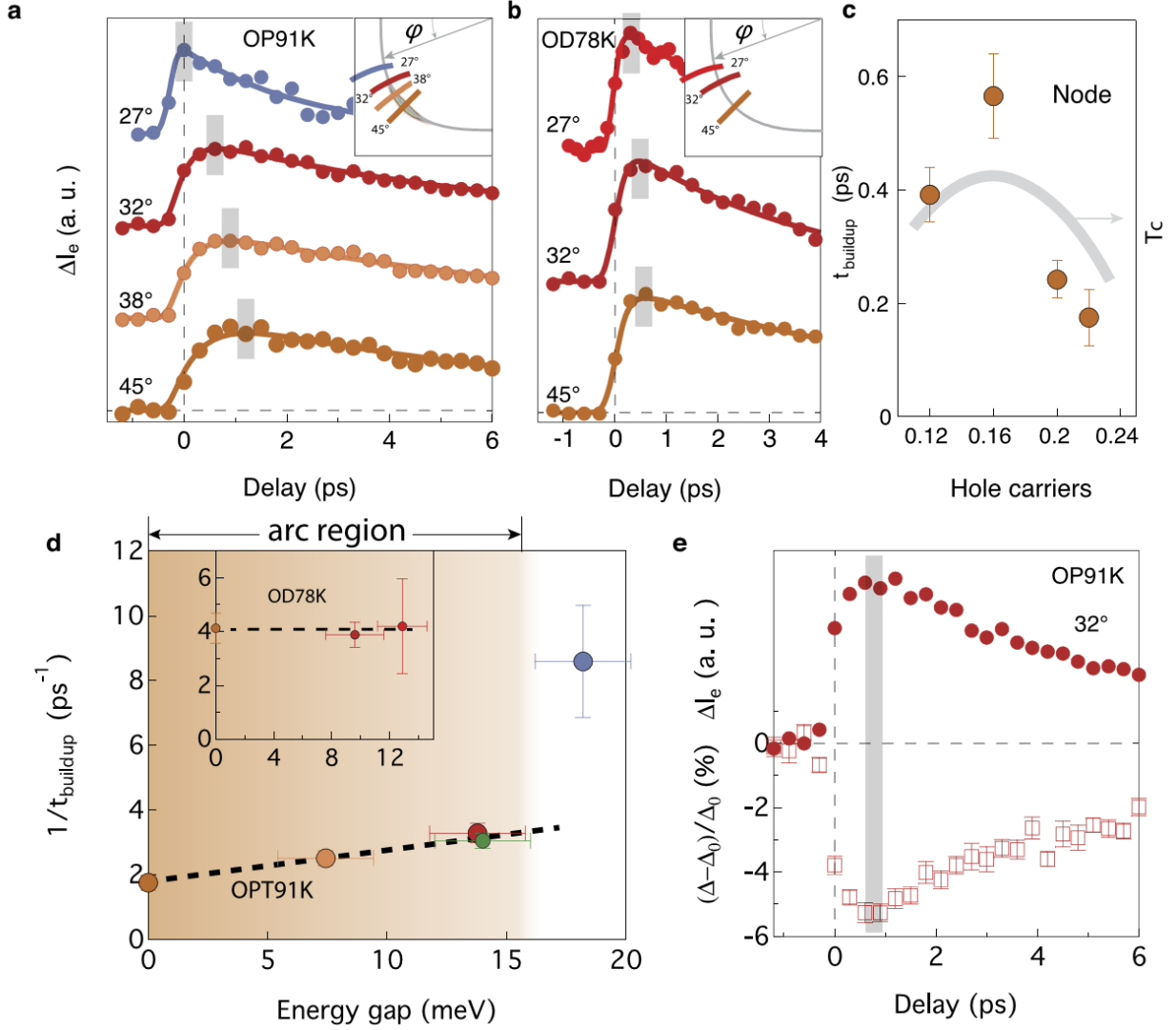After t_{buildup}, what are left behind are "unpaired" excited quasiparticles, meaning that

Figure 4.4. Momentum dependence of the buildup time. These measurements were taken at 20 K on nearly optimally (T_c =91 K) and overdoped (T_c =78 K) Bi2212 samples with pump fluence of 2.4 μJ/cm^2. (a) ΔI_e as a function of delay time measured inside (red curves) and outside (blue curve) the Fermi arc region for the optimally doped sample. (b) ΔI_e inside the Fermi arc for an overdoped sample. (c) Doping dependence of the buildup time at the node. (d) The extracted buildup rate $1/t_{buildup}$ from (a) as a function of energy gap at the Fermi momentum. The green data point is an additional measurement not shown in (a). (e) Comparison between ΔI_e and the change of energy gap as a function of delay time at the Fermi surface angle of 32°.

the time reversed partners of these quasiparticles are not simultaneously excited. At a longer timescale, due to momentum-changing scattering, some subset of those "unpaired" excited quasiparticles will change into "paired" ones and quickly recombine. The bottleneck of the recombination process is the conversion of unpaired NEQPs into paired ones, which is considerably slower.[128,123,72] This slow process is what is referred to as bimolecular recombination.

Note that this explanation is similar to that of earlier optical spectroscopy studies, in that the finite buildup time arises because much of the initial photoexcitation energy is stored in the lattice degrees of freedom.[130,131,132] However, the main difference is that we attribute this initial energy specifically to the presence of the superconducting condensate. This is a key aspect to account for the temperature, energy, and fluence dependence here reported, which otherwise cannot be explained.

A cartoon of this physical scenario is shown in Fig. 4.5. In Panel (b) we also show the results of a simulation that uses the RT equations augmented to include stimulated recombination. Without a superconducting condensate (black curve), no buildup time is observed. But when the condensate is present, the results are qualitatively consistent with the experimental observations (red curve).

In Fig. 4.6, we explain the simulation in greater detail. Since the recombination of non-equilibrium electrons is related to the underlying condensate, we define two kinds of non-equilibrium electrons in the system: a) n_p, the number of "paired" non-equilibrium electrons, whose time reversal partners are also excited b) n_d, number of "unpaired" non-equilibrium electrons, whose time reversal partners are not simultaneously excited. Originally, the RT model was derived to describe the dynamics of Cooper pair formation by injecting normal electrons to a condensed pairing system[132], in which the normal electrons are all "unpaired" excited quasiparticles, but here some excited quasiparticles are "paired". To describe the dynamics of a photo-excited system as schematized in Fig. 4.6(a), we use the augmented RT equations

$$\dot{n} = -\beta n_d^2 + 2\gamma_N N - 2\beta n_d n_{th} - \gamma_p n_p$$
$$\dot{N} = \beta n_d^2 - \gamma_N N - \beta n_d n_{th} - \gamma_e N + \gamma_p n_p/2$$
$$\dot{n}_p = -\gamma_d n_p + 2\gamma_N N - \gamma_p n_p$$
$$n = n_d + n_p$$

(4.3)

n is the number of excited electrons, N is the number of excited bosons, n_{th} is the number of thermally populated electrons, β is the recombination coefficient, γ_N is the pair breaking coefficient by bosons, γ_e is the rate at which bosons are removed from the interacting system, γ_d is the rate at which "paired" non-equilibrium electrons scatter and become "unpaired", and γ_p is the rate of stimulated emission into the existing superconducting condensate. The bosons under consideration are only those which are near twice the energy of the superconducting gap size. Both γ_p and β are proportional to the number of condensed Cooper pairs in the system because of stimulated emission.

Figure 4.6(b) shows the numerical solutions of n for different γ_p at zero temperature (n_{th}=0). Considering that the Fermi velocity in Bi2212 is about 3×10^5 m/s, the lifetime of quasiparticles is about 200 fs, the average distance that a quasiparticle diffuses in 6 ps is
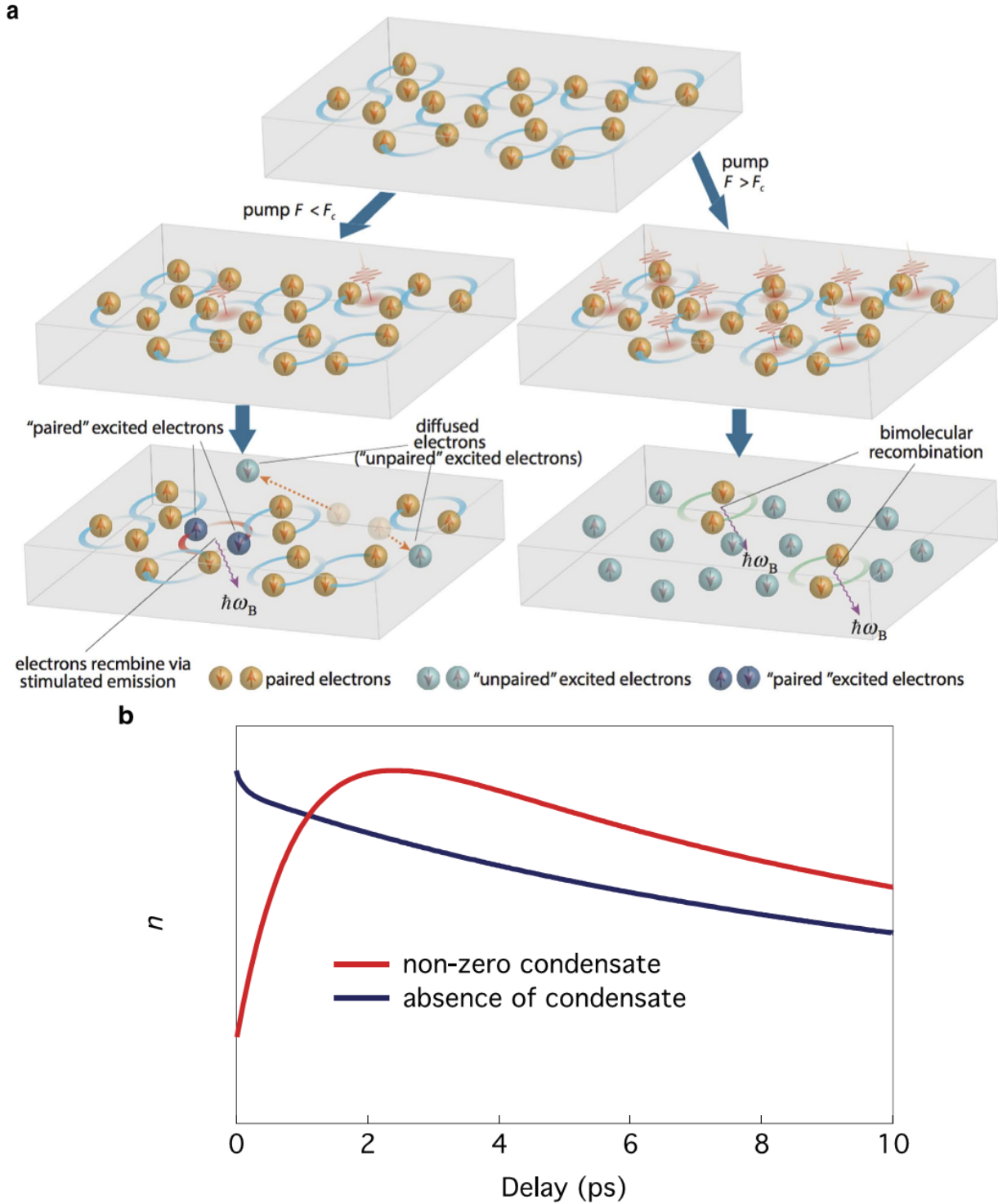
Figure 4.5. The stimulated emission mechanism to slow down the NEQP buildup. (a) Cartoons show the response of a superconductor to a pump laser with fluences less than and greater than the critical fluence. (b) Simulations of the numbers of non-equilibrium electrons (n) as a function of delay time. A nonzero buildup time is observed only in the presence of a condensate. The simulations are described in greater detail in Fig. 4.6 and the text. The parameters are the same as 4.6(b) but with $\gamma_p = 0$ and 1000.
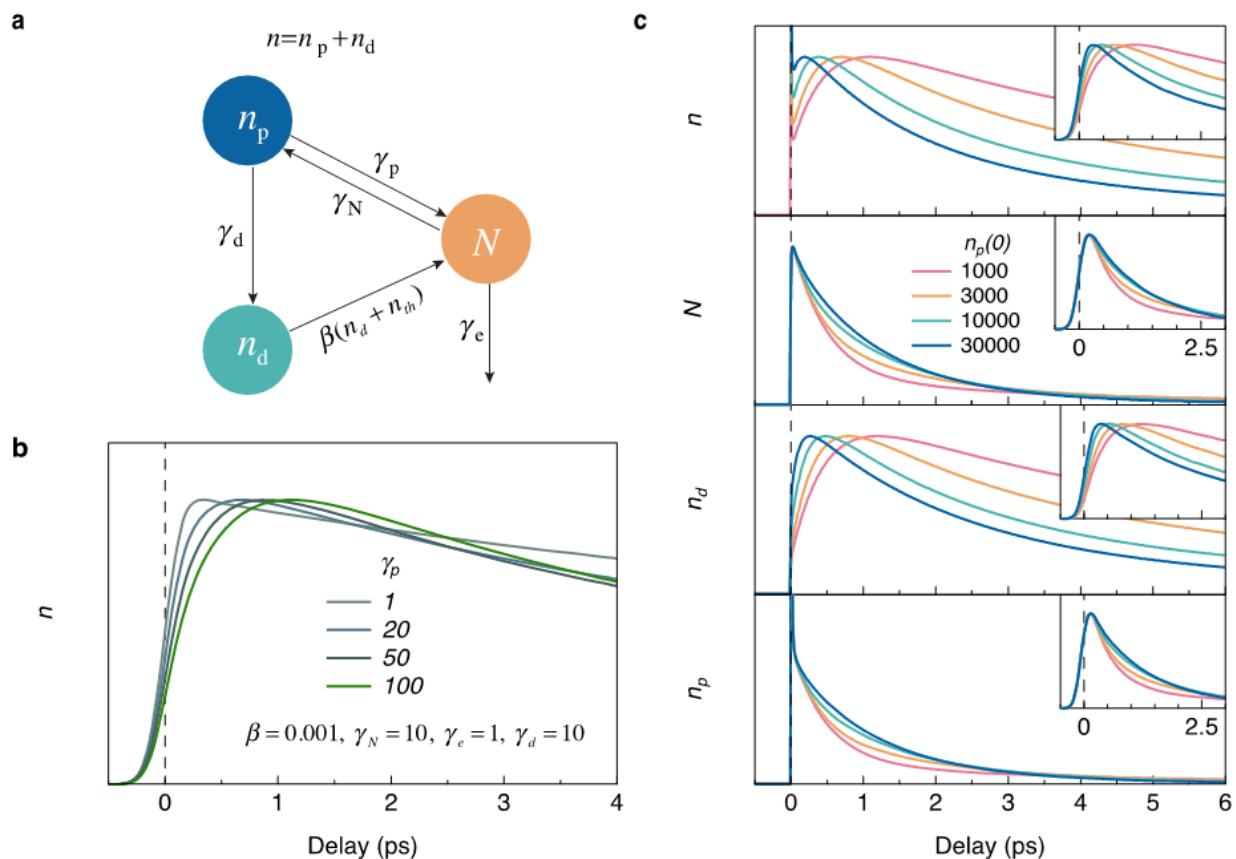
Figure 4.6. Numerical simulation of NEQP dynamics, including stimulated emission. (a) Schematization of the rate equations. n is the number of non-equilibrium electrons, divided into the "paired" excitations (n_p) and "unpaired" excitations. N is the number of bosons. (b) Numerical solutions of the number of non-equilibrium electrons (n) for different stimulated pairing rates γ_p. Corresponding parameters are noted. All the curves are convolved with a system time resolution of 300 fs. (c) Numerical solutions with $\gamma_p = 100$ for different $n_p(0)$. Insets are the corresponding numerical solutions convolved with time resolution. All the curves are normalized to the same height.

about 300 nm with a random walk model, corresponding about 40000 pairs in this region (coherence length is about 1.5 nm). Thus to simulate a small perturbation to the system by pump pulse, we use $n_p(0)$=1000. For small γ_p, solutions of the rate equations give faster buildup time in n, suggesting that to get such a long buildup time as the one shown in Fig. 4.3, the pair formation from stimulated emission must be very fast. To simulate a buildup time of 1 ps, γ_p must be around 100 ps^{-1}, suggesting that the time of the stimulated emission in Bi2212 is on the order of or shorter than 10 fs. Note that these simulations use γ_e on the order of 1 ps^{-1}, which shows that stimulated emission may cause a longer buildup time even when the system is in the weak bottleneck regime. Moreover, simulations indicate that for higher excitation density, the build-up of non-equilibrium electrons is faster (see Fig. 4.6(c)), consistent with the data in Fig. 4.3.

Note that due to the electronic inhomogeneity of Bi2212, the momentum conservation rules are relaxed, i.e. when "paired" NEQPs recombine they can emit bosons with a sufficiently wide range momentum. Within this scenario, the momentum dependence of the buildup time can be easily accounted for by the momentum dependence of the recombination rate (γ), that increases as we move away from the node.[72] Additionally, the absence of buildup time beyond the Fermi arc region puts a strong constraint on the presence of a condensate in this momentum region, another important manifestation of the nodal/off-nodal dichotomy.[28]

One alternate interpretation of our results is that the initial NEQPs far from the node scatter towards the node, allowing the NEQP population near the node to build up over a longer period of time. Such scattering would be induced by the anisotropic form of the superconducting gap. However, this interpretation fails to account for the absence of a buildup time at high fluences or high temperatures, despite the presence of an anisotropic gap. Above the critical fluence, the superconducting gap is not suppressed until about 0.6 ps after the pump pulse,[73] which is after the NEQP population has already reached its maximum. Above the critical temperature, there is still an anisotropic gap present in the form of the pseudogap.

To conclude, our main finding is that upon photoexcitation, the delay in the buildup of the non-equilibrium quasiparticle population in high-temperature superconductors is sensitive to whether there is a superconducting condensate. We propose that our observation reveals the stimulated recombination of photoexcited quasiparticles.

Chapter 5

Relation between electron-boson coupling and superconductivity

Because of the important role of electron-boson interactions in conventional superconductivity, it has long been asked whether any similar mechanism is at play in high-temperature cuprate superconductors. Evidence for strong electron-boson coupling is observed in cuprates with ARPES, in the form of a dispersion kink and peak-dip-hump structure. What is missing is evidence of a causal relation to superconductivity.

In this chapter, we describe a study[133] that revisits the peak-dip-hump structure using both the novel technique of TARPES, and a novel method of analysis: one-dimensional momentum integration. We developed a theoretical framework to understand this new form of analysis, and showed that the peak-dip-hump structure depends on the degree to which the bosonic mode contributes to superconductivity. Further study could address one of the longstanding mysteries of high-temperature superconductivity.

5.1 Introduction

In conventional superconductors, the electron-phonon coupling is the "glue" that allows Cooper pairing, and leads to superconductivity.[134] In high-temperature cuprate superconductors, electrons form Cooper pairs, and have been found to strongly couple to a bosonic mode, but it is unclear whether these two facts are related to each other. Critics observe that cuprates are dominated by the Hubbard repulsion and antiferromagnetic exchange coupling, and that any bosonic interaction appears to be of lesser importance.[12] Experiments have extensively explored the electron-boson interaction, but have only begun to answer this fundamental question.[135]

Early evidence for electron-boson coupling in cuprates was found with ARPES, in the form of a peak-dip-hump structure (PDHS) in the energy profiles of ARPES intensity. The PDHS was eventually understood as one aspect of an electron dispersion kink (see Section 1.2.3). As described in Sections 1.1.6 and 1.1.7, one aspect of the kink is a sudden drop in quasiparticle lifetime, arising from the decay pathway by boson emission. A quasiparticle with a long lifetime is observed as a sharp peak in intensity, while a quasiparticle with short lifetime is observed as a broad hump. The PDHS appears when the peak and hump are seen together in ARPES energy profiles.

Other experimental techniques, such as scanning tunneling microscopy[136] and Raman spectroscopy,[137] have observed features that are similar to the PDHS. However, in this context the PDHS does not have exactly the same interpretation. The difference is that ARPES studies look at a particular point in momentum space, while these other techniques effectively integrate over a large range of momentum. At a single momentum, the peak represents a single quasiparticle pole; but in a momentum-integrated measurement, the peak represents a pileup of many quasiparticle poles at the edge of the superconducting gap. Some simulations have shown that electron-boson coupling could create a momentum-integrated PDHS,[138] but other studies have argued that it arises from charge order or the pseudogap.[139,137]

Bridging the devide between momentum-integrated and momentum-resolved techniques, there have been several recent ARPES studies that integrate across just one dimension of momentum.[29,30,140,87] This analysis sacrifices resolution perpendicular to the Fermi surface, but maintains resolution along the Fermi surface and greatly improves statistics. This method of analysis could be particularly useful when applied to the electron-boson coupling, because, as discussed in Section 1.1.7, the spectral density function reduces to a particularly simple form when integrated over momentum.

Here we look at the PDHS in Bi2212, applying TARPES and integrating along one-dimensional momentum cuts. As laser pulses suppress superconductivity, spectral weight shifts into the dip, causing an increase of intensity near 70 meV (near the kink). We quantify the strength of the dip by measuring the magnitude of the increase of intensity, finding that it is stronger away from the node, and roughly equal in underdoped and overdoped samples. We also observe an increase of intensity near 140 meV, which could indicate a second kink or a second-order effect of the first kink.

To understand the PDHS in the context of one-dimensional momentum integration, we built a simulation using Eliashberg theory in a superconductor with an Einstein boson. We find that a PDHS appears only when both superconductivity and electron-boson coupling are simultaneously present. Furthermore, the strength of the dip depends on the extent to which the boson couples to the d-wave superconducting parameter. Further study may be able to determine whether and how much the bosonic mode is involved in the mechanism of high-temperature superconductivity.
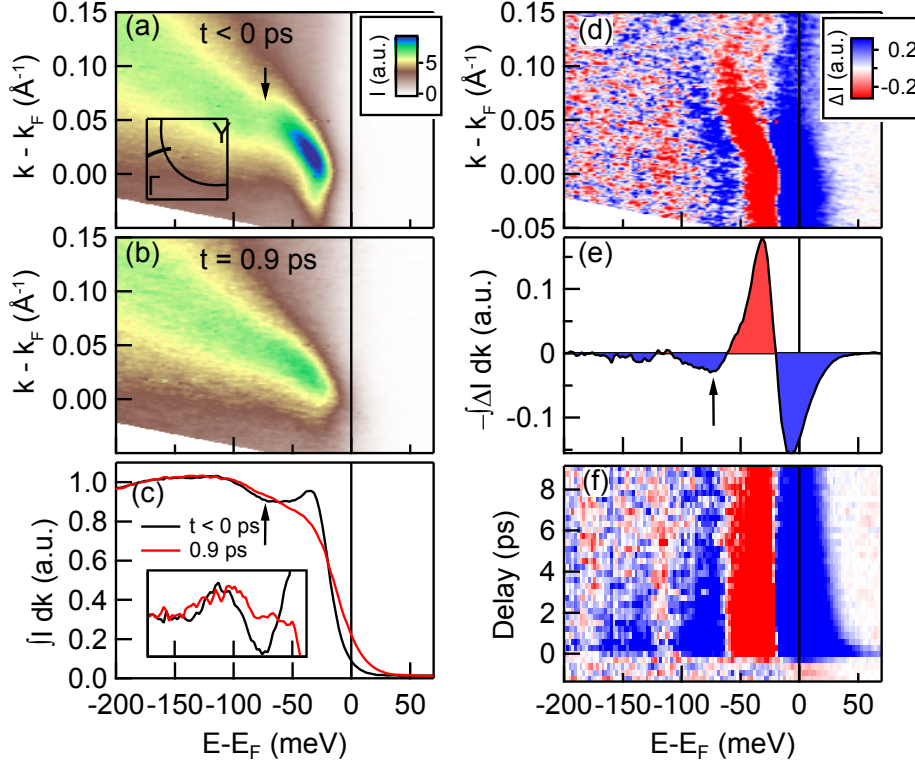
Figure 5.1. Measuring the peak-dip-hump structure. (a) The ARPES intensity map of an overdoped Bi2212 sample ($T_c = 70$ K) at equilibrium at 20 K. The inset shows where in momentum space the cut was taken. (b) A map of the same sample 0.9 ps after pumping with a 24 μJ/cm^2 pulse. (c) The intensity in (a) and (b) integrated over momentum. The inset shows a closeup of the two curves (after subtracting a quadratic fit). (d) A map of the change in intensity between (a) and (b). (f) The momentum-integrated change of intensity at t = 0.9 ps. (e) The momentum-integrated change of intensity plotted as a function of delay time.

5.2 Pump-induced intensity difference

To introduce our technique, we begin with an overdoped (OD) Bi2212 sample ($T_c = 70$ K), which is shown in Figure 5.1. Panel (a) shows the ARPES intensity map at equilibrium at 20 K, and Panel (b) shows the same map 0.9 ps after the pump pulse. Every measurement in this study uses a 24 μJ/cm^2 pump pulse, which is sufficient to suppress superconductivity completely. The arrow roughly indicates the position of the kink. Upon pumping, the kink is significantly weakened, although it does not disappear entirely. The superconducting gap is seen between the ARPES intensity and the Fermi energy E_F. Although superconductivity is suppressed by pumping, a gap remains because of the transient pseudogap state.[73,75] This particular measurement is taken along the momentum cut indicated in the inset of Panel (a), where both the superconducting gap and pseudogap are present.

Figure 5.1(c) shows ARPES intensity integrated over momentum. The integration win-

dow is given by our measurement window, which is slightly larger than the maps shown. To account for fluctuations in laser power, the intensity curves are normalized by the intensity averaged at high binding energy (200 to 300 meV). The intensity at equilibrium shows a clear PDHS, but 0.9 ps after pumping, the peak and dip have been suppressed. The inset shows a closeup of the two curves, and one can see that pumping causes intensity to fill into the dip. These observations motivated us to consider the difference between curves.

Figure 5.1(d) shows a map of the intensity difference (ΔI), and Panel (e) shows $-\Delta I$ integrated over momentum. Panel (e) uses the same units as Panel (c), so that 0.1 is approximately a 10% change in the spectral weight. The increase of intensity near E_F (blue region) corresponds to intensity filling the superconducting gap, and an increase in the occupation fraction of the quasiparticle states above E_F. The decrease of intensity near 30 meV (red region) corresponds to the suppresion of the peak in the PDHS, as well as a decrease in the occupation fraction of the quasiparticle states. The most striking observation is an increase of intensity near 70 meV (indicated by arrow) which matches with the dip in Panel (c) and the kink in Panel (a). This increase of intensity cannot be explained by a change in the occupation fraction of electrons, and implies a change in the density of states itself.

In Figure 5.1(f), we show the delay dependence of the momentum-integrated ΔI. It is clear that ΔI appears nearly immediately after pumping, and decreases over several picoseconds, but its qualitative features do not change during that time. The saturated color scale also make clear an increase of intensity near 140 meV, which will be discussed further later.

In order to make these precise measurements, we found it necessary to correct for several systematic errors. Following standard procedure, we correct for the nonlinear sensitivity of our detector.[68] We partially correct for the instrumental energy resolution by applying five iterations of the Lucy-Richardson deconvolution algorithm (this was not necessary in previous chapters which did not look at any detailed energy dependence).[141] We found that some error was caused by variations in the sensitivity of the camera, and we corrected for this by accumulating data over several days and measuring the systematic bias. As in Chapter 3, we correct for drift in the Fermi level over time. We also correct for the pump-induced shift in chemical potential that was the focus of Chapter 3, since it is not the focus of this study.

5.3   Momentum and doping dependence

In the previous section, we took overdoped Bi2212 and integrated ΔI over a particular momentum cut. The next step is to expand this measurement to other momenta and other dopings. Figure 5.2(a) and 5.2(b) show the $-\Delta I$ curves measured on underdoped (UD) Bi2212 ($T_c = 78$ K), and OD Bi2212 ($T_c = 70$ K), both measured at 20 K. Each curve is taken at a different momentum cut, parametrized by the Fermi surface angle φ, defined in the upper right panel. In order to compare different curves, we normalize each measurement such that the equilibrium intensity at 100 meV is 1. In each curve, we identify minima near
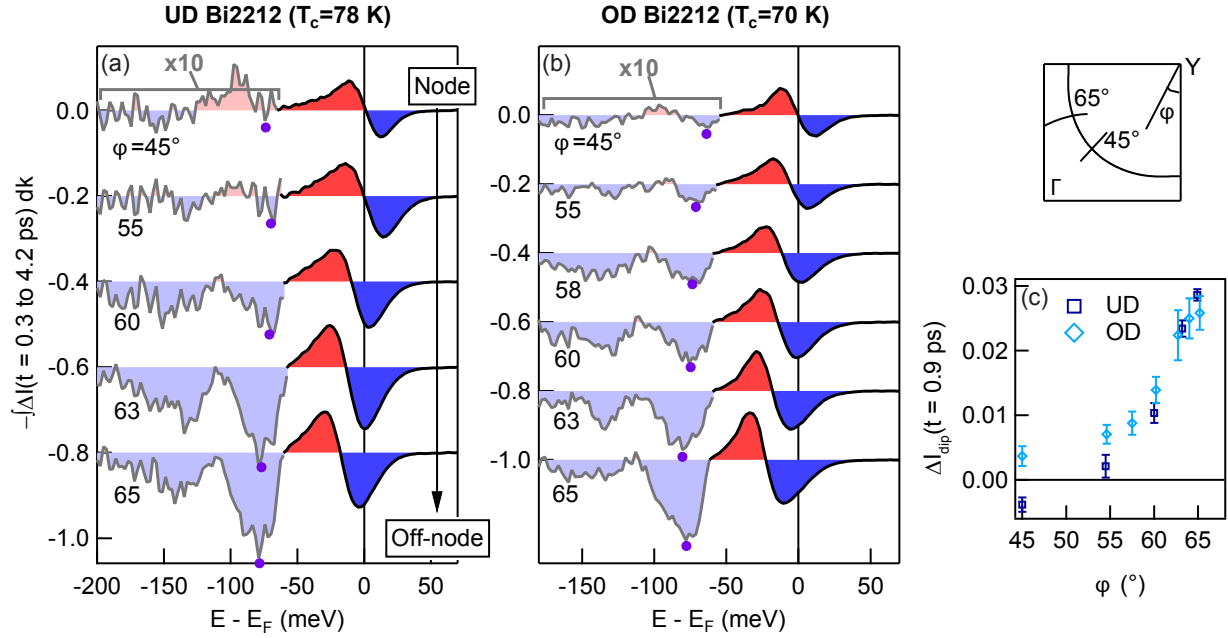
Figure 5.2. The momentum-integrated ΔI curves for an underdoped Bi2212 sample (a) and an overdoped sample (b). Each curve corresponds to a different momentum cut (parametrized by φ, defined in the upper right panel), and the curves are offset for clarity. Parts of each curve have been magnified by a factor of 10. The curves are averaged from 0.3 to 4.2 ps to improve signal to noise ratio; this does not qualitatively change the results. Purple circles indicate minima in the curves. (c) The change of intensity at 0.9 ps, averaged over a 20 meV window centered at the purple circles.

70 meV, corresponding to the dip. We define the dip strength $\Delta I_{\rm dip}$, shown in Fig. 5.2(c), to be the change of intensity averaged in a 20 meV window centered at the minimum.

Near the node, $\Delta I_{\rm dip}$ is slightly larger in the UD sample than in the OD sample. But apart from this small difference, both samples have a similar dip strength. This disconfirms any relation between the dip and the pseudogap, since the pseudogap is much smaller in the overdoped sample.[14] It also suggests that the bilayer splitting, which sometimes causes a PDHS in overdoped samples near the antinode,[142,143,144,145] is not the source of the PDHS in our measurements.

We also observe that $\Delta I_{\rm dip}$ increases with φ. This is consistent with previous studies, which all agree that the PDHS is much stronger near the anti-node.[43,44,45,47,46,48,50] The momentum dependence of the PDHS is typically attributed to the electron-boson coupling strength, which, in the superconducting state, increases with distance from the node.[50,61,59] However, we will later propose that the momentum dependence of $\Delta I_{\rm dip}$ is related to the size of the gap.

Finally, we note additional minima appearing near 140 meV. Given the similarity between the minima at 70 meV and 140 meV, it is tempting to identify the feature at 140 meV with an additional dip structure. Such additional dip structures have previously been observed in sensitive ARPES measurements.[66]

5.4   Characteristic energy scales

In Figure 5.3, we identify local minima and maxima in the momentum integrated intensity curves, and show how these energy scales depend on doping and momentum. Away from the node, p_1 corresponds to the peak in the PDHS, which arises from a pileup of quasiparticle states at the superconducting gap edge. At the superconducting node, there is no superconducting gap, and p_1 instead corresponds to the increase in electronic temperature. Thus, as we move away from the node, p_1 starts near electronic temperature scale, and ends near the superconducting gap size $\Delta_{\rm eq}$.

The energy scale p_2 corresponds to the dip in the PDHS, which nearly matches the kink energy. The kink energy is significant because it is expected to appear at $\Delta + \Omega$, where Δ is the superconducting gap size and Ω is the energy of the bosonic mode.[48] Whether Δ is the maximum gap size, or the gap size at the same momentum is an issue under dispute, as discussed in Section 1.2.3. However, we note that p_2 is not a very precise way to estimate the kink energy, since p_2 is not exactly the energy of the dip, nor is the dip at exactly the same energy as the kink. In earlier measurements of OD Bi2212 samples, the kink appears near 60 meV at the node[49] and near 40 meV at the antinode.[51] This does not match the energy of p_2 in panel (c) which appears near 60 meV at the node, and nearly 80 meV away from the node. Later, simulations will corroborate our conclusion that p_2 may deviate slightly from the kink energy.

The energy scales p_3 and p_4 are related to the mysterious feature at 140 meV. One
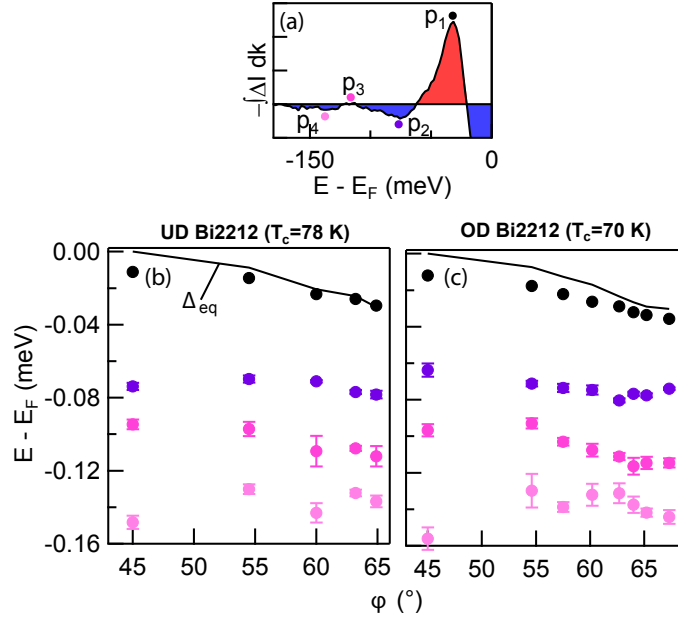
Figure 5.3. Characteristic energy scales of the peak-dip-hump structure. (a) Illustration of the characteristic energy scales observed in $\int \Delta I \mathrm{d}k$. p_i is the energy of the ith minima or maxima below the E_F. These characteristic energy scales are shown as a function of Fermi surface angle in UD Bi2212 (b) and OD Bi2212 (c). The size of the gap at equilibrium (Δ_{eq}) is estimated with standard fitting methods.[129] Error bars are determined by the variance between measurement cycles, although measurements may also be affected by systematic error.

interpretation is that this feature arises from another bosonic coupling mode at energy Ω', with p_4 appearing near $\Delta + \Omega'$. A second possibility is that they are a second-order feature of the first bosonic coupling mode, with p_4 appearing near $\Delta + 2\Omega$.

5.5   Simulations of momentum-integrated intensity

The PDHS has a different interpretation depending on whether it is measured at a single momentum, or using momentum-integrated techniques. To interpret the PDHS in the context of one-dimensional momentum integration, we need to develop yet another interpretation. Here we develop a framework based on the equations in Section 1.1.6 and simulations in Section 1.1.7.

We begin with the Nambu-Gor'kov Green's function and self-energy. As before, we neglect $\bar{\phi}$ and χ. The ARPES intensity is given by

$$I(k, \omega) = f(\omega) I_0(k) A(k, \omega), \tag{5.1}$$

where $f(\omega)$ is the electron distribution function, $I_0(k)$ is the square of the dipole matrix element discussed in Section 2.1, and A is the spectral density function. Using Eq. (1.24), we derive

$$\int I(\omega, k) \mathrm{d}k \propto f(\omega) \, \mathrm{Re} \frac{Z(\omega)\omega}{\sqrt{(Z(\omega)\omega)^2 - \phi(\omega)^2}}, \tag{5.2}$$

with Z and ϕ being the diagonal and off-diagonal terms of the self-energy. Equation (5.2) makes use of two approximations. First, we assume that the integration window is large enough to cover most of the intensity of the dispersion. Second, we assume that Σ, I_0, and the bare electron velocity are independent of momentum within the window of integration.

Equation (5.2) generates a PDHS only when two conditions are simultaneously fulfilled. First, ϕ must be nonzero, or else the integrated intensity reduces to $f(\omega)$, a function with no PDHS. This implies that the presence of a superconducting gap. Second, either Z or ϕ must have some dependence on energy; a kink fulfills this condition. In our equilibrium data (except those taken at the node), both of these conditions are fulfilled by the presence of a gap and a kink. In pumped data, the gap is partially or completely suppressed, which will partially or completely suppress the PDHS.

In order to make more specific predictions, we constructed the simulations shown in Fig. 5.4. These are built from the simulations in Section 1.1.7, using the Eliashberg equation (Eq. (1.22)) and an Einstein boson at 35 meV. The equilibrium simulations all use $T = 20$ K and a gap size of 30 meV, while the transient simulations all use $T = 80$ K and set ϕ to zero. Following Ref. 8, we use separate electron-boson coupling constants to calculate Z and ϕ, with $\lambda_Z = 1$ and various values of λ_ϕ. The physical meaning of λ_Z is the isotropic component of the electron-boson coupling, while λ_ϕ is the component with $d_{x^2-y^2}$ symmetry. λ_ϕ is, in essence, the extent to which this particular boson contributes to d-wave superconductivity. In equilibrium simulations, we keep the superconducting gap size fixed by adding a real constant
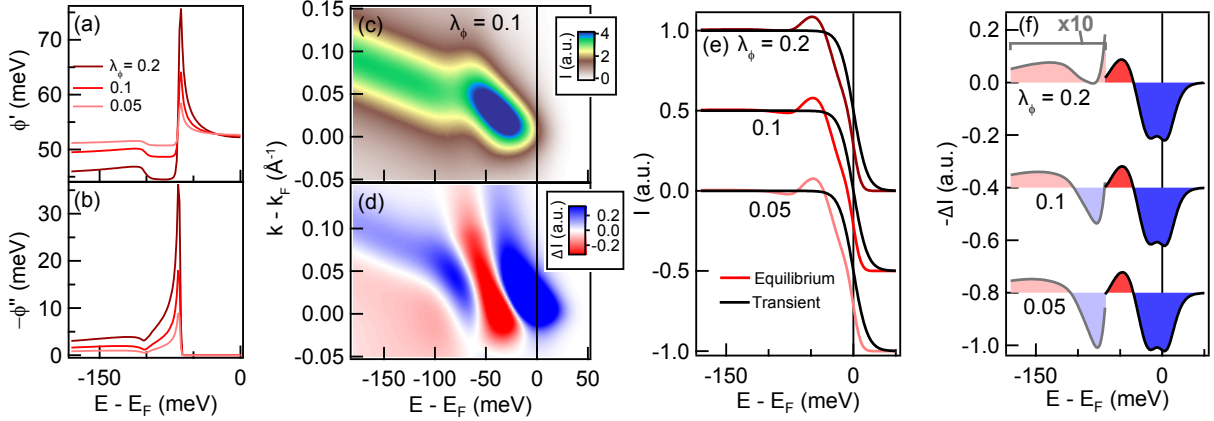
Figure 5.4. Simulations of ARPES intensity using Eliashberg equations, an Einstein boson at 35 meV with coupling strength $\lambda_Z = 1$, and various values of λ_ϕ. (a,b) The real and imaginary parts of ϕ at 20 K. A constant is added to ϕ' in order to fix the superconducting gap is 30 meV. (c) The ARPES intensity map for $\lambda_\phi = 0.1$. (d) The pump-induced change in ARPES intensity. The transient spectra are simulated by taking $\phi = 0$ and $T = 80$ K. (e) The momentum integrated intensity in the equilibrium and transient state, calculated from Eq. (5.2). (f) The pump-induced change in momentum integrated intensity. Note that parts of the curves are magnified by a factor of 10.

to ϕ; this real constant may be interpreted as the contribution to superconductivity from other sources. The real and imaginary components of ϕ at equilibrium are shown in Figs. 5.4(a) and 5.4(b), respectively.

Figure 5.4(c) shows the simulated equilibrium ARPES intensity map for $\lambda_\phi = 0.1$, and Fig. 5.4(d) shows a map of the difference between equilibrium and transient intensity. In order to make the simulation more realistic, we include a 35 meV contribution to the imaginary self-energy from impurity scattering, and a 15 meV instrumental energy resolution. Identical to the experimental procedure, we apply a normalization factor to each map so that they have the same average intensity between 200 and 300 meV. The simulations suggest that it is inappropriate to normalize intensity at high binding energy; however, it was experimentally necessary to correct for laser power fluctuations. The resulting intensity maps are remarkably similar to those observed in Fig. 5.1.

Figure 5.4(e) shows the momentum-integrated intensity in both the equilibrium and transient states. In the equilibrium state, we see a PDHS similar to that observed in experiment, and in the transient state, the PDHS disappears because of the suppression of the superconducting gap. The differences between the equilibrium and transient curves are shown in Fig. 5.4(f), and they resemble the experimental observations in Fig. 5.2. If we identify p_2 as we did in Fig. 5.3, we find that it appears around 80 meV, which is somewhat larger than the value of $\Delta + \Omega = 65$ meV. This may explain why in experimental measurements, p_2 does not precisely match the kink energy.

The most shocking prediction is that as λ_ϕ increases, the dip strength decreases. By

looking at the experimentally observed dip strength and comparing to simulations, we could in principle estimate the value of λ_ϕ, which would tell us the extent to which the electron-boson kink contributes to high-temperature superconductivity.

5.6 Discussion

In this study, we explored the PDHS in cuprates by using two novel techniques. The first technique, TARPES, allows us to quickly compare measurements with and without a superconducting gap. The second technique is to integrate the intensity over a single dimension of momentum, unlike previous studies which either took measurements at single momenta,[43,44,45,47,46,48,50] or used techniques that integrate over large regions of momentum.[136,137] One-dimensional integration is a particularly fruitful way to look at electron-boson coupling because it improves statistics, and because the intensity is expected to follow the simple expression in Eq. (5.2). Note that other studies have used the full momentum dependence of ARPES intensity to extract the Z and ϕ functions,[135] but the method used here is simpler and does not require as much precision.

When looking at the change of intensity upon laser pumping, we observe a shift of intensity into the dip of the PDHS. The maximum change of intensity occurs near 70 meV for a wide range of momenta, in both underdoped and overdoped samples. The presence over a wide doping range suggests that the observed structure is neither related to bilayer splitting nor to the pseudogap. The dip strength increases with distance from the node, which could be related to the increasing kink strength, but on the basis of Eq. (5.2) we argue that it is also related to the increasing superconducting gap size.

We also observe a similar change of intensity near 140 meV. This may arise from a dip produced by a second bosonic mode,[66] but if so it cannot be a phonon, given that the phononic modes reach no higher than 80 meV.[146] Another possibility is that the dip at 140 meV is a second-order effect of the same bosonic mode that produced the dip at 70 meV. The first-order effect would be expected to appear near $\Delta + \Omega$, and the second-order effect is a replica near $\Delta + 2\Omega$. Although, both experiment and simulations suggest that the kink energy is not precisely the same as the dip energy, so it is difficult to estimate Ω in this way. Second-order features appear in simulations, visible at 100 meV in Figs. 5.4(a) and 5.4(b), although they do not have a noticeable impact on the integrated intensity in Fig. 5.4(f). To properly calculate second-order effects, it may be necessary to use polaronic simulations.[6]

Our most significant finding from the simulations is that the strength of the dip depends on the parameter λ_ϕ, the component of the electron-boson coupling that contributes to d-wave superconductivity. At first glance, the evidence suggests that the boson does not contribute very much, which corroborates the results in Ref. 135. However, we caution against drawing any specific conclusions from the present simulations, which make use of several simplifications. First, we use a single constant gap size, when in the real system, the gap size is a function of momentum. Second, in using Eq. (5.2), we assume the integration window is very large. In practice, the integration window is finite, which could lead to

a PDHS even in the nodal equilibrium data, which is experimentally observed in Fig. 5.2. Third, we do not include the self-energy contribution from electron-electron interactions, nor do we attempt to account for the pseudogap. Nonetheless, with more systematic calculations, we are hopeful that comparisons to experiment may help address the longstanding question of how the electron-boson coupling relates to high-temperature superconductivity.

Chapter 6

Concluding remarks

In this dissertation, we have used TARPES on cuprates, and performed detailed investigations of unusual phenomena. In Chapter 3, we showed that pumping cuprates causes their chemical potential to change, and that this is a consequence of an asymmetrical density of states. We use information about the chemical potential to show that the pseudogap inverts the asymmetrical density of states, which narrows down the many theories of the pseudogap. In Chapter 4, we showed that the population of non-equilibrium quasiparticles takes longer to build up after pumping, if a superconducting condensate is present. Our interpretation is that the stimulated recombination of Cooper pairs is slowing down the buildup. In Chapter 5, we investigate the peak-dip-hump structure, a signature of electron-boson coupling, by use of one-dimensional integration. We demonstrate that this is a powerful way to look at electron-boson coupling, and could determine how much it is involved in Cooper pairing.

Through most of my career, we have tried to emphasize the value that TARPES contributes to traditional equilibrium ARPES experiments. The primary argument has been that the pump-induced non-equilibrium state is very different from the high-temperature equilibrium state. While this is true, the sheer novelty of non-equilibrium electron physics also makes it difficult to intuitively interpret. It is worth noting that several of the models we have developed are based on similarity to equilibrium, rather than difference. We believe that in principle, several of these phenomena could be observed with equilibrium ARPES, although it may be quite challenging for various practical reasons. It goes to show that new experimental techniques can contribute value in unexpected ways.

We hope that future experimentalists continue to create new techniques and catalogue new phenomena. But we also emphasize the importance of following up these studies with more systematic research. For example, a systematic study of the chemical potential could establish more than just simple qualitative facts about the structure of the pseudogap. To determine the role of electron-boson coupling in Cooper pairing, it would be necessary to perform more systematic experiments and calculations. Although the venerable mysteries

of high-temperature superconductivity are quite daunting, I am confident that they can be resolved by the dedication and hard work of researchers.

Bibliography

1. Rickayzen, G. *Superconductivity*, chap. 2, 51–115 (Marcel Dekker, Inc., New York, 1969).

2. Scalapino, D. J. *Superconductivity*, chap. 10, 449–560 (Marcel Dekker, Inc., New York, 1969).

3. Tinkham, M. *Introduction to Superconductivity* (Dover Publications, Inc., New York, 1996), 2nd edn.

4. Annett. *Superconductivity, Superfluids and Condensates* (Oxford University Press, 2004).

5. Fröhlich, H. Theory of the Superconducting State. I. The Ground State at the Absolute Zero of Temperature. *Phys. Rev.* **79**, 845–856 (1950).

6. Verdi, C., Caruso, F. & Giustino, F. Origin of the crossover from polarons to Fermi liquids in transition metal oxides. *Nat. Commun.* **8**, 15769 (2017).

7. LaShell, S., Jensen, E. & Balasubramanian, T. Nonquasiparticle structure in the photoemission spectra from the Be(0001) surface and determination of the electron self energy. *Phys. Rev. B* **61**, 2371–2374 (2000).

8. Sandvik, A. W., Scalapino, D. J. & Bickers, N. E. Effect of an electron-phonon interaction on the one-electron spectral weight of a d -wave superconductor. *Phys. Rev. B* **69**, 094523 (2004).

9. Anderson, P. W. Personal history of my engagement with cuprate superconductivity, 1986–2010. *Int. J. Mod. Phys. B* **25**, 1–39 (2011).

10. Electron correlations in narrow energy bands. *Proc Royal Soc A* **276**, 238 (1963).

11. Varma, C. M. Marginal Fermi-liquid theory of the normal and superconductive state of Cu - O compounds. *Annals of the New York Academy of Sciences* **581**, 9–14 (1990).

12. Anderson, P. W. Is There Glue in Cuprate Superconductors? *Science* **316**, 1705–1707 (2007).

13. Sigrist, M. & Rice, T. M. Unusual paramagnetic phenomena in granular high-temperature superconductors—A consequence of d-wave pairing? *Rev. Mod. Phys.* **67**, 503–513 (1995).

14. Vishik, I. M. *et al.* Phase competition in trisected superconducting dome. *Proc. Natl. Acad. Sci. USA* **109**, 18332–18337 (2012).

15. Maiti, S. & Chubukov, A. V. Superconductivity from repulsive interaction. *AIP Conference Proceedings* **1550**, 3–73 (2013).

16. Devereaux, T. P., Cuk, T., Shen, Z.-X. & Nagaosa, N. Anisotropic Electron-Phonon Interaction in the Cuprates. *Phys. Rev. Lett.* **93**, 117004 (2004).

17. Loeser, A. G., Shen, Z.-X., Dessau, D. S., Marshall, D. S., Park, C. H., Fournier, P. & Kapitulnik, A. Excitation Gap in the Normal State of Underdoped $Bi_2Sr_2CaCu_2O_{8+\delta}$. *Science* **273**, 325–329 (1996).

18. Marshall, D. S. *et al.* Unconventional Electronic Structure Evolution with Hole Doping in $Bi_2Sr_2CaCu_2O_{8+\delta}$: Angle-Resolved Photoemission Results. *Phys. Rev. Lett.* **76**, 4841–4844 (1996).

19. Damascelli, A., Hussain, Z. & Shen, Z.-X. Angle-resolved photoemission studies of the cuprate superconductors. *Rev. Mod. Phys.* **75**, 473–541 (2003).

20. Norman, M. R., Pines, D. & Kallin, C. The pseudogap: friend or foe of high T_c? *Adv. Phys.* **54**, 715–733 (2005).

21. Hashimoto, M., Vishik, I. M., He, R.-H., Devereaux, T. P. & Shen, Z.-X. Energy gaps in high-transition-temperature cuprate superconductors. *Nat. Phys.* **10**, 483–495 (2014).

22. Lee, W. S. *et al.* Abrupt onset of a second energy gap at the superconducting transition of underdoped Bi2212. *Nature* **450**, 81–84 (2007).

23. Kondo, T., Takeuchi, T., Kaminski, A., Tsuda, S. & Shin, S. Evidence for Two Energy Scales in the Superconducting State of Optimally Doped $(Bi,Pb)_2(Sr,La)_2CuO_{6+\delta}$. *Phys. Rev. Lett.* **98**, 267004 (2007).

24. Ma, J.-H. *et al.* Coexistence of Competing Orders with Two Energy Gaps in Real and Momentum Space in the High Temperature Superconductor $Bi_2Sr_{2-x}La_xCuO_{6+\delta}$. *Phys. Rev. Lett.* **101**, 207002 (2008).

25. Khasanov, R. *et al.* Evidence for a Competition between the Superconducting State and the Pseudogap State of $(BiPb)_2(SrLa)_2CuO_{6+\delta}$ from Muon Spin Rotation Experiments. *Phys. Rev. Lett.* **101**, 227002 (2008).

26. Kondo, T., Khasanov, R., Takeuchi, T., Schmalian, J. & Kaminski, A. Competition between the pseudogap and superconductivity in the high-T_c copper oxides. *Nature* **457**, 296–300 (2009).

27. Hashimoto, M. *et al.* Direct spectroscopic evidence for phase competition between the pseudogap and superconductivity in $Bi_2Sr_2CaCu_2O_{8+\delta}$. *Nat. Mater.* **14**, 37–42 (2015).

28. Fu, H. & Lee, D.-H. Dichotomy between the nodal and antinodal excitations in high-temperature superconductors. *Phys. Rev. B* **74**, 174513 (2006).

29. Reber, T. J. *et al.* The origin and non-quasiparticle nature of Fermi arcs in Bi$_2$Sr$_2$CaCu$_2$O$_{8+\delta}$. *Nat. Phys.* **8**, 606–610 (2012).

30. Reber, T. J. *et al.* Prepairing and the "filling" gap in the cuprates from the tomographic density of states. *Phys. Rev. B* **87**, 060506 (2013).

31. Kondo, T. *et al.* Point nodes persisting far beyond T$_c$ in Bi2212. *Nat. Commun.* **6**, 7699 (2015).

32. Emery, V. J. & Kivelson, S. A. Importance of phase fluctuations in superconductors with small superfluid density. *Nature* **374**, 434–437 (1995).

33. Chakravarty, S., Laughlin, R. B., Morr, D. K. & Nayak, C. Hidden order in the cuprates. *Phys. Rev. B* **63**, 094503 (2001).

34. Qi, Y. & Sachdev, S. Effective theory of Fermi pockets in fluctuating antiferromagnets. *Phys. Rev. B* **81**, 115129 (2010).

35. Lee, P. A. Amperean Pairing and the Pseudogap Phase of Cuprate Superconductors. *Phys. Rev. X* **4**, 031017 (2014).

36. Yang, K.-Y., Rice, T. M. & Zhang, F.-C. Phenomenological theory of the pseudogap state. *Phys. Rev. B* **73**, 174501 (2006).

37. Rice, T. M., Yang, K.-Y. & Zhang, F. C. A phenomenological theory of the anomalous pseudogap phase in underdoped cuprates. *Rep. Prog. Phys.* **75**, 016502 (2012).

38. LeBlanc, J. P. F. Signatures of a momentum independent pseudogap in the electronic density of states and Raman spectroscopy of the underdoped cuprates. *New J. Phys.* **16**, 113034 (2014).

39. Yang, H.-B., Rameau, J. D., Johnson, P. D., Valla, T., Tsvelik, A. & Gu, G. D. Emergence of preformed Cooper pairs from the doped Mott insulating state in Bi$_2$Sr$_2$CaCu$_2$O$_{8+\delta}$. *Nature* **456**, 77–80 (2008).

40. Hashimoto, M. *et al.* Particle-hole symmetry breaking in the pseudogap state of Bi2201. *Nat. Phys.* **6**, 414–418 (2010).

41. He, R.-H. *et al.* From a Single-Band Metal to a High-Temperature Superconductor via Two Thermal Phase Transitions. *Science* **331**, 1579–1583 (2011).

42. Sakai, S. *et al.* Raman-Scattering Measurements and Theory of the Energy-Momentum Spectrum for Underdoped Bi$_2$Sr$_2$CaCuO$_{8+\delta}$ Superconductors: Evidence of an *s*-Wave Structure for the Pseudogap. *Phys. Rev. Lett.* **111**, 107001 (2013).

43. Dessau, D. S. *et al.* Anomalous spectral weight transfer at the superconducting transition of Bi$_2$Sr$_2$CaCu$_2$O$_{8+\delta}$. *Phys. Rev. Lett.* **66**, 2160–2163 (1991).

44. Hwu, Y. *et al.* Electronic spectrum of the high-temperature superconducting state. *Phys. Rev. Lett.* **67**, 2573–2576 (1991).

45. Dessau, D. S. *et al.* Nature of the high-binding-energy dip in the low-temperature photoemission spectra of $Bi_2Sr_2CaCu_2O_{8+\delta}$. *Phys. Rev. B* **45**, 5095–5098 (1992).

46. Norman, M. R. *et al.* Unusual Dispersion and Line Shape of the Superconducting State Spectra of $Bi_2Sr_2CaCu_2O_{8+\delta}$. *Phys. Rev. Lett.* **79**, 3506–3509 (1997).

47. Fedorov, A. V., Valla, T., Johnson, P. D., Li, Q., Gu, G. D. & Koshizuka, N. Temperature Dependent Photoemission Studies of Optimally Doped $Bi_2Sr_2CaCu_2O_8$. *Phys. Rev. Lett.* **82**, 2179–2182 (1999).

48. Campuzano, J. C. *et al.* Electronic Spectra and Their Relation to the (π, π) Collective Mode in High- T_c Superconductors. *Phys. Rev. Lett.* **83**, 3709–3712 (1999).

49. Lanzara, A. *et al.* Evidence for ubiquitous strong electron-phonon coupling in high-temperature superconductors. *Nature* **412**, 510–514 (2001).

50. Kaminski, A. *et al.* Renormalization of Spectral Line Shape and Dispersion below T_c in $Bi_2Sr_2CaCu_2O_{8+\delta}$. *Phys. Rev. Lett.* **86**, 1070–1073 (2001).

51. Cuk, T. *et al.* Coupling of the B-1g phonon to the antinodal electronic states of $Bi_2Sr_2Ca_{0.92}Y_{0.08}Cu_2O_{8+\delta}$. *Phys. Rev. Lett.* **93**, 117003 (2004).

52. Meevasana, W. *et al.* Doping Dependence of the Coupling of Electrons to Bosonic Modes in the Single-Layer High-Temperature $Bi_2Sr_2CuO_6$ Superconductor. *Phys. Rev. Lett.* **96**, 157003 (2006).

53. Lanzara, A. *et al.* Normal state spectral lineshapes of nodal quasiparticles in single layer Bi2201 superconductor. *J. Phys. Chem. Solids* **67**, 239–243 (2006).

54. Lee, W. S. *et al.* Superconductivity-induced self-energy evolution of the nodal electron of optimally doped $Bi_2Sr_2Ca_{0.92}Y_{0.08}Cu_2O_{8+\delta}$. *Phys. Rev. B* **77**, 140504 (2008).

55. Graf, J. *et al.* Bond Stretching Phonon Softening and Kinks in the Angle-Resolved Photoemission Spectra of Optimally Doped $Bi_2Sr_{1.6}La_{0.4}Cu_2O_{6+\delta}$ Superconductors. *Phys. Rev. Lett.* **100**, 227002 (2008).

56. Zhou, X. J., Cuk, T., Devereaux, T., Nagaosa, N. & Shen, Z.-X. *Handbook of High-Temperature Superconductivity: Theory and Experiment*, chap. Angle-Resolved Photoemission Spectroscopy on Electronic Structure and Electron-Phonon Coupling in Cuprate Superconductors, 87 (Springer, 2006).

57. Lee, W. S., Johnston, S., Devereaux, T. P. & Shen, Z.-X. Aspects of electron-phonon self-energy revealed from angle-resolved photoemission spectroscopy. *Phys. Rev. B* **75**, 195116 (2007).

58. Johnson, P. D. *et al.* Doping and Temperature Dependence of the Mass Enhancement Observed in the Cuprate $Bi_2Sr_2CaCu_2O_{8+\delta}$. *Phys. Rev. Lett.* **87**, 177007 (2001).

59. Gromko, A. D. *et al.* Mass-renormalized electronic excitations at $(\pi, 0)$ in the superconducting state of $Bi_2Sr_2CaCu_2O_{8+\delta}$. *Phys. Rev. B* **68**, 174520 (2003).

60. Kim, T. K., Kordyuk, A. A., Borisenko, S. V., Koitzsch, A., Knupfer, M., Berger, H. & Fink, J. Doping Dependence of the Mass Enhancement in $(Pb,Bi)_2Sr_2CaCu_2O_8$ at the Antinodal Point in the Superconducting and Normal States. *Phys. Rev. Lett.* **91**, 167002 (2003).

61. Sato, T. *et al.* Observation of Band Renormalization Effects in Hole-Doped High-T_c Superconductors. *Phys. Rev. Lett.* **91**, 157003 (2003).

62. Borisenko, S. V. *et al.* Parity of the Pairing Bosons in a High-Temperature Pb – $Bi_2Sr_2CaCu_2O_8$ Bilayer Superconductor by Angle-Resolved Photoemission Spectroscopy. *Phys. Rev. Lett.* **96**, 067001 (2006).

63. Borisenko, S. V. *et al.* Kinks, Nodal Bilayer Splitting, and Interband Scattering in $YBa_2Cu_3O_{6+x}$. *Phys. Rev. Lett.* **96**, 117004 (2006).

64. Plumb, N. C. *et al.* Large momentum-dependence of the main dispersion 'kink' in the high-T_c superconductor $Bi_2Sr_2Ca_{0.92}Y_{0.08}Cu_2O_{8+\delta}$. *New J. Phys.* **15**, 113004 (2013).

65. Kulić, M. L. & Dolgov, O. V. Dominance of the electron-phonon interaction with forward scattering peak in high-T_c superconductors: Theoretical explanation of the ARPES kink. *Phys. Rev. B* **71**, 092505 (2005).

66. He, J. *et al.* Coexistence of Two Sharp-Mode Couplings and their Unusual Momentum Dependence in the Superconducting State of $Bi_2Sr_2CaCu_2O_{8+\delta}$ Revealed by Laser-Based Angle-Resolved Photoemission. *Phys. Rev. Lett.* **111**, 107005 (2013).

67. He, J. Coexistence of Two Sharp-Mode Couplings in $Bi_2Sr_2CaCu_2O_{8+\delta}$. In *Angle-Resolved Photoemission Spectroscopy on High-Temperature Superconductors: Studies of Bi2212 and Single-Layer FeSe Film Grown on SrTiO₃ Substrate*, 59–70 (Springer Berlin Heidelberg, Berlin, Heidelberg, 2016).

68. Smallwood, C. L., Jozwiak, C., Zhang, W. & Lanzara, A. An ultrafast angle-resolved photoemission apparatus for measuring complex materials. *Rev. Sci. Instrum.* **83**, 123904 (2012).

69. Smallwood, C. L., Kaindl, R. A. & Lanzara, A. Ultrafast angle-resolved photoemission spectroscopy of quantum materials. *EPL* **115**, 27001 (2016).

70. Smallwood, C. L. *Time- and Angle-Resolved Photoemission Studies of Cuprate Superconductors*. Ph.D. thesis, University of California, Berkeley (2014).

71. Hüfner, S. *Photoelectron Spectroscopy: Principles and Applications* (Springer, 2003), 3rd edn.

72. Smallwood, C. L. *et al.* Tracking Cooper Pairs in a Cuprate Superconductor by Ultrafast Angle-Resolved Photoemission. *Science* **336**, 1137–1139 (2012).

73. Smallwood, C. L., Zhang, W., Miller, T. L., Jozwiak, C., Eisaki, H., Lee, D.-H. & Lanzara, A. Time- and momentum-resolved gap dynamics in $Bi_2Sr_2CaCu_2O_{8+\delta}$. *Phys. Rev. B* **89**, 115126 (2014).

74. Smallwood, C. L. *et al.* Influence of optically quenched superconductivity on quasiparticle relaxation rates in $Bi_2Sr_2CaCu_2O_{8+\delta}$. *Phys. Rev. B* **92**, 161102 (2015).

75. Ishida, Y., Saitoh, T., Mochiku, T., Nakane, T., Hirata, K. & Shin, S. Quasi-particles ultrafastly releasing kink bosons to form Fermi arcs in a cuprate superconductor. *Sci. Rep.* **6**, 18747 (2016).

76. Zhang, Z. *et al.* Photoinduced filling of near nodal gap and dissipation of quasiparticles in $Bi_2Sr_2CaCu_2O_{8+\delta}$ (2017).

77. Boschini, F. andda Silva Neto, E. H. *et al.* Collapse of high-T_c superconductivity via ultrafast quenching of the phase coherence (2017).

78. Zhang, W. *et al.* Signatures of superconductivity and pseudogap formation in nonequilibrium nodal quasiparticles revealed by ultrafast angle-resolved photoemission. *Phys. Rev. B* **88**, 245132 (2013).

79. Perfetti, L., Loukakos, P. A., Lisowski, M., Bovensiepen, U., Eisaki, H. & Wolf, M. Ultrafast electron relaxation in superconducting $Bi_2Sr_2CaCu_2O_{8+\delta}$ by time-resolved photoelectron spectroscopy. *Phys. Rev. Lett.* **99**, 197001 (2007).

80. Piovera, C. *et al.* Quasiparticle dynamics in high-temperature superconductors far from equilibrium: An indication of pairing amplitude without phase coherence. *Phys. Rev. B* **91**, 224509 (2015).

81. Smallwood, C. L., Miller, T. L., Zhang, W., Kaindl, R. A. & Lanzara, A. Nonequilibrium electron dynamics in a solid with a changing nodal excitation gap. *Phys. Rev. B* **93**, 235107 (2016).

82. Yang, S.-L. *et al.* Inequivalence of Single-Particle and Population Lifetimes in a Cuprate Superconductor. *Phys. Rev. Lett.* **114**, 247001 (2015).

83. Rameau, J. D. *et al.* Energy dissipation from a correlated system driven out of equilibrium. *Nat. Commun.* **7**, 13761 (2016).

84. Rameau, J. D. *et al.* Photoinduced changes in the cuprate electronic structure revealed by femtosecond time- and angle-resolved photoemission. *Phys. Rev. B* **89**, 115115 (2014).

85. Zhang, W. *et al.* Ultrafast quenching of electronboson interaction and superconducting gap in a cuprate superconductor. *Nat. Commun.* **5**, 4959 (2014).

86. Miller, T. L. *et al.* Resolving unoccupied electronic states with laser ARPES in bismuth-based cuprate superconductors. *Phys. Rev. B* **91**, 085109 (2015).

87. Miller, T. L., Zhang, W., Eisaki, H. & Lanzara, A. Particle-Hole Asymmetry in the Cuprate Pseudogap Measured with Time-Resolved Spectroscopy. *Phys. Rev. Lett.* **118**, 097001 (2017).

88. Rietveld, G., van Veenendaal, M., van der Marel, D. & Mooij, J. Temperature dependence of the chemical potential of high-T_c superconductors. *Physica B* **165**, 1605–1606 (1990).

89. Rietveld, G., Chen, N. Y. & van der Marel, D. Anomalous temperature dependence of the work function in YBa$_2$Cu$_3$O$_{7-\delta}$. *Phys. Rev. Lett.* **69**, 2578–2581 (1992).

90. Saito, S. *et al.* Temperature dependence of the work function of Bi$_2$Sr$_2$CaCu$_2$O$_8$ single crystal cleaved at low temperature. *Appl. Surf. Sci.* **252**, 379–384 (2005).

91. van der Marel, D. & Rietveld, G. Universal jump in slope of the chemical potential at second-order phase transitions. *Phys. Rev. Lett.* **69**, 2575–2577 (1992).

92. Avigo, I. *et al.* Coherent excitations and electron-phonon coupling in Ba/EuFe$_2$As$_2$ compounds investigated by femtosecond time- and angle-resolved photoemission spectroscopy. *J. Phys.: Condens. Matter* **25**, 094003 (2013).

93. Yang, L. X. *et al.* Ultrafast Modulation of the Chemical Potential in BaFe$_2$As$_2$ by Coherent Phonons. *Phys. Rev. Lett.* **112**, 207001 (2014).

94. Wang, Y. H. *et al.* Measurement of Intrinsic Dirac Fermion Cooling on the Surface of the Topological Insulator Bi$_2$Se$_3$ Using Time-Resolved and Angle-Resolved Photoemission Spectroscopy. *Phys. Rev. Lett.* **109**, 127401 (2012).

95. Sobota, J. A., Yang, S., Analytis, J. G., Chen, Y. L., Fisher, I. R., Kirchmann, P. S. & Shen, Z.-X. Ultrafast Optical Excitation of a Persistent Surface-State Population in the Topological Insulator Bi$_2$Se$_3$. *Phys. Rev. Lett.* **108**, 117403 (2012).

96. Crepaldi, A. *et al.* Ultrafast photodoping and effective Fermi-Dirac distribution of the Dirac particles in Bi$_2$Se$_3$. *Phys. Rev. B* **86**, 205133 (2012).

97. Crepaldi, A. *et al.* Evidence of reduced surface electron-phonon scattering in the conduction band of Bi$_2$Se$_3$ by nonequilibrium ARPES. *Phys. Rev. B* **88**, 121404 (2013).

98. Tanaka, S.-i. Utility and constraint on the use of pump-probe photoelectron spectroscopy for detecting time-resolved surface photovoltage. *J. Electron Spectrosc. Relat. Phenom.* **185**, 152–158 (2012).

99. Yang, S.-L., Sobota, J., Kirchmann, P. & Shen, Z.-X. Electron propagation from a photo-excited surface: implications for time-resolved photoemission. *Appl. Phys. A: Mater. Sci. Process.* **116**, 85–90 (2013).

100. Levy, G., Nettke, W., Ludbrook, B. M., Veenstra, C. N. & Damascelli, A. Deconstruction of resolution effects in angle-resolved photoemission. *Phys. Rev. B* **90**, 045150 (2014).

101. Graf, J., Jozwiak, C., Smallwood, C. L., Eisaki, H., Kaindl, R. A., Lee, D.-H. & Lanzara, A. Nodal quasiparticle meltdown in ultrahigh-resolution pump-probe angle-resolved photoemission. *Nat. Phys.* **7**, 805–809 (2011).

102. Zhou, X. *et al.* Space charge effect and mirror charge effect in photoemission spectroscopy. *J. Electron Spectrosc. Relat. Phenom.* **142**, 27–38 (2005).

103. Graf, J. *et al.* Vacuum space charge effect in laser-based solid-state photoemission spectroscopy. *Journal of Applied Physics* **107**, 014912 (2010).

104. Mouallem-Bahout, M., Gaud, J., Calvarin, G., Gavarri, J.-R. & Carel, C. Anisotropic thermal expansion and Grneisen coefficients of the bismuth cuprate 2-2-1-2. *Mater. Lett.* **18**, 181–185 (1994).

105. Asahi, T., Suzuki, H., Nakamura, M., Takano, H. & Kobayashi, J. Thermal expansion of superconducting $Bi_2Sr_2CaCu_2O_8$. *Phys. Rev. B* **55**, 9125–9129 (1997).

106. Marder, M. P. *Condensed Matter Physics*, chap. 6.5.1, 169–170 (John Wiley & Sons, 2010). [second edition].

107. Clarke, J. Experimental Observation of Pair-Quasiparticle Potential Difference in Nonequilibrium Superconductors. *Phys. Rev. Lett.* **28**, 1363–1366 (1972).

108. Tinkham, M. & Clarke, J. Theory of Pair-Quasiparticle Potential Difference in Nonequilibrium Superconductors. *Phys. Rev. Lett.* **28**, 1366–1369 (1972).

109. Ledbetter, H. Dependence of T_c on Debye temperature θ_D for various cuprates. *Physica C* **235**, 1325–1326 (1994).

110. Norman, M. R., Randeria, M., Ding, H. & Campuzano, J. C. Phenomenological models for the gap anisotropy of $Bi_2Sr_2CaCu_2O_8$ as measured by angle-resolved photoemission spectroscopy. *Phys. Rev. B* **52**, 615–622 (1995).

111. Van der Marel, D. Anomalous behaviour of the chemical potential in superconductors with a low density of charge carriers. *Physica C: Superconductivity* **165**, 35–43 (1990).

112. Wang, Y., Li, L. & Ong, N. P. Nernst effect in high-T_c superconductors. *Phys. Rev. B* **73**, 024510 (2006).

113. Kanigel, A. *et al.* Protected Nodes and the Collapse of Fermi Arcs in High-T_c Cuprate Superconductors. *Phys. Rev. Lett.* **99**, 157001 (2007).

114. Kanigel, A., Chatterjee, U., Randeria, M., Norman, M. R., Koren, G., Kadowaki, K. & Campuzano, J. C. Evidence for Pairing above the Transition Temperature of Cuprate Superconductors from the Electronic Dispersion in the Pseudogap Phase. *Phys. Rev. Lett.* **101**, 137002 (2008).

115. Lee, J., Fujita, K., Schmidt, A. R., Kim, C. K., Eisaki, H., Uchida, S. & Davis, J. C. Spectroscopic fingerprint of phase-incoherent superconductivity in the cuprate pseudogap state. *Science* **325**, 1099–1103 (2009).

116. Chatterjee, U. *et al.* Observation of a d-wave nodal liquid in highly underdoped $Bi_2Sr_2CaCu_2O_{8+\delta}$. *Nat. Phys.* **6**, 99–103 (2010).

117. Grilli, M., Seibold, G., Di Ciolo, A. & Lorenzana, J. Fermi surface dichotomy in systems with fluctuating order. *Phys. Rev. B* **79**, 125111 (2009).

118. Zhao, J. *et al.* Universal features in the photoemission spectroscopy of high-temperature superconductors. *Proc. Natl. Acad. Sci. USA* **110**, 17774–17777 (2013).

119. Comin, R. *et al.* Charge Order Driven by Fermi-Arc Instability in $Bi_2Sr_{2-x}La_xCuO_{6+\delta}$. *Science* **343**, 390–392 (2014).

120. Hamidian, M. H. *et al.* Atomic-scale electronic structure of the cuprate d-symmetry form factor density wave state. *Nat. Phys.* **12**, 150–156 (2015).

121. LeBlanc, J. P. F., Carbotte, J. P. & Nicol, E. J. Effects of a particle-hole asymmetric pseudogap on Bogoliubov quasiparticles. *Phys. Rev. B* **83**, 184506 (2011).

122. Zhang, W. *et al.* Stimulated emission of Cooper pairs in a high-temperature cuprate superconductor. *Scientific Reports* **6**, 29100 (2016).

123. Gedik, N., Blake, P., Spitzer, R. C., Orenstein, J., Liang, R., Bonn, D. A. & Hardy, W. N. Single-quasiparticle stability and quasiparticle-pair decay in $YBa_2Cu_3O_{6.5}$. *Phys. Rev. B* **70**, 014504 (2004).

124. Kaindl, R. A., Carnahan, M. A., Chemla, D. S., Oh, S. & Eckstein, J. N. Dynamics of Cooper pair formation in $Bi_2Sr_2CaCu_2O_{8+\delta}$. *Phys. Rev. B* **72**, 060510 (2005).

125. Coslovich, G. *et al.* Evidence for a photoinduced nonthermal superconducting-to-normal-state phase transition in overdoped $Bi_2Sr_2Ca_{0.92}Y_{0.08}Cu_2O_{8+\delta}$. *Phys. Rev. B* **83**, 064519 (2011).

126. Gedik, N., Langner, M., Orenstein, J., Ono, S., Abe, Y. & Ando, Y. Abrupt Transition in Quasiparticle Dynamics at Optimal Doping in a Cuprate Superconductor System. *Phys. Rev. Lett.* **95**, 117005 (2005).

127. Cortés, R., Rettig, L., Yoshida, Y., Eisaki, H., Wolf, M. & Bovensiepen, U. Momentum-Resolved Ultrafast Electron Dynamics in Superconducting $Bi_2Sr_2CaCu_2O_{8+\delta}$. *Phys. Rev. Lett.* **107**, 097002 (2011).

128. Rothwarf, A. & Taylor, B. N. Measurement of Recombination Lifetimes in Superconductors. *Phys. Rev. Lett.* **19**, 27–30 (1967).

129. Norman, M. R., Randeria, M., Ding, H. & Campuzano, J. C. Phenomenology of the low-energy spectral function in high-T_c superconductors. *Phys. Rev. B* **57**, R11093–6 (1998).

130. Demsar, J. *et al.* Pair-Breaking and Superconducting State Recovery Dynamics in MgB_2. *Phys. Rev. Lett.* **91**, 267002 (2003).

131. Kusar, P., Kabanov, V. V., Demsar, J., Mertelj, T., Sugai, S. & Mihailovic, D. Controlled Vaporization of the Superconducting Condensate in Cuprate Superconductors by Femtosecond Photoexcitation. *Phys. Rev. Lett.* **101**, 227001 (2008).

132. Beck, M., Klammer, M., Lang, S., Leiderer, P., Kabanov, V. V., Gol'tsman, G. N. & Demsar, J. Energy-Gap Dynamics of Superconducting NbN Thin Films Studied by Time-Resolved Terahertz Spectroscopy. *Phys. Rev. Lett.* **107**, 177007 (2011).

133. Miller, T. L., Zhang, W., Eisaki, H. & Lanzara, A. Interplay of superconductivity and bosonic coupling in the peak-dip-hump structure of $Bi_2Sr_2CaCu_2O_{8+\delta}$ (2017). In preparation.

134. Bardeen, J., Cooper, L. N. & Schrieffer, J. R. Theory of Superconductivity. *Phys. Rev.* **108**, 1175–1204 (1957).

135. Bok, J. M. *et al.* Quantitative determination of pairing interactions for high-temperature superconductivity in cuprates. *Sci. Adv.* **2** (2016).

136. Fischer, Ø., Kugler, M., Maggio-Aprile, I., Berthod, C. & Renner, C. Scanning tunneling spectroscopy of high-temperature superconductors. *Rev. Mod. Phys.* **79**, 353–419 (2007).

137. Loret, B. *et al.* Unconventional High-Energy-State Contribution to the Cooper Pairing in the Underdoped Copper-Oxide Superconductor $HgBa_2Ca_2Cu_3O_{8+\delta}$. *Phys. Rev. Lett.* **116**, 197001 (2016).

138. Zasadzinski, J. F., Coffey, L., Romano, P. & Yusof, Z. Tunneling spectroscopy of $Bi_2Sr_2CaCu_2O_{8+\delta}$: Eliashberg analysis of the spectral dip feature. *Phys. Rev. B* **68**, 180504 (2003).

139. Gabovich, A. M. & Voitenko, A. I. Charge density waves as the origin of dip-hump structures in the differential tunneling conductance of cuprates: The case of d-wave superconductivity. *Physica C* **503**, 7–13 (2014).

140. Parham, S. *et al.* Pair breaking caused by magnetic impurities in the high-temperature superconductor $Bi_{2.1}Sr_{1.9}Ca(Cu_{1-x}Fe_x)_2O_y$. *Phys. Rev. B* **87**, 104501 (2013).

141. Lucy, L. B. An iterative technique for the rectification of observed distributions. *Astronomical Journal* **79**, 745 (1974).

142. Feng, D. L. *et al.* Bilayer Splitting in the Electronic Structure of Heavily Overdoped $Bi_2Sr_2CaCu_2O_{8+\delta}$. *Phys. Rev. Lett.* **86**, 5550–5553 (2001).

143. Gromko, A. *et al.* ARPES studies of c-axis intracell coupling in $Bi_2Sr_2CaCu_2O_{8+\delta}$. *J. Phys. Chem. Solids* **63**, 2299–2304 (2002).

144. Kordyuk, A. A. *et al.* Origin of the Peak-Dip-Hump Line Shape in the Superconducting-State $(\pi, 0)$ Photoemission Spectra of $Bi_2Sr_2CaCu_2O_8$. *Phys. Rev. Lett.* **89**, 077003 (2002).

145. Borisenko, S. V. *et al.* Anomalous Enhancement of the Coupling to the Magnetic Resonance Mode in Underdoped Pb-Bi2212. *Phys. Rev. Lett.* **90**, 207001 (2003).

146. Renker, B., Gompf, F., Ewert, D., Adelmann, P., Schmidt, H., Gering, E. & Mutka, H. Changes in the phonon spectra of Bi 2212 superconductors connected with the metal-semiconductor transition in the series of $Bi_2Sr_2Ca_{1-x}Y_xCu_2O_8$ compounds. *Z. Phys. B* **77**, 65–68 (1989).